Advancing Stimulated Raman Scattering Microscopy through Deep Learning and Gel-Based Tissue Engineering

Thesis by
Li-En Lin

In Partial Fulfillment of the Requirements for
the degree of
Doctor of Philosophy

CALIFORNIA INSTITUTE OF TECHNOLOGY
Pasadena, California

2025
Defended May 15th, 2025

Li-En Lin
ORCID: 0000-0003-3086-6991

TO

My dear Family and Friends

ACKNOWLEDGEMENTS

Graduate school has been an incredible journey filled with unexpected twists, challenges, and discoveries. I'm deeply grateful to my advisor, Professor Lu Wei, for supporting my scientific curiosity and explorations every step of the way. Conversations with you always spark new ideas and novel things to explore. I would also like to thank my committee members, Professor Mitchio Okumura, Professor Linda Hsieh-Wilson, and Professor David Van Valen, for all the insightful feedback and guidance on my research projects and proposals. Your perspectives have been invaluable to my growth as a scientist.

A special thank you goes to my lab mentors, Kun Miao and Chenxi Qian, whose passion for research first inspired me to join the Wei Lab. Your enthusiasm made even the most challenging experiments feel exciting. I'm especially thankful to Adrian Colazo, with whom I collaborated closely. Thank you for always being there to troubleshoot laser issues and for your warmth and openness in our conversations, whether about science, food, culture, life, or everything in between. I truly enjoyed our conversations in and out of the lab. Thank you to all the members of the Wei group that I have had the privilege to work with—Haomin Wang, Jiajun Du, Ryan Leighton, Dongkwan Lee, Xiaotian Bi, Rahuljeet Chadha, Philip Kocheril, Noor Naji, Ziguang Yang, Joe Ambarian, and Berea Suen, for the camaraderie and support. To my undergraduate mentees, Emily Dunn, Jay Siri, and Bridget Yang, thank you for the opportunity to learn and grow through mentoring.

Beyond the lab, I've been incredibly fortunate to have friends having my back. Kai-Hung, thank you for your unwavering support since the very beginning of (and even before) this

PhD journey. Jerry, thank you for being my classmate of seven years and best buddy in LA. Yu-An and Beverley, thank you for all the memorable adventures we shared in both LA and the Bay Area. Franco, it was exciting and fun working on our (sometimes exhausting) project together. Chia Yu and Ting Ting, thank you for putting up with my rambling. Ashley, thanks for your emotional support, and for introducing me to Beeno, the sweetest cat ever.

I would like to thank my ACT and Taiwanese friends for all the warmth, laughter, and many delightful conversations and gatherings. I'm very grateful for the memories shared with Elle, Brooke, Allen, Howard, Albert, Yu-Ling, Steve, Daniel, Yen-Yung, Yu-Chen, Yun-Ting, Chao, Hao-Hsuan, Hsiao-Yi, Shih-Hao, Sabrina, Renee, Hsin, Ming-Hao, Sandy, Chien-Ying, Joyce, Jessie, Po-Hsuan, Cyuan-Han, Chun Ju, Chi-Fang, Ming-Li, Joshua, Chungyi, Chun, Han Hsin, Benjamin, Ting-Yu, and Sean. And to my Pokémon GO mates, especially Angel and Manny, thanks for all the fun walks and raids that gave me a break from the academic grind.

I want to thank the friends and colleagues I met throughout my time at Caltech for making this journey so much more enjoyable. Chia-Yu and Fan, thank you for being such easygoing roommates. I'm also grateful to those I worked with in class, including Zachary, Tynesha, Jimmy, Sulan, Honson, and Perez, for all the teamwork. During the early days when I was still finding my way at Caltech, I truly appreciated the support, guidance, and friendship of Tianyi, Yu Shiuan, and Gracie. I would also like to thank the inspiring mentors and friends I met through the Caltech Seed Fund: Jay, Julie, Sona, Jacob, Alexander, Rifat, Vivienne, Jose, Eric, Amanda, Jolena, and Stephanie. Your guidance and encouragement have made a lasting impact on me. Lastly, to the friends who gave me that final push when I needed it most,

Annie, Kay, Chun-Ying, Rachel, Carol, Josephine, and many others, I couldn't have made it to the finish line without you.

Most of all, I need to express my greatest appreciation to my family members. My parents provided me with the best environment I could imagine to grow up in, along with the freedom to explore my interests, which nurtured my passion for science. My sister, who is the uplifter of our family, is the reason I had the courage to pursue a PhD abroad. Without their unconditional love and support throughout the years, I wouldn't be who I am today.

ABSTRACT

Stimulated Raman scattering (SRS) microscopy is a highly effective label-free imaging method for investigating the molecular composition of biological systems. Its broader use has been held back by spatial resolution, imaging speed, and large-scale tissue imaging compatibility. Breaking these limitations requires an integrated approach beyond the development of optical hardware. This thesis introduces a compilation of techniques that leverage gel-based tissue engineering and deep learning to enhance the capabilities of SRS microscopy.

The first chapter, Gel-Enabled Super-Resolution Label-Free Volumetric Vibrational Imaging, introduces VISTA, a sample-expansion vibrational imaging technique that achieves label-free super-resolution imaging of protein-dense biological structures with resolution as fine as 78 nm. By enabling isotropic expansion and protein retention, VISTA allows for high-throughput, unbiased volumetric imaging without labeling, with further enhancement using deep learning-based component prediction.

The second chapter, High-Resolution Imaging of In Vivo Protein Aggregates, applies VISTA to image amyloid-beta and polyQ aggregates in biological samples with high specificity. Combined with segmentation using convolutional neural networks, this technique is capable of mapping aggregate structure and microenvironments, enabling new insights into neurodegenerative disease pathology.

The third chapter, High-Throughput Volumetric Mapping Facilitated by Active Tissue SHRINK, introduces SHRINK, a hydrogel-based sample shrinkage method that

isotropically shrinks tissue while maintaining structural integrity. Active shrinkage enhances imaging throughput and signal sensitivity and enables rapid, large-scale, three-dimensional whole-organ mapping with SRS microscopy.

The fourth chapter, Deep Learning-Augmented Metabolic Profiling in Live Neuronal Cultures, presents a tandem deep learning platform for live-cell metabolic imaging. By integrating a recurrent convolutional neural network and U-Net segmentation model with deuterium-labeled metabolic tracing, this platform enables non-invasive, high-speed profiling of lipid, protein, glucose, and water metabolism in neuronal subtypes under physiological and pathological conditions.

These developments represent multidimensional strategies that expand the application of SRS microscopy to high-resolution, high-throughput, and dynamic imaging in a variety of biological systems. The integration of deep learning and gel-based tissue engineering techniques opens new avenues for SRS microscopy to explore complex biological questions.

PUBLISHED CONTENT AND CONTRIBUTIONS

Qian, C. [#], Miao, K. [#], Lin, L. E., Chen, X., Du, J., & Wei, L. (2021). Super-resolution label-free volumetric vibrational imaging. *Nature Communications*, *12*(1), 3648. doi: 10.1038/s41467- 021-23951-x.

[#]equal contribution. L.-E.L. performed U-Net training for multiplexed VISTA, performed the experiments, and participated in the writing the manuscript.

Lin, L. E., Miao, K., Qian, C., & Wei, L. (2021). High spatial-resolution imaging of label-free in vivo protein aggregates by VISTA. *Analyst*, *146*(13), 4135-4145. doi: 10.1039/D1AN00060H

L.-E.L. participated in the conceptualization of the project, designed and performed the experiments, analyzed data, and participated in writing the manuscript.

Miao, K., Lin, L. E., Qian, C., & Wei, L. (2022). Label-free super-resolution imaging enabled by vibrational imaging of swelled tissue and analysis. *Journal of Visualized Experiments (JoVE)*, (183), e63824. doi: 10.3791/63824

L.-E.L. performed U-Net training for multiplexed VISTA, performed the experiments, and participated in the writing of the manuscript.

Lin, L. E., Colazo, A., Bi, X., Du, J., & Wei, L. (2025). High-Throughput Volumetric Mapping Facilitated by Active Tissue SHRINK. *Small Methods*, 2500382. doi: 10.1002/smtd.202500382

L.-E.L. participated in the conceptualization of the project, designed and performed the experiments, analyzed data, and participated in writing the manuscript.

Bi, X., Lin, L. E., & Wei, L. (2025). BPS2025-Quantitative bond-selective imaging of polyQ aggregates without EGFP labeling reveals aggregation compartmentalization and growth dynamics in live neurons. *Biophysical Journal*, *124*(3), 512a. doi: 10.1016/j.bpj.2024.11.220

L.-E.L. designed and performed the experiments and participated in writing the manuscript.

Wang, H., Kocheril, P. A., Yang, Z., Lee, D., Naji, N., Du, J., Lin, L. E., & Wei, L. (2024). Room-Temperature Single-Molecule Infrared Imaging and Spectroscopy through Bond-Selective Fluorescence. *Angewandte Chemie International Edition*, *63*(52), e202413647. doi: 10.1002/anie.202413647

L.-E.L. helped with theoretical calculations and participated in writing the manuscript.

TABLE OF CONTENTS

Chapter 1

INTRODUCTION

1.1 Stimulated Raman Scattering Microscopy

Recent developments in optical imaging have tremendously increased the possibility of investigating biological systems, allowing us to observe complicated structures and dynamic processes at subcellular resolution. In comparison to other label-free imaging techniques, stimulated Raman scattering (SRS) microscopy is unique in its ability to interrogate the native vibrational fingerprints of biomolecules[1]. In contrast to fluorescence microscopy, which requires chemical labeling, SRS provides chemically specific contrast based on molecular vibrations, such as CH_3 and CH_2 stretching modes. Notably, SRS imaging has proven to be useful for imaging native protein and lipid distributions in live biological tissues, and it is a useful tool for *in situ* tissue physiology and pathology research[2]. In addition, SRS facilitates the quantitative and noninvasive analysis of metabolic activity by using bioorthogonal vibrational tags, for example, deuterium-labeled metabolites, thus revealing new possibilities for the exploration of cell-specific dynamics in varied environments, including the brain[3–6].

1.2 Limitations of Current SRS Microscopy Techniques

Despite its growing adoption and the advantages of label-free imaging, conventional SRS microscopy is limited by several major limitations. First, its spatial resolution is not capable of imaging nanoscale structures such as amyloid fibrils and protein aggregates, which are typically less than 100 nm in diameter[7,8]. Super-resolution SRS methods, including approaches based on saturation excitation or structured illumination, have achieved only modest gains and are constrained by requiring specialized equipment[9–12]. Second, although SRS offers volumetric imaging capability, imaging throughput is compromised by light scattering and signal sensitivity, particularly in large or intact tissues[13]. Furthermore, longitudinal metabolic imaging in live systems is also compromised by the possibility of photodamage and the inability to resolve intricate, multicellular identities in densely packed tissues or cultures. These constraints pose challenges to high-throughput, cell-type-specific investigation of intricate structural and metabolic properties in physiological and pathological conditions.

1.3 Gel-Based Tissue Engineering for Enhanced Biological Insight

To address the limitations in spatial resolution and scalability of optical imaging techniques, sample-engineering approaches have appeared as valuable additions to optical techniques. Expansion microscopy (ExM) and analogous techniques accomplish super-resolution by physical magnification of biological samples via embedding in swellable hydrogels, allowing super-resolution imaging with conventional microscopy setups[14]. From this idea, our approach, vibrational imaging of expanded tissues and analysis (VISTA), takes ExM to SRS

microscopy, where label-free nanoscale visualization of protein-enriched features is possible due to isotropic tissue expansion[7]. VISTA maintains dense protein aggregates like amyloid-β plaques and allows for a detailed three-dimensional mapping of surrounding microenvironments such as nuclei and vasculature[8]. Alternatively, the SHRINK platform utilizes a hydrogel-assisted tissue-shrinking methodology that concentrates molecular densities and substantially enhances imaging speed[15]. By maintaining isotropic volume shrinkage while supporting structural integrity, SHRINK leads to improvements in SRS signal sensitivity and subcellular-resolution imaging in millimeter-thick tissues. These gel-based engineering strategies offer scalable, high-resolution solutions for visualizing complex biological tissues, especially in limited or rare human samples.

1.4 Improving SRS Microscopy with Deep Learning

Deep learning offers transformative potential for addressing the throughput and segmentation challenges inherent to SRS imaging[7]. The tandem deep learning framework of a recurrent convolutional neural network (RCNN) and a U-Net model enables high-speed volumetric imaging and cell-type classification in live neuronal co-cultures. The RCNN leverages spatial continuity of biological features to infer sparsely acquired axial data, reducing acquisition time and photodamage in longitudinal experiments[16]. Sequentially, the U-Net architecture allows for the segmentation of morphologically heterogeneous cell types from unlabeled datasets[17]. Integration of the deep learning architecture with bioorthogonal chemical imaging enables real-time, noninvasive metabolic

profiling of neurons, astrocytes, and oligodendrocytes in common tissue environments. This strategy breaks the long-standing trade-offs between speed, resolution, and cell-type specificity and thus quantitative characterization of cellular activities in regular and disease states.

1.5 Summary and Outlook

Integration with deep learning and gel-based tissue engineering has empowered SRS microscopy with enhanced resolution, scalability, and specificity. Collectively, these technologies enable the visualization of intricate tissue architecture, nanoscale structures, and dynamic metabolic processes in intact and living biological samples. This thesis describes a suite of methodological and conceptual improvements that utilize this platform to examine protein aggregation and metabolic dynamics in neuronal and tissue systems. By overcoming the optical, structural, and computational constraints of current methods, this thesis presents the groundwork for a new generation of super-resolved, label-free, high-throughput imaging modalities, with applications extending to neurodegeneration research, tissue mapping, and biomedical imaging applications.

1.6 References

1. Wei, L. *et al.* Live-Cell Bioorthogonal Chemical Imaging: Stimulated Raman Scattering Microscopy of Vibrational Probes. *Acc. Chem. Res.* **49**, 1494–1502 (2016).

2. Wang, P. *et al.* Imaging lipid metabolism in live Caenorhabditis elegans using fingerprint vibrations. *Angew. Chem. Int. Ed Engl.* **53**, 11787–11792 (2014).
3. Wei, L. *et al.* Imaging Complex Protein Metabolism in Live Organisms by Stimulated Raman Scattering Microscopy with Isotope Labeling. *ACS Chem. Biol.* **10**, 901–908 (2015).
4. Wei, L., Yu, Y., Shen, Y., Wang, M. C. & Min, W. Vibrational imaging of newly synthesized proteins in live cells by stimulated Raman scattering microscopy. *Proc. Natl. Acad. Sci.* **110**, 11226–11231 (2013).
5. Du, J. *et al.* Raman-guided subcellular pharmaco-metabolomics for metastatic melanoma cells. *Nat. Commun.* **11**, 4830 (2020).
6. Zhang, L. *et al.* Spectral tracing of deuterium for imaging glucose metabolism. *Nat. Biomed. Eng.* **3**, 402–413 (2019).
7. Qian, C. *et al.* Super-resolution label-free volumetric vibrational imaging. *Nat. Commun.* **12**, 3648 (2021).
8. Lin, L.-E., Miao, K., Qian, C. & Wei, L. High spatial-resolution imaging of label-free in vivo protein aggregates by VISTA. *Analyst* **146**, 4135–4145 (2021).
9. Gasecka, A., Daradich, A., Dehez, H., Piché, M. & Côté, D. Resolution and contrast enhancement in coherent anti-Stokes Raman-scattering microscopy. *Opt. Lett.* **38**, 4510–4513 (2013).
10. Gong, L., Zheng, W., Ma, Y. & Huang, Z. Higher-order coherent anti-Stokes Raman scattering microscopy realizes label-free super-resolution vibrational imaging. *Nat. Photonics* **14**, 115–122 (2020).

11. Gong, L., Zheng, W., Ma, Y. & Huang, Z. Saturated Stimulated-Raman-Scattering Microscopy for Far-Field Superresolution Vibrational Imaging. *Phys. Rev. Appl.* **11**, 034041 (2019).
12. Watanabe, K. *et al.* Structured line illumination Raman microscopy. *Nat. Commun.* **6**, 10095 (2015).
13. Lin, H. *et al.* Microsecond fingerprint stimulated Raman spectroscopic imaging by ultrafast tuning and spatial-spectral learning. *Nat. Commun.* **12**, 3052 (2021).
14. Chen, F., Tillberg, P. W. & Boyden, E. S. Expansion microscopy. *Science* **347**, 543–548 (2015).
15. Lin, L.-E., Colazo, A., Bi, X., Du, J. & Wei, L. High-Throughput Volumetric Mapping Facilitated by Active Tissue SHRINK. *Small Methods* e2500382 (2025) doi:10.1002/smtd.202500382.
16. Huang, L., Chen, H., Luo, Y., Rivenson, Y. & Ozcan, A. Recurrent neural network-based volumetric fluorescence microscopy. *Light Sci. Appl.* **10**, 62 (2021).
17. Ronneberger, O., Fischer, P. & Brox, T. U-Net: Convolutional Networks for Biomedical Image Segmentation. Preprint at https://doi.org/10.48550/arXiv.1505.04597 (2015).

Chapter 2

GEL-ENABLED SUPER-RESOLUTION LABEL-FREE VOLUMETRIC VIBRATIONAL IMAGING

Qian, C.#; Miao, K.# ; Lin, L.-E.; Chen, X.; Du, J.; Wei, L. Super-Resolution Label-Free Volumetric Vibrational Imaging. Nat Commun. 2021, 12 (1), 3648. doi:10.1038/s41467-021-23951-x.

Miao, K., Lin, L. E., Qian, C., & Wei, L. (2022). Label-free super-resolution imaging enabled by vibrational imaging of swelled tissue and analysis. Journal of Visualized Experiments (JoVE), (183), e63824. doi: 10.3791/63824

2. 1 Summary

Innovations in high-resolution optical imaging have allowed visualization of nanoscale biological structures and connections. However, super-resolution fluorescence techniques, including both optics-oriented and sample-expansion based, are limited in quantification and throughput especially in tissues from photobleaching or quenching of the fluorophores, and low-efficiency or non-uniform delivery of the probes. Here, we report a general sample-expansion vibrational imaging strategy, termed VISTA, for scalable label-free high-resolution interrogations of protein-rich biological structures with resolution down to 78 nm. VISTA achieves decent three-dimensional image quality through optimal retention of endogenous proteins, isotropic sample expansion, and deprivation of scattering lipids. Free from probe-labeling associated issues, VISTA offers unbiased and

high-throughput tissue investigations. With correlative VISTA and immunofluorescence, we further validated the imaging specificity of VISTA and trained an image-segmentation model for label-free multi-component and volumetric prediction of nucleus, blood vessels, neuronal cells, and dendrites in complex mouse brain tissues. VISTA could hence open new avenues for versatile biomedical studies.

2. 2 Introduction

Our knowledge of biology is significantly advanced by the development of optical imaging techniques. They reveal multi-dimensional spatial information that is crucial for understanding numerous functions and mechanisms in complex environments. At subcellular levels, super-resolution fluorescence microscopy techniques, including instrument-based stimulated emission depletion (STED) microscopy, photo-activated localization microscopy (PALM), and stochastic optical reconstruction microscopy (STORM)[1,2], have been devised to overcome the diffraction limit barrier and allow optical visualization of previously unresolvable structures with nanometer resolution. Moreover, sample-oriented strategies, by physically expanding specimens embedded in swellable polymer hydrogels, have made a significant impact on high-resolution imaging of versatile samples[3]. For example, expansion microscopy (ExM) typically achieves a four-fold resolution enhancement using conventional fluorescence microscopes with isotropic sample expansion[4,5].

Despite their wide applications for uncovering unknown biological events through fine structural and functional characterizations, the super-resolution fluorescence microscopy has a few fundamental limits that originate from the requirement of fluorophore labeling. First, photobleaching and decay of the fluorophores make these techniques less ideal for repetitive and quantitative examinations of target structures[1-5]. This is especially problematic when the sample specimen is limited (e.g., clinical samples). Second, immunofluorescence, the widely used strategy for visualizing various proteins without genetic manipulation, poses serious issues of prolonged sample preparations and inhomogeneous antibody labeling in intact tissues[6]. This is due to the slow diffusion of large antibodies into the tissues and the depletion of probes on the surface[7]. To circumvent these fluorophore-associated challenges, we seek to have a super-resolution imaging modality that does not require labels.

Complementary to fluorescence, Raman microscopy targets the specific vibrational motions and maps out the distribution of chemical-bond specific structures and molecules inside live biological systems in a label-free or minimum labeling fashion. In particular, nonlinear stimulated Raman scattering (SRS) has been proven to be a highly successful optical imaging strategy for label-free or tiny-label imaging of biological samples with resolution and speed similar to those of fluorescence[8,9]. For example, SRS imaging targeting the methyl group (i.e. CH_3) vibrations from endogenous proteins at 2940 cm^{-1} (**Fig. 1a and S1**) has been demonstrated for visualizing proteins-rich structures with submicron

resolution at a speed up to video rate in live animals[10]. In principle, implementation of super-resolution Raman imaging could bypass the need of and hence the issues from fluorophore labeling. Despite extensive efforts, this goal has remained challenging. Strategies including excitation saturation, signal suppression with a donut beam or structural illumination have been reported [11-15]. However, they rely on additional specialized optics and the resolution enhancement is only 1.7 times on biological samples[13-15]. While such optics-based strategies have been heavily explored, there are no known efforts from the perspective of engineering samples for label-free super-resolved Raman imaging.

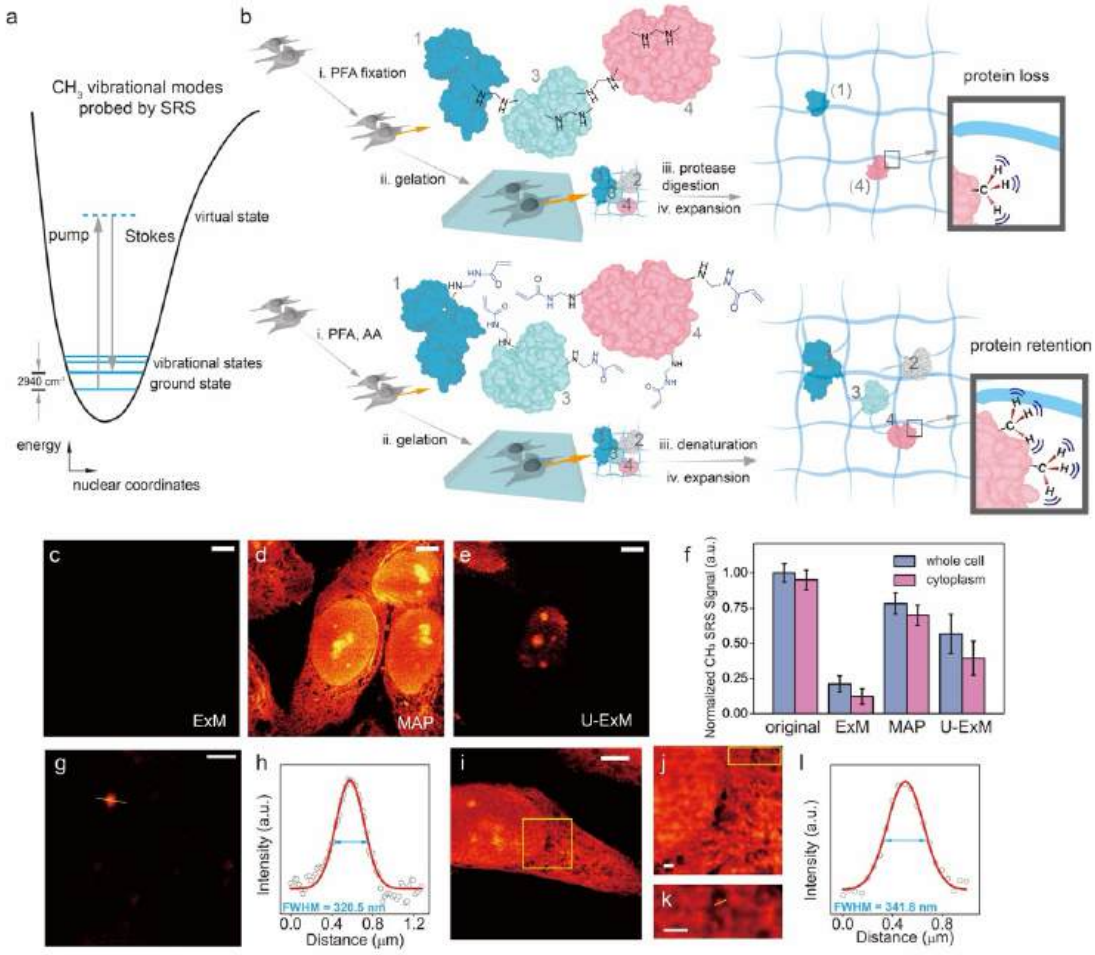

Figure 1. High-resolution label-free vibrational imaging of expanded and protein-retained samples. a, Energy scheme for SRS probing of CH_3 vibrational motion at 2940 cm^{-1}. More details in Fig. S1. **b**, Comparison of protein retention (i.e. the methyl groups, CH_3, from proteins) for SRS imaging between ExM (top) and MAP (bottom) based sample-hydrogel embedding procedures following different fixation, hybridization and homogenization chemistries. **c-e**. SRS imaging of CH_3 at 2940 cm^{-1} for expanded HeLa cells following ExM, MAP, and U-ExM sample treatment under the same intensity scale. Scale bars: 20 μm. **f**,

Quantification of proteins retention levels by comparing average CH_3 signals in expanded cells after ExM, MAP and U-ExM procedures with that from unprocessed HeLa cells (original). CH_3 signals in expanded cells were scaled back with the average expansion ratios for comparison. Data shown as mean ± SD. **g-h**, Quantification of SRS resolution by imaging the C-H vibration at 3050 cm^{-1} from a representative 100 nm polystyrene bead (g) and fitting its cross-section profile (h). Scale bar: 1 μm. **i-l**, Fitted VISTA imaging cross-section profile (l) from a small structural feature (k) of expanded HeLa cells (i-k, j, k are zoom-in views from the boxed regions in i, j respectively). Scale bars: 30 μm in (i), 2 μm in j-k. For processed samples, the length scale is in terms of distance after expansion.

2. 3 Results

Here, we report a super-resolution label-free vibrational imaging strategy in cells and tissues that couples the sensitive SRS microscopy with recent sample-treatment innovations. We term this strategy *V*ibrational *I*maging of *S*welled *T*issues and *A*nalysis (VISTA). We embed biological samples in polymer hydrogels, expand the sample-hydrogel hybrid in water, and target the vibrational motion of retained CH_3 groups from endogenous proteins by SRS for visualization. Our devised strategy possesses a few desirable features. First, compared to fluorescence imaging, VISTA avoids any label-associated issues, allowing uniform imaging and a much higher throughput especially in tissues.

Second, compared to optics-based Raman imaging, VISTA is easy to implement without any additional instrument and achieves an unprecedented Raman resolution down to 82 nm on biological samples. Importantly, it allows high-resolution imaging deep into the tissues[16], a common limit shared by all instrument-based super-resolution microscopy. Third, with further implementation of a convolutional neural network (CNN) for image segmentation[17], VISTA could offer specific, multi-component, and volumetric imaging in complex tissues with quality similar to that of fluorescence.

As a first step to establish VISTA, we asked whether the sample expansion strategy is compatible with SRS microscopy. We embedded HeLa cells in a polymer gel following the widely-used ExM protocol[4,5] (**Fig. 1b, top**), which involves paraformaldehyde (PFA) fixation, gelation, and sample homogenization through protease digestion. We then performed SRS imaging to visualize hydrogel-retained endogenous proteins in expanded cells at 2940 cm^{-1} (i.e. the CH_3 channel). However, almost no CH_3 contrast could be detected (**Fig. 1c, ExM and Fig. S2a**), indicating an extensive loss of proteins or protein fragments under strong protease digestion (i.e., proteinase K)—a known issue in ExM[5]. Indeed, our quantification in CH_3 channel showed that the protein loss could reach 79% (**Fig. 1f**), consistent with a recent fluorescence analysis[18]. With such a high protein content loss and an approximate 64-fold signal dilution due to 4-fold isotropic sample expansion, SRS signals are therefore diminished. We asked whether reducing digestion time or altering to a milder protease (e.g. Lys-c)[5] would help retain SRS signals. Unfortunately, proteinase K already significantly

digests the protein network even within 30 min (**Fig. S2**). Further reducing the digestion time or changing the protease comes at the expense of low expansion ratios and sample distortion after expansion due to incomplete homogenization of PFA-crosslinked protein networks.

The key to VISTA is to preserve the maximum level of proteins for SRS imaging while achieving optimal homogenization for isotropic sample expansion. Since protease digestion is only required when extensive intra- and inter- protein crosslinking arises from PFA fixation[19], we resorted to using magnified analysis of proteome (MAP)[20], an alternative sample-hydrogel hybridization protocol. MAP significantly reduces such PFA-induced protein crosslinking by introducing high concentration of acrylamide (AA) together with PFA fixation so that the excess AA will react with and hence quench the reactive methylols formed by protein-PFA reaction[20] (**Fig. 1b, bottom**). The subsequent sample homogenization is achieved by protein denaturation instead of protease digestion. With optimizations of incubation time, SRS imaging of CH_3 showed clear cellular structures with a decent signal-to-noise ratio in expanded cells (**Fig. 1d, MAP**). Characterizations of cell sizes before and after expansion yielded an average expansion ratio of four-fold, close to that reported through fluorescence[20]. Further quantification of the average CH_3 signal from MAP-processed cells compared to that from unprocessed cells indeed confirmed that proteins were largely preserved (**Fig. 1f**). Here, the slightly lowered CH_3 intensity from MAP was likely due to the removal of lipids (**Fig. S3**). Recently, an ultrastructure expansion microscopy (U-ExM) was reported to image ultrastructures with decreased concentration of

AA[21]. However, our analysis demonstrated that lowering AA concentration would still lead to a loss of a rather significant portion of proteins (**Fig. 1e**, U-ExM and **Fig. 1f**, with an additional loss of 21% in whole cells and 32% in cytoplasm compared to MAP). We therefore concluded that MAP-based sample embedding protocol allows high-quality VISTA imaging of protein-rich subcellular structures that were not clearly identifiable with the normal SRS imaging resolution (**Fig. 1d, MAP vs Fig. S1b,** e.g. the sub-structure of nucleoli and the network in cytosol).

Since the signal of VISTA comes from the CH_3 channel where the spectral crosstalk of other vibrations might exist, we next examined possible background contributions from both CH_2 vibrations of the hydrogel and the O-H stretch of the water. We compared the background sizes and spatial distributions by replacing normal hydrogel monomer and water with their deuterated correspondents respectively. Our data showed that the background introduced from each component can be largely minimized through the deuteration strategy (**Fig. S4**) and the lowering of the signals was uniform throughout the cellular samples, implying that the background is constant and does not introduce any heterogeneous imaging features. After optimizing and confirming the sample processing and imaging conditions, we then aimed to determine the achievable resolution of VISTA. We performed regular SRS imaging on 100 nm polystyrene beads at 3050 cm^{-1} for C-H bonds with a NA=1.05 objective (**Fig. 1g**). We obtained a fitted image cross-section with a full width at half maximum (FWHM) of 320 nm, which designates a resolution of 382 nm of the SRS microscope by

Rayleigh criterion after deconvolution of the bead object function (**Fig. 1h)**. These data indicate that VISTA offers a 96 nm effective resolution after a 4-fold isotropic sample expansion. We also confirmed a similar level of resolution of VISTA on small structural features within HeLa cells (**Fig. 1i-l**). The effective resolution could be further pushed to an unprecedented 82 nm with a higher-NA objective (i.e. NA=1.2) **(Fig. S5).**

With isotropic sample expansion, VISTA also provides sharp three-dimensional (3D) views of cellular morphology and subcellular structures (**Fig. S6a-b**). In addition to imaging normal cell states, we applied VISTA to visualizing structural changes of HeLa cells throughout mitosis in metaphase, anaphase, telophase, and interphase (**Fig. 2a-d**). VISTA images clearly resolved fine structures including cytosolic inner networks, small membrane protrusions of microvilli (**Fig. 2a-d, white arrowed**), and protein-rich contractile ring and midbody (**Fig. 2d, blue arrowed**). In addition, we observed an interesting change of protein contents during mitosis. The relative level of chromosome-associated proteins decreases as the nuclear envelopes disintegrate. This is evidenced by the dark region in cells (**Fig. 2a-c)**, which designates chromosome structures, confirmed by DAPI fluorescence stain (**Fig. S7**). The protein level then increases as the nuclear envelopes reform at the end of the mitosis in telophase (**Fig. 2d, green arrowed**). The 3D views of the cells are shown in **Fig. S6c-d**. These data imply that VISTA is capable of performing quantitative total protein analysis at subcellular compartments.

Apart from visualizing fine subcellular structures, VISTA is well-suited for tissue imaging. We first demonstrated VISTA on the optical transparent zebrafish embryos, in particular the cone and rod photoreceptors in the outer segment (OS), which are important model systems for understanding visual perception[22,23]. Comparisons of CH_3 images before (**Fig. 2e**) and after (**Fig. 2f**) sample embedding and expansion from the same area presented a clear change of contrast due to lipid removal, which allowed us to unambiguously image protein-rich structures, e.g., the retinal pigment epithelium (**Fig. 2g,** arrow indicated). Our data also confirmed a similar level of sample expansion ratio on tissues compared to that of cells (**Fig. S8**). We then aimed to implement VISTA on the much more scattering and complex mouse brain tissues, especially for the hippocampus where characterizations of intricate structural relationship are important for functional understanding of a series of physiological (e.g. memory formation) and pathological (e.g. neurodegenerative diseases) events[24,25]. Our mosaic VISTA image on hippocampus (**Fig. 2h**) reveals clear and specific contrast from neuronal cell bodies, processes, and also likely blood vessel cross-sections at various locations (**Fig. 2i-l, green, blue and white arrows indicated, respectively, in Fig. 2j**). All these features are virtually indistinguishable in regular SRS images due to a much lower resolution and the interference of lipid signals (**Fig. S9**). With the homogenization of sample refractive index after lipid removal, deep VISTA imaging throughout a 1 mm hippocampal tissue (effectively 250 μm in unexpanded tissues) is also achieved (**Fig. 2m**). We note that our current imaging depth is mainly limited by the short working distance of the signal-collecting

condenser and could be significantly improved by replacing both the objective and the condenser with long working distance objectives (e.g., 8 mm), specifically designed for tissue-clearing imaging of whole mouse brain hemispheres[26,27].

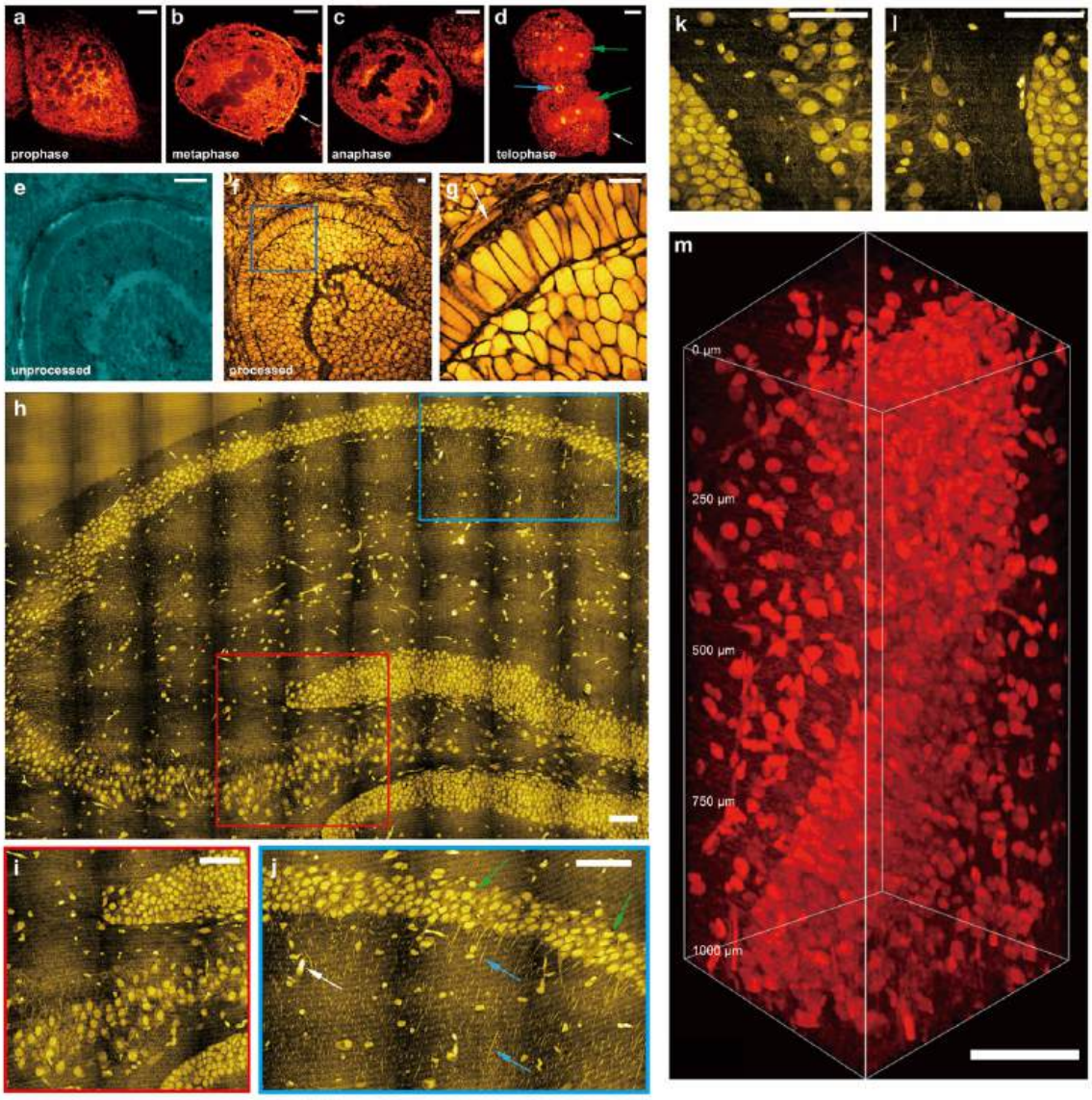

Figure 2. Super-resolution three-dimensional VISTA imaging of cells and tissues. a-d, Mitotic HeLa cells in prophase (a), metaphase (b), anaphase (c), and telophase (d). **e-g**, zebrafish embryonic retina before processing and after

expansion: unprocessed (e), expanded (f), and zoom-in view from the boxed region in f (g). **h**, A mosaic VISTA image of a hippocampal tissue. **i-l**, zoomed-in high-resolution view from color-boxed areas (i, red box; j, blue box) and selected regions in h. Representative neuronal cell bodies, neuronal processes, and likely blood vessel cross-sections are indicated by green, blue, and white arrows respectively in j. **m**, 3D volume VISTA imaging of a hippocampal tissue throughout 1000 μm depth. Scale bars: 20 μm (a-g) and 200 μm (h-m). For processed samples, the length scale is in terms of distance after expansion.

Since VISTA distinctly delineates the shapes of neuronal cells, processes, and likely blood vessels (**Fig. 2h-l**), we set out to validate the identities of these protein-rich biological components in VISTA images with established immunofluorescence. We were able to nicely correlate almost all structures shown in VISTA with fluorescence targets across various regions in brain tissues, including hippocampus and cortex. First, each vessel-like structure in VISTA is confirmed by lectin-DyLight594 staining, including those in vessel heavy regions within the hippocampus **(Fig. 3a-b, S10a-c)** and larger ones likely of arteries[20,28] **(Fig. 3c-d)**. In addition to capturing vessel structures and distributions, VISTA could also image protein abundant red blood cells inside vessels that are retained in the polymer gel network (**Fig. 3c, Fig S10d-f**). Second, all the nuclei shown in VISTA have one-to-one correspondence to DAPI labeling **(Fig. 3e&g)**. We found that a small portion of these nuclei are from vascular endothelial cells, confirmed

by their co-localizations with lectin vessel staining (**Fig. 3e-h,** arrowed) and GLUT1 immunostaining (**Fig. S11**, arrowed). The rest of the nuclei should come from various types of cells including neurons, astrocytes, oligodendrocytes, etc. Third, together with nuclear structures, some cells also present clear contrast of cytoplasm. Our further correlative imaging identified that all these cell bodies captured by VISTA belong to matured neuronal cells, but not to astrocytes or oligodendrocytes. This is confirmed by the co-localizations of VISTA cell bodies with immuno-fluorescence-stained NeuN (matured neuron marker**, Fig. 3i-j**) and MAP2 (marker of neuronal perikarya and dendrites**, Fig. 3k-l**), and the lack of cross-localizations to glial fibrillary acidic protein (GFAP, astrocyte cellular maker, **Fig. S12a-f**) and myelin basic proteins (MBP, oligodendrocyte cellular marker, **Fig. S12g-l**). These results also suggest that maturated neuronal cells are more protein abundant in the cytosols compared to astrocytes and oligodendrocytes, a result difficult to quantify by other methodologies. Fourth, in addition to cell bodies, neuronal processes visualized in VISTA could be assigned to dendrites, which showed decent overlap with those imaged by MAP2 stains (**Fig. 3k-l**). Our characterizations by correlative immunofluorescence imaging hence confirm that VISTA offers holistic mapping of nuclei, vessels, and neuronal cell distributions and dendritic connections in brain tissues, without any labels.

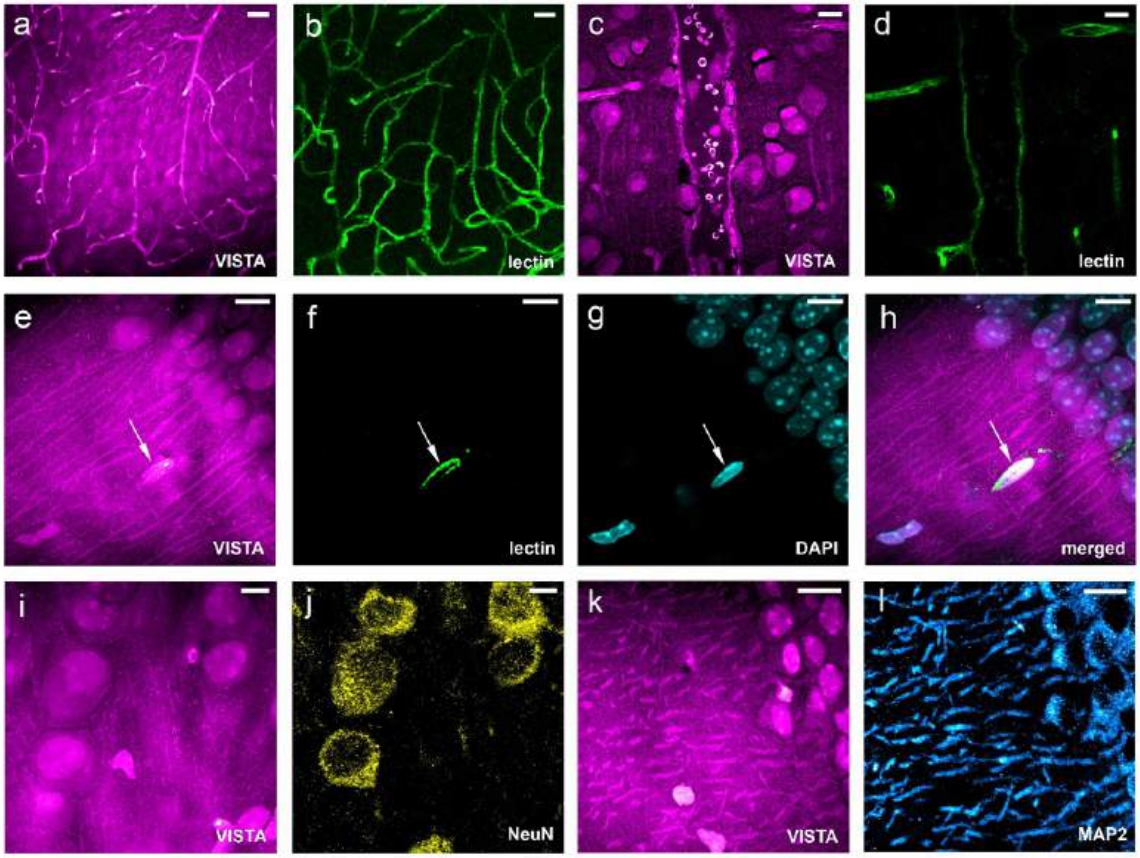

Figure 3. Validation of VISTA imaging features with fluorescent markers on mouse brain tissues. a-d, Parallel images of VISTA (a, c) and fluorescence from lectin-DyLight594 stained blood-vessel (b, d) in vessel-abundant regions. **e-g**, Parallel images of VISTA (e) with two-color fluorescence from lectin-DyLight594 stained vessels (f) and DAPI-stained nuclei (g). **h.** Three-channel merged image from e-g. **i-j**, Parallel images of VISTA (i) and fluorescence from immuno-stained NeuN, the matured neuron marker (j). **k-l**. Parallel images of VISTA (k) and fluorescence from immuno-stained MAP2, the neuronal cell body and dendrite marker (l). All images are shown as maximum intensity projection from a stack of volume images. Scale bars: 40 μm. The length scale is in terms of distance after sample expansion.

High-resolution 3D mapping of the intricate cellular, vasculature, and connectivity network in brain has been a long-sought goal for super-resolved fluorescence microscopy. Imaging such multi-cellular interplay with high throughput would significantly maximize the information value and open new avenues for versatile biological investigations, such as in stroke models and neurodegenerative diseases[25,29-31]. As we were able to assign the origins of protein-abundant structures in VISTA to specific protein targets, we then aimed to transform each identified biological structure in **Fig. 3** into individual components for multi-target analysis through image segmentation. Recently, CNN based deep learning has been implemented for SRS imaging, but mostly focused on denoising and diagnosis prediction[32-35]. The imaging segmentation requires hyperspectral SRS and yet offers limited resolution[33]. Here, we adapted a U-Net based architecture[17,36] and trained our model with parallel VISTA and fluorescence images as input datasets for high-resolution image segmentation. VISTA images (**Fig. 4a, d, g**) were then passed through the trained model, and successfully generated predicted structures (**Fig. 4c, f, i**) that correlate well with fluorescence-labeled ground truth (**Fig. 4b, e, h**) for blood vessels (**Fig. 4c, v-lectin**), nuclei (**Fig. 4f, v-DAPI**), MAP2-immunolabeled neuronal cell bodies and dendrites (**Fig. 4i, v-MAP2**), and NeuN-immunolabeled mature neurons (**Fig. S13**). The quality and contrast of these predicted images are close to the corresponding fluorescence images. The prediction performance is quantified by the Pearson correlation coefficient (**Fig. S14**). We note that the relatively low correlation

values for NeuN prediction were mainly due to the low fluorescence signals obtained, likely caused by the loss of NeuN epitope during protein denaturation. With these 4 individual components successfully predicted, 4-color multiplex imaging is readily obtainable in 3D (**Fig. 4j and Fig. S15**). For more integrated insights of biological organizations, 6-to-7-component imaging could also be achieved on the same sample with an additional 2-to-3 fluorescent colors (**Fig. 4k and Fig. S16**). Compared to conventional label-free imaging, deep learning equipped VISTA offers desired target specificity for multiplex structural analysis. Compared to sample-expansion fluorescence microscopy, which typically requires week-to-month long sample preparation with immunofluorescence[4,6,20,21], sample-processing steps for VISTA are complete within 48 hours (**Fig. S17**). Such high-throughput nature of label-free VISTA imaging by omitting the multi-round immunostaining processes for multi-component investigations would largely facilitate our understanding of the intricate relationship between these cellular and sub-cellular structures deep inside tissues.

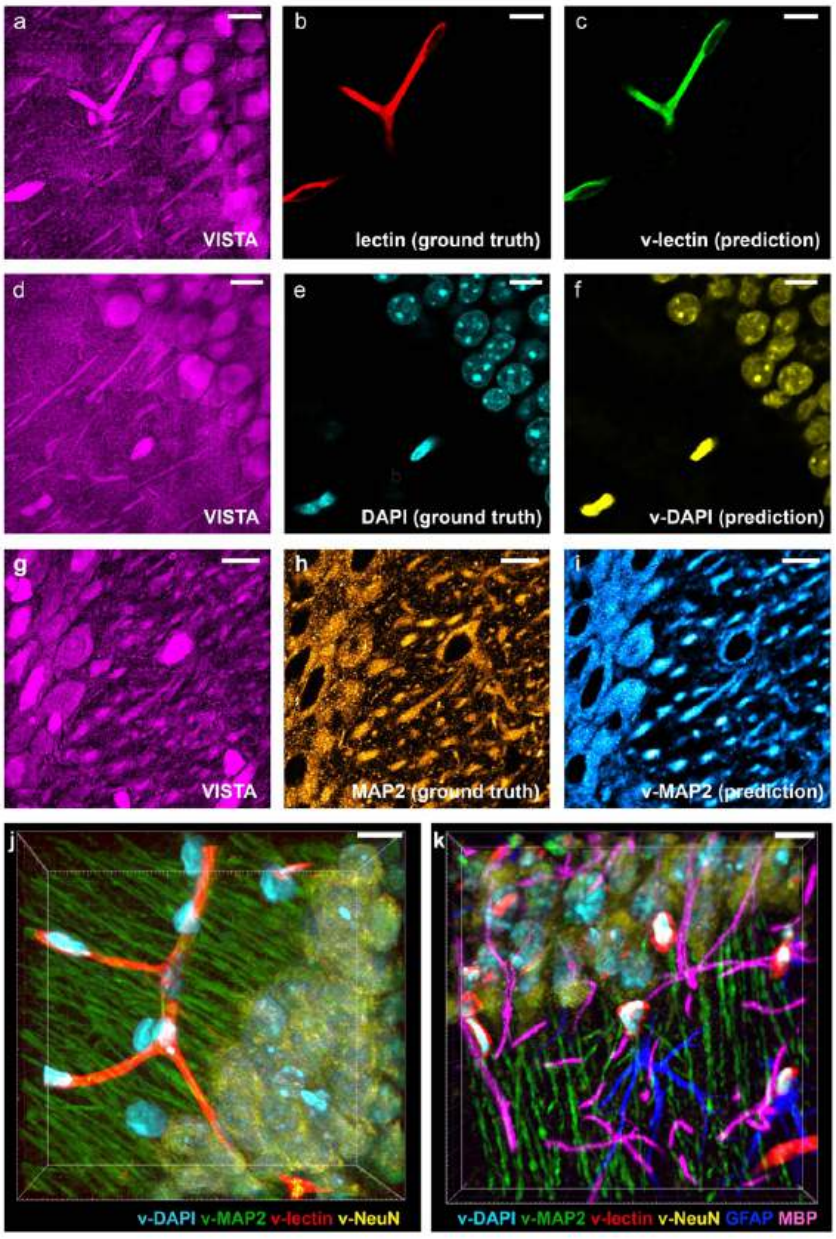

Figure 4. Label-free VISTA prediction for specific and multi-component imaging of brain hippocampal tissues. **a-c**, The input VISTA image (a), the ground truth fluorescence image of lectin-DyLight594 stained blood vessels (b) and the predicted VISTA-lectin (v-lectin) image of blood vessels (c). **d-f**, The input VISTA image (d), the ground truth fluorescence image of DAPI stained

nuclei (e) and the predicted VISTA-DAPI (v-DAPI) image of nuclei (f). **g-i**, The input VISTA image (g), the ground truth immunofluorescence image of MAP2 stained neuronal cell bodies and dendrites (h) and the predicted VISTA-MAP2 (v-MAP2) image of neuronal cells and dendrites (i). **j**, 4-color volume imaging from label-free VISTA prediction for vessels (v-lectin, red), nuclei (v-DAPI, cyan), neuronal cell bodies and dendrites (v-MAP2, green) and matured neuron cell bodies (v-NeuN, yellow). **k**, Tandem 6-color volume imaging from label-free 4-color VISTA prediction and parallel two-color immuno-fluorescence images of GFAP (blue) and MBP (magenta). Scale bars: 40 μm. The length scale is in terms of distance after sample expansion.

2. 4 Discussion

In summary, we established VISTA as a robust and general label-free method for resolving protein-rich cellular and subcellular structures in 3D cells and tissues with an effective imaging resolution down to 82 nm. Targeting the CH_3 vibrational groups from endogenous proteins, VISTA is free from probe bleaching, decay or quenching caused by photo-illumination or gel polymerization and hence suited for repetitive and quantitative interrogations. Implemented with machine learning, VISTA allows specific and multi-component imaging of nuclei, blood vessels, matured neuronal cells and dendrites in brain tissues. VISTA avoids low-efficiency, inhomogeneous delivery, and high cost of fluorescent antibodies, and thus offers fast throughput, uniform imaging

throughout tissues, and cost-effective sample preparation, which scales up better with large human brain samples for future clinical investigations.

A few further technical improvements could be explored to bring VISTA a step forward. It could be coupled with all existing instrument-based high-resolution vibrational imaging techniques for further improvement in resolution. In particular, with a recently reported SRS configuration of frequency-doubled (i.e. wavelength-halved) excitation lasers[37], VISTA should further push the obtainable resolution down to 30 nm. As SRS signals scale nonlinearly with the laser frequency, frequency doubling would allow a 16-time improved sensitivity to resolve lower-protein-abundance structures. In addition to imaging proteins, VISTA could be extended to imaging other types of biomolecules including DNA, RNA, lipids with proper development of molecular anchoring chemistry during sample embedding[38]. With all these features, VISTA should find a wide range of applications for mapping subcellular architectures, cell distributions, and connectivity across various molecular and resolution scales in complex tissues.

1. 5 Protocol

1. Preparation of stock solutions for fixation and sample expansion

1.1. Prepare 40 mL of fixation solution by first dissolving 12 g of acrylamide (30% w/v) solid in 26 mL of nuclease-free water. Then, add 10 mL of 16% PFA stock solution to the mixture. Finally, add 4 mL of 10x phosphate-buffered saline (PBS, pH 7.4). The prepared solution can be stored at 4 ˚C for up to 2 weeks.

NOTE: Acrylamide is hazardous so the step of dissolving acrylamide solid in water should be done in a fume hood.

1.2. Prepare gelation solution (stock X) by dissolving 70 mg of sodium acrylate (7% w/v), 200 mg of acryl amide (20% w/v), and 50 µL of N, N′-methylenebisacrylamide (0.1% w/v) in 420 µL of ultrapure water. Add 57 µL of sterile-filtered 10x PBS (pH 7.4) at the end and store this solution at −20 ˚C for up to 1 week.

NOTE: Avoid sodium acrylate solid that forms clumps; make sure the sodium acrylate used is in the form of dispersive powders. The stock X made will be a colorless liquid; if the liquid looks light yellow, obtain new sodium acrylate.

1.3. Prepare the polymerization initiator solution by dissolving 1 g of ammonium persulfate (APS, 10% w/w) in 9 mL of nuclease-free water. Similarly, prepare polymerization accelerator solution by dissolving 1 g of tetramethylethylenediamine (TEMED, 10% w/w) in 9 mL of nuclease-free water. Aliquot the resulting solutions and store at −20 ˚C.

1.4. Prepare 50 mL of denaturing buffer by dissolving 2.88 g of sodium dodecyl sulfate (SDS, 200 mM), 0.584 g of sodium chloride (200 mM), and 2.5 mL of 1M Tris-HCl buffer (50 mM, pH 8) in nuclease-free water.

NOTE: The concentration of SDS is close to its saturation condition. Some crystallization in the buffer is normal. Slight warming it up to 37 °C can make the solution clear and ready to use.

2. Preparation of mammalian cell samples

2.1. Seed 3.5 x 10^4 HeLa cells onto a 12 mm borosilicate coverslip (#1.5) in a 24-well plate and then culture the cells in 400 µL of Dulbecco's Modified Eagle Medium (DMEM) with 10% fetal bovine serum and 1% penicillin–streptomycin antibiotics (complete DMEM) under a humidified atmosphere with 5% CO_2 at 37 °C.

2.2. To obtain cells in different mitotic stages, incubate the cells in DMEM without fetal bovine serum for 20 h to synchronize the cell stages. Once they reach 60% confluency, switch the medium for the cells to complete DMEM and incubate for another 2–6 h to target various stages of mitosis.

2.3. Wash the HeLa cells on coverslips with sterile PBS and incubate them with fixation solution (4% PFA 30% acrylamide [AA] in PBS) at 37 °C for 7–8 h before further processing.

NOTE: Higher fixation temperature together a with high concentration of acrylamide helps to quench the intermolecular crosslinking between proteins during the fixation processes and is reported to preserve the detailed ultra-structures of proteins[8].

2.4. For cells with polyQ aggregates, grow the cells in complete DMEM until they reach 70%–90% confluency. After changing to new complete DMEM, transfect 1 μg of plasmid encoding mHtt97Q-GFP into the cells using transfection agent (details in **Table of Materials**). Perform transfection according to the manufacturer's protocol.

2.5. After 24–48 h of transfection, remove the culture medium and add 800 μL of fixation solution (4% PFA, 30% AA) to the coverslips with cells. Incubate the coverslips at 37 °C for 6–8 h. Wash the coverslip with PBS 3x, and the resulting cell samples are ready for further processing.

3. Preparation of mouse brain samples

3.1. Purchase C57BL/6J mice (6- to 8-week-old, male and female, six mice) and Alzheimer mice (9-month-old, female, three mice) from commercial sources (details in **Table of Materials**). Perform euthanasia via carbon dioxide narcosis according to standard protocol[27]. In brief, place mice in a chamber and fill the

chamber with a flow of 100% CO_2 in the order of 30%–70% of the volume of the chamber/min and maintain the flow for at least 1 min after clinical death.

3.2. After confirming the humane euthanasia, quickly decapitate the mice using a scissor. Expose the skull with a large incision through the skin down the midline. Pull the skin toward the nose of the animal to fully expose the skull.

3.3. Cut the skull open along the midline with fine scissors and peel the two halves of the skull away to the side. Use tweezers to scoop out the brain into a petri dish on ice with PBS. Wash the fresh mouse brain with ice-cold PBS and transfer the brain to 10 mL of fixation buffer (4% PFA, 30% AA).

3.4. Incubate the mouse brain in fixation buffer at 4 °C for 24–48 h and then transfer it to 37 °C overnight. After washing it with sterile PBS, cut the mouse brain into 150 µm sections using a vibratome and store in PBS at 4 °C.

4. Hydrogel embedding, denaturation, and expansion of cell and tissue samples

4.1. Make sure the samples were incubated in the fixation buffer for the required amount of time, as indicated above. Thaw stock X, free-radical initiator, and accelerator stock solutions and keep them on ice during the whole process.

NOTE: Insufficient incubation time could cause a reduced number of proteins retained on the hydrogel hybrid and, therefore, cause a decrease in signal.

4.2. Pick up the coverslip with cells and place it on a glass slide using tweezers. Pick the brain slices (150 μm thick) and place them on another glass slide using a soft wool paintbrush, ensuring that they are flat. Get rid of excess liquid that comes with the samples.

4.3. Stack two coverslips (#1.5), by adding drops of water between them, on both sides of the sample on the glass slide to make a gelation chamber. Place the glass slide with the sample facing upward onto an ice-cold heat block and cool it to 4 °C for 1 min.

4.4. Add 10% (w/w) TEMED to stock X and then 10% APS solution. Quickly vortex and, within 1 min after mixing, slowly drop the resulting solution into the chamber onto the samples to cover the surface of the sample, avoiding air bubbles. Keep the solution and samples on ice (or an ice-cold heat block) to avoid gel formation (high degree of polymerization) before adding to the sample.

4.5. Once the sample is fully immersed in the solution, place a flat, transparent, film-covered coverslip on top of the sample as a lid for the chamber. Leave the

chamber on ice or an ice-cold heat block for another 1 min before incubating it in a humidifying incubator at 37 °C for 30 min.

4.6. Take out the gelation chamber on the glass slide from the 37 °C incubator. A non-transparent gel should be observed after removing the lid. Retrieve the gel by cutting with a razorblade or, alternatively, put the glass slide into denaturing buffer at room temperature for 15 min. The gel will separate itself from the glass slide.

4.7. Incubate the isolated gel in denaturing buffer under heat conditions to achieve further denaturation and delipidation. For cell samples, denature at 95 °C for 1 h. For 150 μm thick brain slices, denature at 70 °C for 3 h, followed by 95 °C for 1 h.

NOTE: The gel could become curly when first incubated with denaturing buffer at room temperature. It is normal and will become flat after high-temperature denaturation. When working with thicker tissue samples, a longer denaturation time is needed.

4.8. After the heat treatment, wash the denatured sample 3 times with PBS for 10 min. At this point, the gel should have expanded to about 1.5 times the original size. Incubate the washed gel with ultrapure water in a large container (at least 20 times the volume of the gel) to achieve a higher expansion ratio. Change the

water every 1 h 3x and leave the sample in darkness overnight. The resulting gel is ready to image.

NOTE: The expansion ratio largely depends on the mechanical properties of the original sample. A 4.2 times expansion for the cell samples and 3.4 times expansion for the brain tissue sample were obtained.

5. Label-free imaging of endogenous protein distribution in expanded cell and tissue samples

5.1. Keep the expanded gel samples in water during the imaging process. The gel is fragile after expansion and so should be handled with caution. Place the expanded sample-bearing gel onto a microscope slide (1 mm thick) with a microscope spacer with appropriate opening sizes and depths, filled with water. Cover the spacer with a coverslip (#1.5) and ensure it is properly sealed to avoid sample movement.

5.2. Place the sample with either the expanded cell or tissue onto the motorized stage with the coverslip facing the objective. Click **Ocular** on the software to change the light path to bright field and adjust the z position using a manual knob.

5.3. Add immersion oil on the top of the sample and adjust the condenser to the correct position for Köhler illumination while watching under bright field with

25x magnification from the objective. Input 791.3 nm in the OPO wavelength window on the laser panel to target protein CH_3 vibration at 2940 cm^{-1}.

5.4. Switch the light of the microscope from bright field (eye piece) to laser scanning mode by clicking the **LSM** button and open the SRS laser shutter by hitting the **Shutter** button on the laser control panel. Press the **LIVE** button in the microscope software to start real-time image acquisition.

5.5. Find the proper focus by changing the z while looking at the SRS image under short pixel-dwell time (12.5 µs/pixel) and low image resolution (256 pixels x 256 pixels). Once the ideal z-position is found, change the scan size and pixel-dwell time by pulling the respective bar in the microscope software.

5.6. Acquire the image by hitting the **LSM** button using the super-sampling condition (1024 pixels x 1024 pixels) with a longer pixel-dwell time (80 µs/pixel) that matches the time constant of the lock-in amplifier. Acquire volumetric images by collecting a z-stack with a step size of 1 µm in the z-direction. Process and analyze the saved OIR file from the software using ImageJ.

NOTE: The detailed SRS setup has recently been reported in Mutlu et al.[24]. Here, use a tunable picosecond laser (770–990 nm) with an 80 MHz repetition rate for the pump and Stokes (1031.2 nm) excitation lasers in a laser scanning confocal microscope (detailed in **Table of Materials**). Optimize the temporal

and spatial overlapping of the two beams for signals with pure D_2O. It takes some effort to find the right z for the expanded sample under bright field because the refractive index is very homogenous throughout the gel.

5.7. Determine the resolution of VISTA by taking an SRS image of polystyrene beads (100 nm) using both a 25x objective and a 60x objective. Set the pump laser to 784.5 nm, corresponding to Raman shift of 3050 cm^{-1}, characteristic of the aromatic C-H stretches vibrations of polystyrene.

NOTE: The pump laser wavelength used here is similar to the one used in VISTA for proteins.

5.8. With the 60x objective, the experimental full wave half maximum (FWHM, which is the width of the line shape at half of the amplitude) of the bead image was 276.17 nm. Model the function of the bead object as a half-circle.

NOTE: When the PSF Gaussian function has a c (σ) = 269 nm/2.35, the convoluted bead image would have a measured FWHM of 276.17 nm. As a result, the resolution of the SRS system is 269 nm × 1.22 = 328 nm by the Rayleigh Criterion. As VISTA has an average of 4.2 times expansion of cell samples, the effective resolution is down to 328 nm/4.2 = 78 nm.

6. Correlative VISTA and fluorescent imaging of immuno-labeled and expanded tissue samples

6.1 After denaturation, pre-incubate the hydrogel embedded samples (e.g., 150 μm brain coronal section) in 1% (v/v) Triton X-100 (PBST) for 15 min. Switch the incubation buffer to PBST with primary antibody at a 1:100 dilution. If multiple protein targets are needed for multiplex imaging, dilute respective primary antibodies for different targets to proper concentrations in the same cocktail and incubate with the samples simultaneously.

6.2 Incubate the gels with diluted primary antibodies at 37 °C with gentle shaking at 80 rpm for 16–18 h, followed by extensive washing 3x with PBST for 1–2 h at 37 °C. Flip over the gel during the incubation to prevent inhomogeneous antibody labeling here and in all subsequent incubations.

6.2 Incubate the samples with secondary antibodies of corresponding species targets at 1:100 dilutions with PBST at 37 °C for 12–16 h, protected from the light. Wash labeled hydrogel samples 3x with PBST for 1–2 h at 37 °C with gentle shaking.

6.3 Dilute DAPI to 3 μM final concentration in PBS. Add a sufficient volume of DAPI solution to the sample hydrogel so that the gel is submerged in the solution.

Incubate for 1–2 h at room temperature with gentle shaking at 80 rpm. Wash the sample 3x with PBS.

6.4 Expand the immuno-labeled gel samples by incubating with a large volume of double deionized H_2O. Change the water every 1 h 3x and incubate the samples in H_2O overnight, protected from light. During labeling, the gel should expand 1.5 times compared to the PBS buffer.

6.5 Prepare the imaging sample as described in step 5.1. Place the imaging sample onto the laser scanning confocal microscope with the 25x, 1.05 NA, water immersion objective for fluorescent imaging.

6.6 Select the proper channel with the respective excitation laser (405 nm, 488 nm, 561 nm, and 640 nm) and PMT pair according to the targeted antibodies in the dropdown menu on the microscope software. Press the **LIVE** button for real-time image acquisition.

6.7 Adjust the focus position by a manual knob based on the real-time fluorescence signal. Optimize the laser power, pixel-dwell time, and PMT gain in the microscope software according to the real-time fluorescence signal to avoid a dim signal or oversaturation.

NOTE: Evaluate the appearance and features based on the reported structures of different antibodies to eliminate potential antibody cross-reactivities and to avoid crosstalk between different fluorescence channels.

6.8 Hit the **LSM** button to start acquiring correlative SRS and fluorescent images. First, collect volumetric fluorescence images on immuno-labeled samples. Once fluorescence imaging is finished, switch the microscope light path to the infrared (IR) transparent condition.

6.9 Change the detection channel from fluorescence PMT to SRS on the microscope software. Open the shutter for the SRS laser and perform SRS volumetric imaging on the field of view of the same sample with the same range of z. The normal range is between 100–200 μm and can go up to 700 μm.

NOTE: There is slight chromatic aberration that causes a shift in z-position between the fluorescent images and the SRS images because of the wavelength difference in the excitation lasers. Manual side-by-side comparison between the SRS and fluorescence z-stack images is needed. Look for the exact matching features from both the SRS and the fluorescence channel to match the z-position precisely.

7. Construction, training, and validation of U-Net architecture

NOTE: Installation on Linux is recommended. A graphics card with >10 GB of RAM is required.

7.1 Setting up the environment

7.1.1. Install Anaconda or Miniconda on a 3-5.3.0-linux-x86_64. Clone or download the following files: https://github.com/Li-En-Good/VISTA. Create a Conda environment for the platform using the following command line*:*

conda env create -f environment.yml

7.2. Training the prediction model

7.2.1. Pair the directories of corresponding SRS images with ground truth images in a csv file. Place the directories of SRS images under path_signal and ground truth images under path_target columns.

7.2.2. Put the csv file in the folder data/csvs. Modify the configuration in scripts/train_model_2d.sh if needed. Activate the environment using the command line:

conda activate fnet

7.2.3. Initiate model training using the command line:

./scripts/train_model_2d.sh <file name of the csv file> 0

The training will then start. The losses for each iteration will be shown in the command line and saved with the model in the folder save_models/<file name for the csv file>.

7.3. Validate the images in the training set and test set using the command line:

./scripts/train_model_2d.sh <file name of the csv file> 0

The prediction results will be saved in the folder results/<file name of the csv file>.

8. VISTA combined with U-Net predictions for protein-specific multiplexity in label-free images

8.1 Modify the csv file in data/csvs/<file name of the csv file>/test.csv. Replace the directories of both path_signal and path_target with the directory of new SRS images.

8.2 Remove the prediction results from the training, which is the folder results/<file name of the csv file>. Run predictions using the command line:

./scripts/train_model_2d.sh <file name of the csv file> 0

The prediction results will be saved in the folder results/<file name of the csv file>/test.

1. 6 Methods and materials

SRS microscopy

A picoEmerald laser system (Applied Physics & Electronics) is used as the light source for SRS microscopy. It produces 2 ps pump (tunable from 770–990 nm, bandwidth 0.5 nm, spectral bandwidth ~7 cm−1) and Stokes (1031.2 nm, spectral bandwidth 10 cm−1) beams with an 80 MHz repetition rate. Stokes beam is modulated at 20 MHz by an internal electro-optic modulator. The spatially and temporally overlapped pump and Stokes beams are introduced into an inverted multiphoton laser scanning microscope (FV3000, Olympus), and then focused onto the sample by a 25× water objective (XLPLN25XWMP, 1.05 N.A., Olympus) for imaging. Transmitted Pump and Stokes beams are collected by a high N.A. condenser lens (oil immersion, 1.4 N.A., Olympus) and pass through a bandpass filter (893/209 BrightLine, 25 mm, Semrock) to filter out Stokes beam. A large area (10 × 10 mm) Si photodiode (S3590-09, Hamamatsu) is used to measure the pump beam intensity. A 64 V reverse-bias DC voltage is applied on the photodiode to increase the saturation threshold and reduce response time. The output current is terminated by a 50-Ω terminator and pre-filtered by a 19.2–23.6-MHz band-pass filter (BBP-21.4+, Mini-Circuits) to reduce laser and scanning noise.

The signal is then demodulated by a lock-in amplifier (SR844, Stanford Research Systems) at the modulation frequency. The in-phase X output is fed back to the Olympus IO interface box (FV30-ANALOG) of the microscope. Image acquisition speed is limited by a 30 μs time constant set for the lock-in amplifier.

Correspondingly, we use 80 μs pixel dwell time, which gives a speed of 21 s per frame for a 512-by-512-pixel field of view. Pump laser is tuned to 791.3 nm for imaging protein CH3 vibrational mode at 2940 cm−1. Laser powers on the sample are measured to be 30 mW for the Pump beam and 200 mW for modulated Stokes beam. Sixteen-bit greyscale images are acquired by Olympus Fluoview 3000 software. Volumetric images were acquired by collecting a z-stack with a step size of 1 micron in the z-direction.

Reagents and materials

Sodium acrylate (SA, Sigma-Aldrich), acrylamide (AA, Sigma-Aldrich), N,N′-methylenebisacrylamide (BIS, 2%; Sigma-Aldrich), ammonium persulfate (APS, Sigma-Aldrich), tetramethylethylenediamine (TEMED, Sigma-Aldrich), sodium dodecyl sulfate (SDS), Triton X-100, Tween-20, and deuterium oxide were obtained from Sigma-Aldrich, and 1.0 M Tris was obtained from Biosolve. Nuclease-free water was purchased from Ambion–Thermo Fisher. Acrylamide (2,3,3-D3) was obtained from Cambridge Isotope Laboratories. Deuterated sodium acrylate was prepared from acrylic acid (2,3,3-D3, Cambridge Isotope Laboratories) and sodium hydroxide (Sigma-Aldrich). DAPI was purchased from Thermo Fisher (D1306, Thermo Fisher). Primary antibodies: anti-MBP in rat (Abcam, ab7349); anti- MBP in rabbit (Abcam, ab40390); anti-GFAP in chicken (Abcam, ab4674); anti-chicken IgY, Alexa 488 (Invitrogen, A-32931); anti-GFP Alexa Fluor 647 (Invitrogen, A-31852); anti-MAP2 (Cell Signaling Technology,8707); anti-NeuN (Cell Signaling Technology, 24307); anti-GLUT-1

(Millipore SigMBPma, 07-1401); Lycopersicon Esculentum Lectin DyLight®594 (Vector Laboratories, DL-1177-1). Secondary antibodies: goat anti-rat IgG, Alexa Fluor 568 (Invitrogen, A-11077); goat anti-mouse IgG, Alexa Fluor 647 (Invitrogen, A-21236); goat anti-rabbit IgG, Alexa Fluor 488 (Invitrogen, A-11034); goat anti-chicken IgY, Alexa Fluor 647 (Invitrogen, A-21449).

Hydrogel embedding: gelation, denaturation, and expansion

Stock solutions include an incubation solution (30% AA in 4% PFA), and a gelation solution (7% SA, 20% AA, 0.1% BIS in 1× phosphate-buffered saline (PBS)) were made and stored at 4 °C and −20 °C, respectively. The free-radical initiator APS and accelerator TEMED were dissolved and diluted in nuclease-free water to a concentration of 10% (w/w), and stored at −20 °C as stocks. Prior to a typical hydrogel embedding step, the cell or tissue samples were incubated in a solution of 30% AA in 4% PFA under different conditions depending on the sample type (detailed in the following sections). The gelation solution, the free-radical initiator, and accelerator were thawed and kept at 4 °C before the gelation step. Coverslips with the cell or tissue samples were placed at the bottom of a pre-fabricated and pre-cooled gelation chamber, with the sample facing upward. After adding a sufficient amount of gelation solution (7% SA, 20% AA, 0.1% BIS in 1× PBS) to fully immerse the sample, a layer of flat Parafilm-covered coverslip was placed on top of the chamber as the lid. The chamber was kept at 4 °C for 1 min as the free-radical polymerization proceeded before it was transferred to a humid incubator for the following incubation at 37 °C for 1 h. Coverslips with gels were

then incubated insufficient amount of denaturing buffer (200 mM SDS, 200 mM NaCl, and 50 mM Tris in nuclease-free water, pH 8) in Petri dishes for 15 min at room temperature. The volume of the denaturing buffer and the size of the Petri dishes used were determined by the sample size and thickness after denaturation. In 15 min, gels would be detached from the coverslips. They were transferred into 1.5-ml Eppendorf centrifuge tubes filled with denaturing buffer and were incubated under different conditions depending on the sample type (detailed in the following sections). Initial expansions were carried out immediately after the denaturation step at ambient temperature, in H2O or D2O, which was changed twice in 1 h. The expanded gel was then kept in H2O or D2O overnight and stored in the dark. The gel expanded 4.0 ± 0.22 times in our experiments.

Cultured HeLa cell experiments

In mammalian cell experiments, cultured HeLa-CCL2 (ATCC) were seeded onto coverslips (12 mm, #1.5, Fisher) for 24 h. Cells were first grown in regular DMEM medium supplemented with 10% fetal bovine serum and 1% penicillin–streptomycin antibiotics until they reached 70–90% confluency. Coverslips with HeLa cells were incubated in a solution of 4% PFA with 30% AA in PBS for 7–8 h at 37 °C, without normal fixation with PFA. Hydrogel embedding, including gelation, denaturation, and expansion, was processed in the above-mentioned steps. The denaturation after transfer into Eppendorf centrifuge tubes was at 95 °C for 30 min.

Normal brain tissue experiments

Mouse brains tissues harvested from mice were washed once with DPBS on ice and immediately incubated in a solution of 4% PFA with 30% AA in PBS for 24–30 h at 4 °C, then transferred to a shaker and further incubated for 12 h at 37 °C with gentle shaking. After the incubation step, the tissue sample was cut into 100–250 μm thin slices (and thick slices up to 600–650 μm, for thick brain tissue experiments) using a Leica VT 1200S vibratome. Hydrogel embedding, including gelation, denaturation, and expansion, was processed in the above-mentioned steps. The denaturation after transfer into Eppendorf centrifuge tubes was first at 70 °C for 3 h and then at 95 °C for 1 h.

Zebrafish embryo experiments

Fresh zebrafish embryo samples were embedded in gelatin and snap-frozen in liquid nitrogen and stored at −80 °C until ready for sectioning. Immediately before sectioning, the whole gelatin embedded sample was allowed to warm up to −30 °C for 10 min in the cryostat. Cryosectioning was carried out on the whole frozen block, and sectioned slices were collected onto the glass slides at room temperature. The glass slides with collected sample slices were stored at −20 °C until ready for de-gelatinization and hydrogel embedding. When ready, the slides were warmed up to room temperature, and then de-gelatinized by incubation in PBS at 42 °C for 30 min. The de-gelatinized samples were washed in PBS with 0.1% Tween-20 before processing. Hydrogel embedding, including gelation,

denaturation, and expansion, was processed in the above-mentioned steps. For thin (50-μm) slices of the zebrafish embryo we used, the denaturation after transfer into Eppendorf centrifuge tubes was at 95 °C for 30 min.

Thick brain tissue experiments

Thick brain tissues were cut to slices with a thickness of at least 250 μm (1000 μm after expansion). PFA + AA incubation and hydrogel embedding, including gelation, denaturation, and expansion, were processed in the above-mentioned steps similar to the normal tissue processing. The denaturation after transfer into Eppendorf centrifuge tubes was first at 70 °C for 3 h and then at 95 °C for 4 h. Thicker tissue can also be imaged by VISTA with a longer 95 °C denaturation time.

Immunostaining

In an immuno-labeling process, 60-μm- to 150-μm-thick mouse brain coronal slices were embedded in a hydrogel, denatured, pre-incubated with PBS with 1% (wt/vol) Triton X-100 (PBST) for 15 min, and subsequently incubated with primary antibodies at a typical 1:100 dilution with PBST at 37 °C for 16 h, followed by washing with PBST three times at 37 °C for 1–2 h. The samples were then incubated with secondary antibodies at a 1:100 dilution with PBST at 37 °C for 12–16 h, followed by washing with PBST three times at 37 °C for 1–2 h.

Sample mounting and imaging

Expanded cell or tissue samples were kept in D2O/H2O for imaging. Grace Bio-Labs Press-To-Seal silicone isolators with appropriate opening sizes and depths were used as spacers between microscope slides (1 mm, VWR) and coverslips (12 mm, #1.5, Fisher). In particular, the thick brain tissue samples (after expansion) were placed in a 4-mm silicon isolator to avoid any pressure and damage to the sample. For control experiments on normal PFA fixed HeLa cells, 0.5-mm Press-To-Seal silicone isolators or the common Grace Bio-Labs SecureSeal™ spacers were used. Confocal images were obtained by the Olympus FluoView™ FV3000 confocal microscope with the SRS setup described above.

SRS imaging of beads

Polystyrene beads (0.1 μm mean particle size, Sigma-Aldrich, Inc.) were resuspended in deionized water by a 1:2000 dilution. The resuspension step required vortexing and sonication for 20 min at room temperature. Before SRS imaging, the diluted beads suspension was sealed between a glass slide and a coverslip, which was then stored in the dark and left to settle overnight.

Image processing and data analysis

Images color-coding and intensity profile were done by ImageJ. Intensity normalization of the z-stacks was done in ImageJ. 3D rendering of z-stacks was done in Imaris View. Data plotting and analysis, including spectral plots and Gaussian fitting, were performed in OriginLab.

Calculating the resolution of SRS microscopy and the VISTA method

To determine the point spread function (PSF) of the imaging system, deconvolution of the actual size of the beads was done by simulations in MATLAB 2018b. The line profile of the bead image was fitted by Gaussian approximation and the beaded object was modeled as a circle.

Fluorescence imaging

The fluorescence images of processed samples with fluorescent labels were obtained with a 25×, 1.05 NA water-immersion objective with the Olympus Fluoview system. Single-photon confocal laser scanning imaging was performed with 405-, 488-, 561-, and 640-nm lasers (Coherent OBIS). The images were visualized and analyzed with Fiji or Imaris Viewer.

U-Net construction, training, and prediction for label-free imaging

The prediction of subcellular structures from SRS images was based on a U-Net CNN demonstrated by Ounkomol et al.17. Training data were collected by sequentially acquiring respective fluorescence targets and protein SRS images on the same field of view. Image sets were generated by performing a z scan with a z-direction step size of 1 micron. Such a step size is larger than the axial resolutions of both fluorescence and SRS. Before training, the fluorescence and SRS images were background subtracted in ImageJ with a rolling ball radius of 50 pixels (0.497 microns/pixel) before training. The image sets (minimum 200 sets

for each channel) were separated randomly at a 1:3 ratio for testing and training set, respectively. The models were trained by batches of 128 pixels × 128 pixels patches subsampled from the original images. The training was performed using the Adam optimizer to optimize the mean squared error between the fluorescence image and the predicted image. The learning rate set at 0.001 and trained for 50,000 epochs with a batch size of 32 images. All the training and predictions were run on a node of the High-Performance Computing Center at Caltech equipped with Nvidia P100 GPU containing 16 GB of memory. The trained algorithm was applied across different samples with no further adjustments.

Model accuracy

Model accuracy was quantified by the Pearson correlation coefficient between the pixel intensities of the model's output, y, and independent ground-truth test images, x, for all the images of the test sets except for lectin. The Pearson correlation coefficient for lectin was calculated for images with lectin signal since the random noise in the background could not be predicted by the model.

We also quantified the contribution of the noise from the ground-truth fluorescence images to the prediction performance (i.e., the Pearson's r) by our model39. We establish that our model accuracy (i.e. the Pearson's r) decreases as the noise of training-set ground truth increases.

Animals

All animal procedures performed in this study were approved by the California Institute of Technology Institutional Animal Care and Use Committee (IACUC), and we have complied with all relevant ethical regulations. The C57BL/6J (000664), Thy1-YFP (003709) mouse lines used in this study were purchased from the Jackson Laboratory (JAX) and bred in our animal facility. 6- to 8-week-old male and female C57BL/6J, Thy1-YFP mice were used for tissue collection. On the day of collection, the mice were anesthetized with Euthasol (pentobarbital sodium and phenytoin sodium solution, Virbac AH) and transcardially perfused with 30–50 mL of 0.1 M PBS (pH 7.4). After this procedure, the brains were harvested and proceeded to VISTA processing.

Statistics and reproducibility

For all imaging experiments yielding the micrographs reported herein, at least three independent experiments were repeated with similar results.

1. 7 Supplementary information

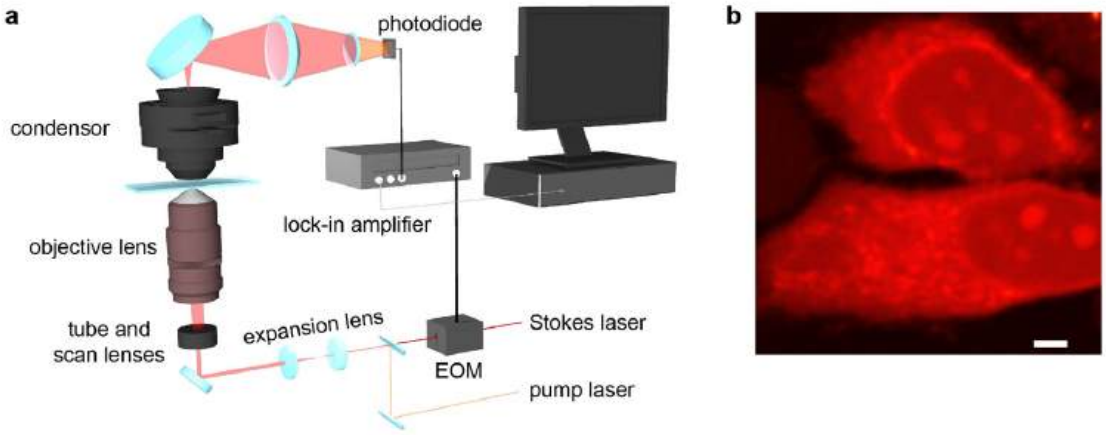

Supplementary Figure 1. Setup for the stimulated Raman scattering (SRS) microscopy. (a) Instrumental setup of SRS microscope. EOM: Electro-Optic Modulator. When the energy difference between the Pump laser photons and the Stokes laser photons matches with the vibrational frequency of target chemical bonds (e.g. 2940 cm-1 for the symmetric vibrational motion of CH3), the chemical bonds are efficiently driven from the vibrational ground state to the vibrational excited state, creating stimulated Raman loss in pump beam, which is subsequently detected by a photodiode and provides the imaging contrast. (b) A representative regular-resolution SRS image of HeLa cells targeting the protein CH3 vibration at 2940 cm-1. Scale bar: 3 μm.

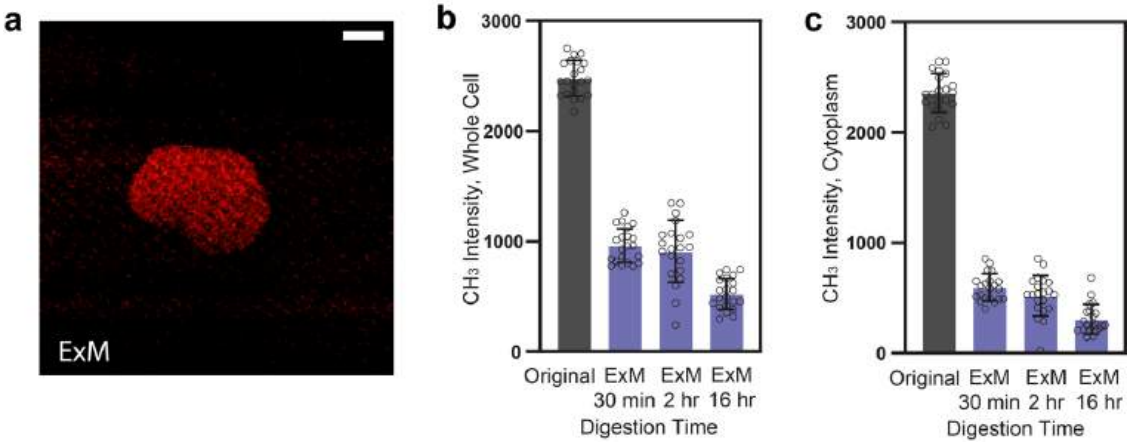

Supplementary Figure 2. SRS quantification of protein loss following the ExM protocol. (a) Contrast-enhanced SRS image for Fig. 1c with a 2-time enhancement on the intensity scale. Scale bar: 20 μm. The length scale is in terms of distance after sample expansion. (b)-(c) Quantification of protein retention level on different protease digestion time by proteinase K on whole cells (b) and from the cytoplasm (c). SRS images of protein CH3 from HeLa cells were

acquired after designated digestion times. The protein signals decrease rapidly upon protease treatment, confirming that the digestion step in ExM causes significant protein loss. For each digestion time, n=21 cells were examined over three independent experiments. Data shown as mean ± SD.

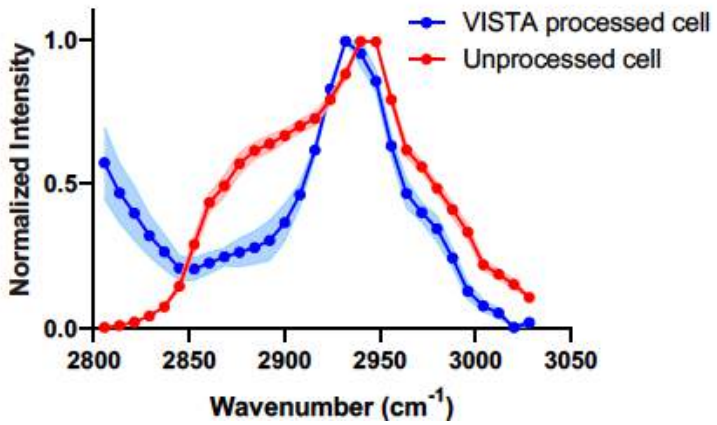

Supplementary Figure 3. Hyperspectral SRS from HeLa cells with and without VISTA processing. The spectra were acquired by sweeping pump laser wavelength with 0.5 nm step size from 783.3 to 799.8 nm, with Stokes laser fixed at 1031.2 nm. The evident loss of lipid peak at 2855 cm-1 between normalized SRS spectra from unprocessed cells (red) and VISTA processed cells (blue) confirms the loss of lipid content from the protein denaturation step, which washes out the lipids. The intact peak shape for CH3 at 2940 cm-1 confirms that VISTA retains proteins. The shoulder around 2800 cm-1 for VISTA processed cell spectrum (blue) originates from D2O. VISTA processed cell, N=10; unprocessed cell, N=15. Data shown as mean ± SD.

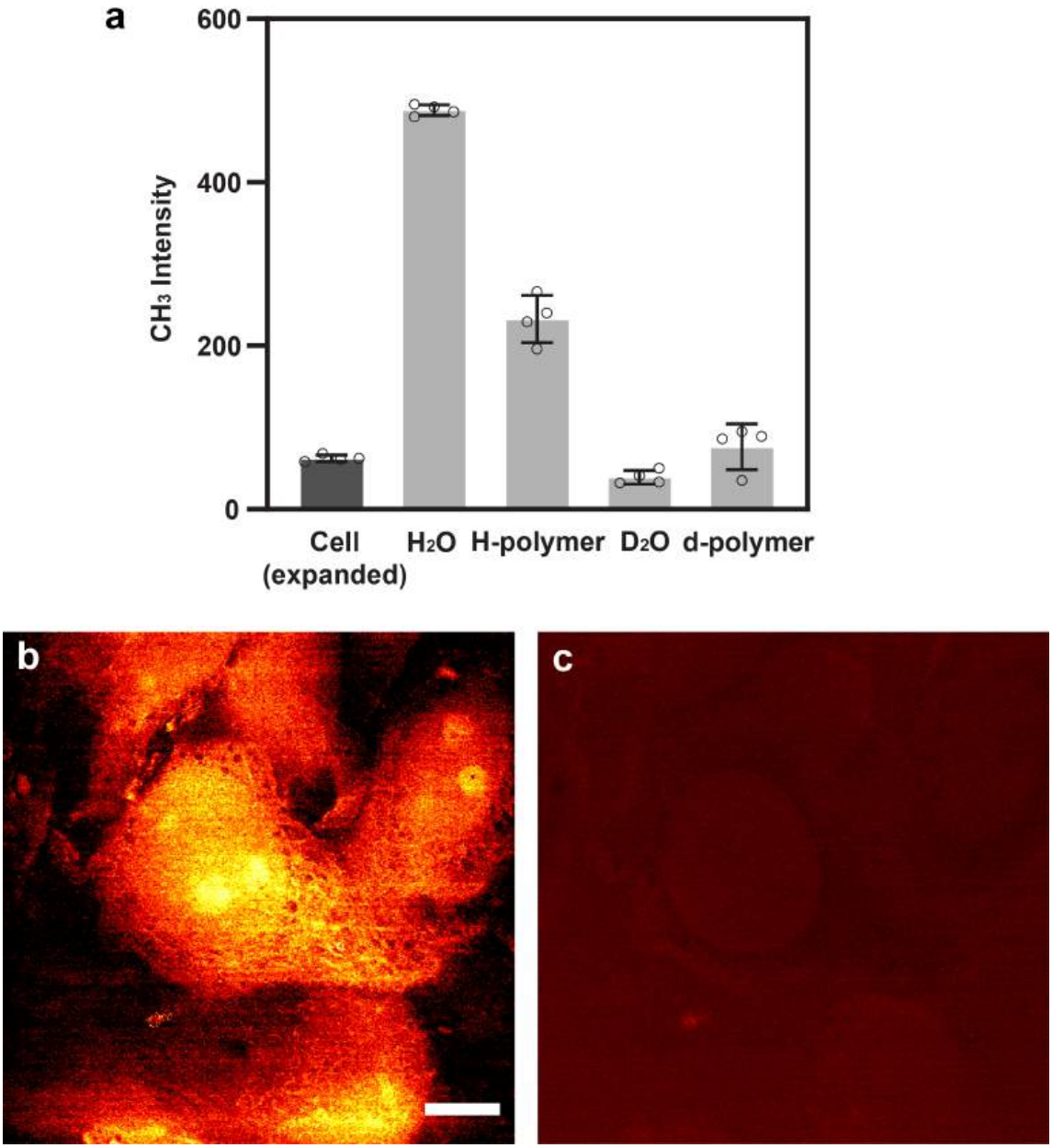

Supplementary Figure 4. Quantification of backgrounds in VISTA CH3 images on HeLa cells. (a) Background contributions from each component (i.e. OH stretch tail from H2O and CH vibrations from the polymers composed of sodium acrylate and acrylamide monomers) were obtained by comparing normal VISTA cell images with VISTA images using corresponding deuterated

components. The change of the backgrounds is constant across field of views after deuteration. For each component, n=4 samples were examined over four independent experiments. Data shown as mean ± SD. (b-c) Representative VISTA images from expanded HeLa cells embedded in the deuterated polymer at the CH3, 2940 cm-1 channel for cellular distributions (b) and the corresponding CD, 2176 cm-1 channel for deuterated polymers (c). Scale bar: 20 μm

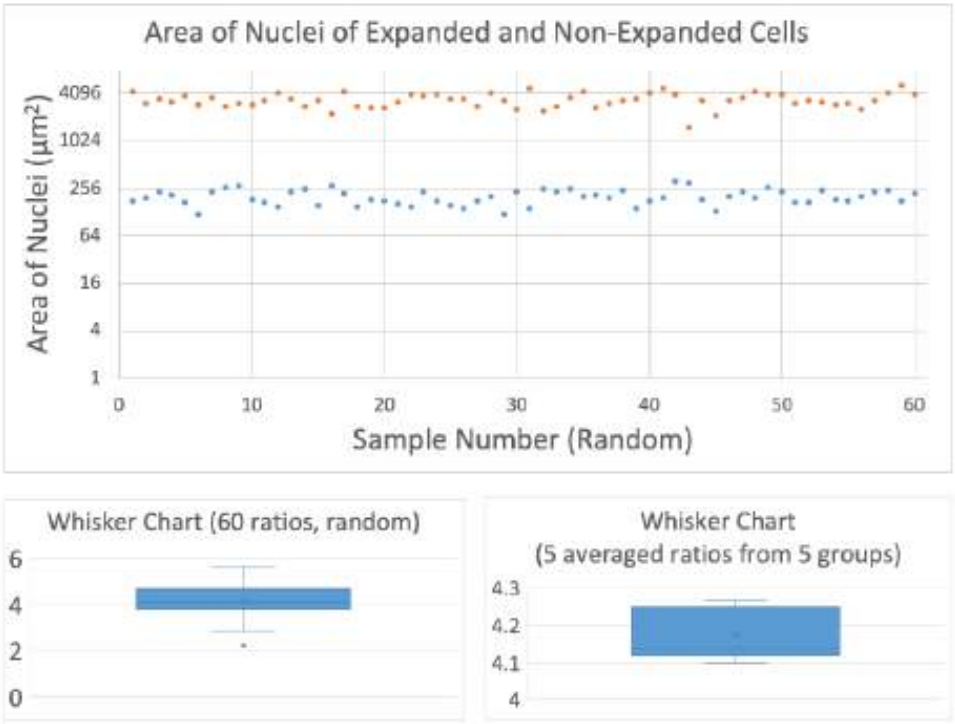

Supplementary Figure 5. Statistical quantification of the average expansion ratio for cell samples by VISTA. Top: Areas of randomly chosen 60 expanded (orange) and non-expanded (blue) cells across 5 individual sample groups. Bottom: statistics with whisker charts for calculation of the average expansion ratios on cells. The left whisker chart (4.2±0.7) is calculated based on total 60

random expanded vs non-expanded pairs, and the right one (4.2±0.1) is calculated based on 5 averaged ratios from the 5 sample groups (12 cells in each group). For the box plots, top/bottom of vertical line is the maxima/minima, center line is median, x in the box is mean, and the top/bottom of box is median of the top/bottom half (3rd quartile/1st quartile).

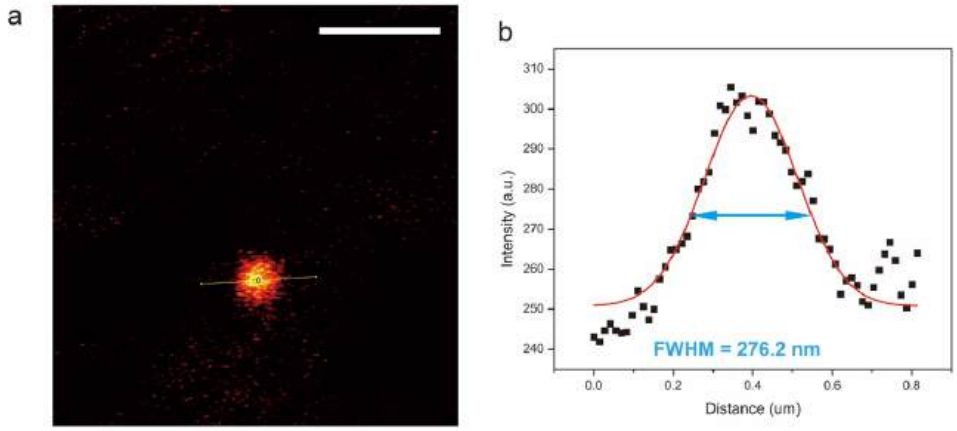

Supplementary Figure 6. Quantification of SRS resolution under a higher numerical aperture (NA) objective lens. A representative image (a) and the corresponding fitted crosssection profile (FWHM of 276.2nm) (b) from a 100-nm polystyrene bead, by targeting the C-H vibration at 3050 cm-1 with a 60X water objective (Olympus, UPLSAPO60XWIR, 1.2 NA). Scale bar: 2 μm.

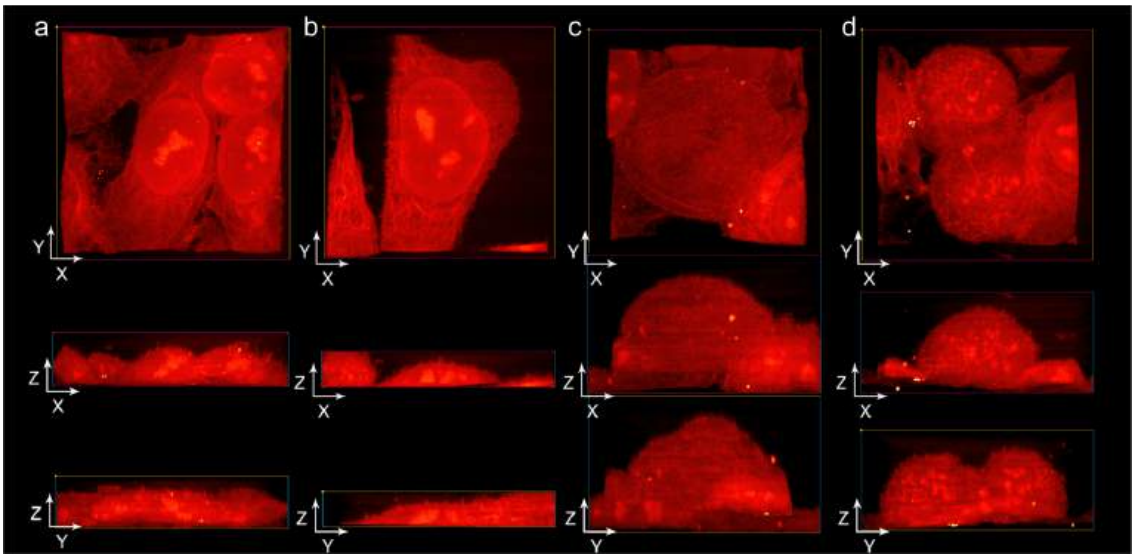

Supplementary Figure 7. High-resolution three-dimensional VISTA views of cellular morphology and subcellular structures of interphase and mitotic HeLa cells. (a-b) Volume HeLa cells at interphase. The network structure in the cytoplasm is clear. In the x-z view, minor upward extrusions from cell surface (zx view) were also captured. (c-d) Volume HeLa cells during mitosis for single-z images shown in Fig. 2b and Fig. 2d.

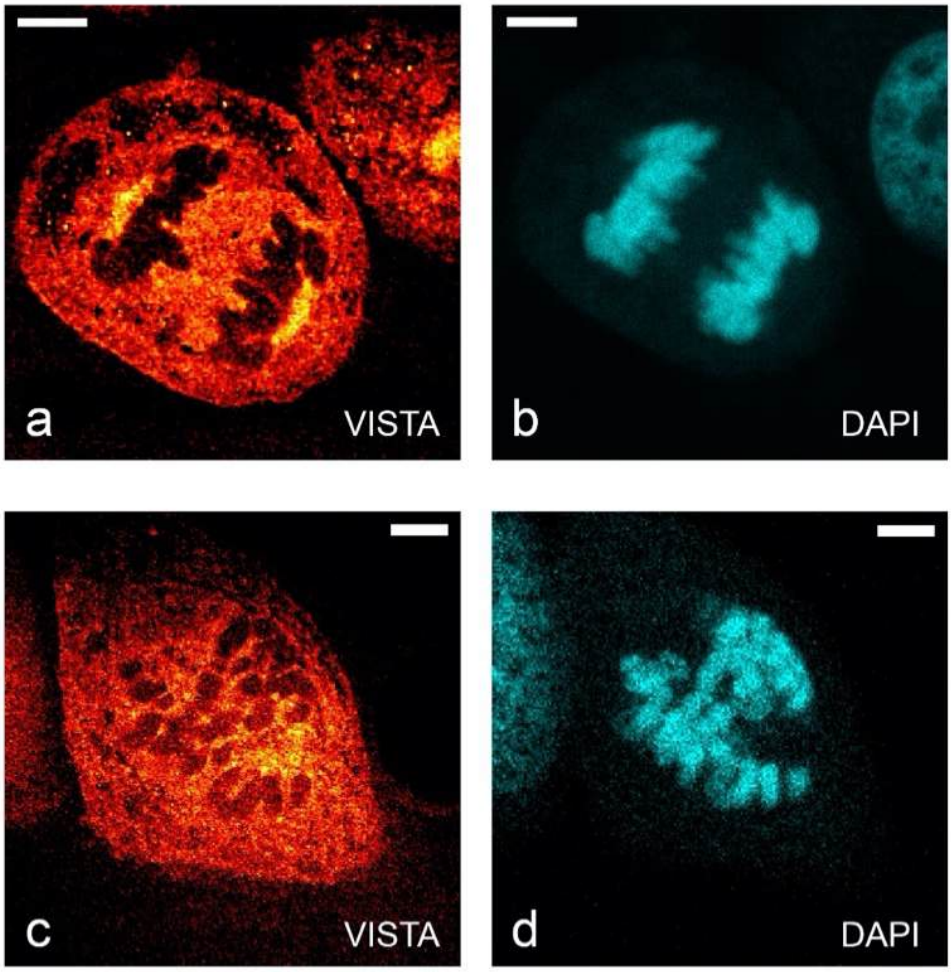

Supplementary Figure 8. Correlative VISTA images and the fluorescent images with DAPI stain on mitotic HeLa cells. Fluorescent DAPI stains confirms that the dark regions shown in VISTA images on anaphase (a-b) and prophase (c-d) HeLa cells are chromosomes with a low CH3 signals (i.e. low protein contents). Scale bars: 20 μm. The length scale is in terms of distance after sample expansion.

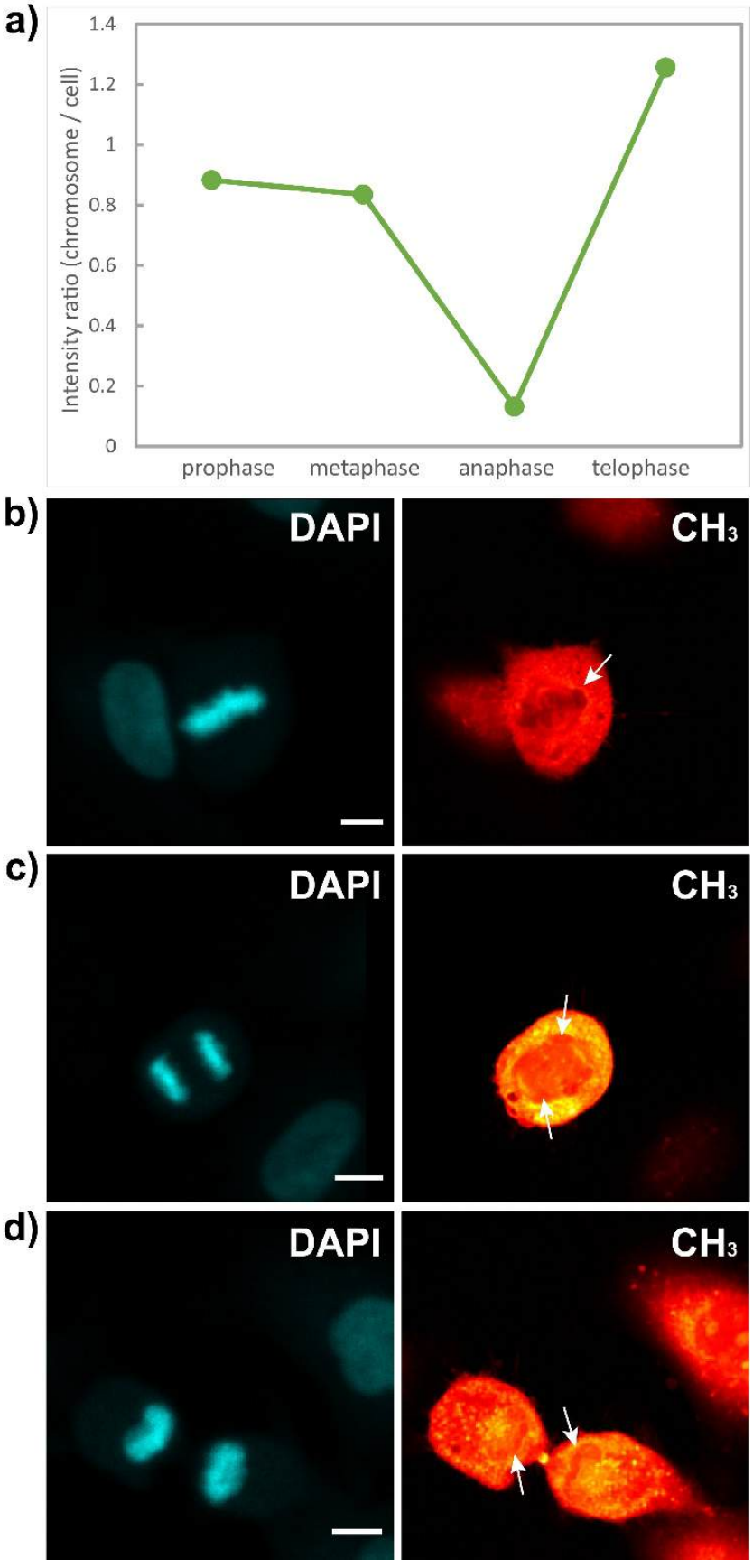
a)
Intensity ratio (chromosome / cell)
1.4
1.2
1
0.8
0.6
0.4
0.2
0
prophase
metaphase
anaphase
telophase
b)
DAPI
CH3
c)
DAPI
CH3
d)
DAPI
CH3

Supplementary Figure 9. Confirmation of protein abundance change in the chromosomal regions in HeLa cells throughout mitosis. (a) Quantification of relative protein abundance in chromosomal regions in reference to the protein CH3 signals from the whole cells (i.e. the chromosome/cell ratio) for expanded HeLa cells across different stages of mitosis, shown in Fig. 2a-d. (prophase: 0.88; metaphase: 0.83; anaphase: 0.14; telophase: 1.26). (b-d) SRS images (CH3, 2940 cm-1) and correlative DAPI-stain fluorescence images of PFA-fixed but unprocessed mitotic HeLa cells in metaphase (b), anaphase (c), and telophase (d). Arrows indicate corresponding chromosome regions in the SRS images guided by DAPI fluorescence stain. Scale bars: 10 μm.

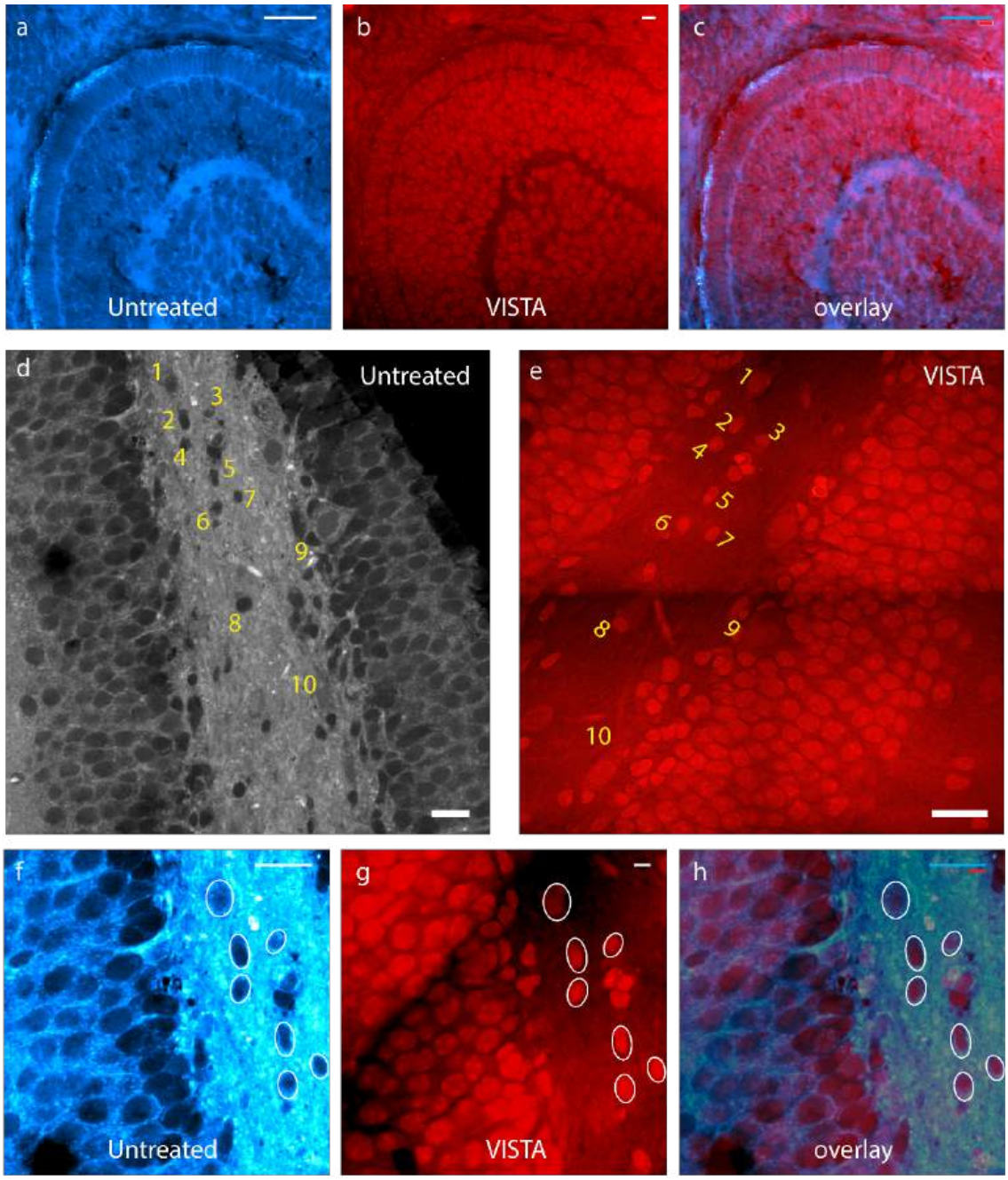

Supplementary Figure 10. Imaging registrations for tissues before and after expansion. (a-c) SRS imaging of an untreated zebrafish retina tissue (a), VISTA imaging of the same sample (b), and the overlay (e). (d-e) SRS imaging of an untreated mouse brain tissue (a) and VISTA image of the same sample (b), with

labels of nine correlating features for expansion ratio calculation. (f-h) SRS imaging of an untreated brain tissue (a), VISTA imaging of the same sample (b), and the overlay (e). White circles indicate cell bodies to guide the registration. Scale bars: 20 μm (a-d,fh), 80 μm (e).

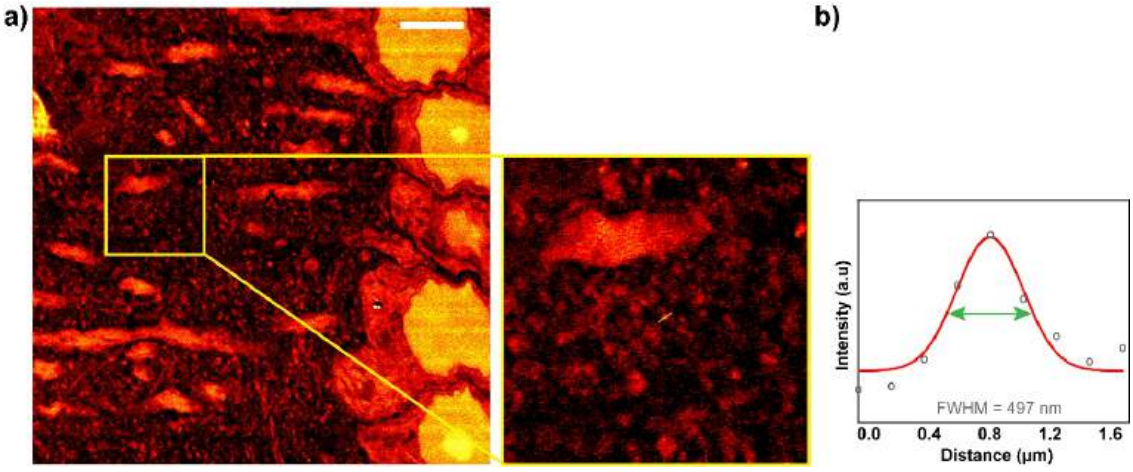

Supplementary Figure 11. Characterizations of fine dendritic structures by VISTA. (a) A representative VISTA image at the CA1 region of a mouse hippocampus sample with a zoomed in view of fine structural details in the yellow box. (b) The cross-section profile of a dendritic structure with a FWHM of 497 nm (corresponding to a lateral size of ~175 nm for the unexpanded sample). Scale bars: 20 μm.

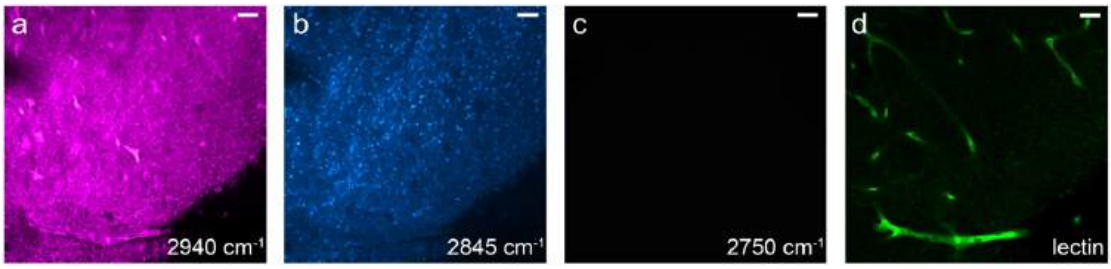

Supplementary Figure 12. Regular-resolution SRS imaging of a PFA-fixed but unprocessed mouse brain tissue. a-c, SRS imaging at 2940 cm-1 (a, CH3), 2845 cm-1 (b, CH2), and 2750 cm-1(c, off-resonance image). Cells, processes, and vessels could not be clearly identified from these SRS images. d, fluorescence image of lectin-stained blood vessel on the same tissue. Scale bars:20 μm.

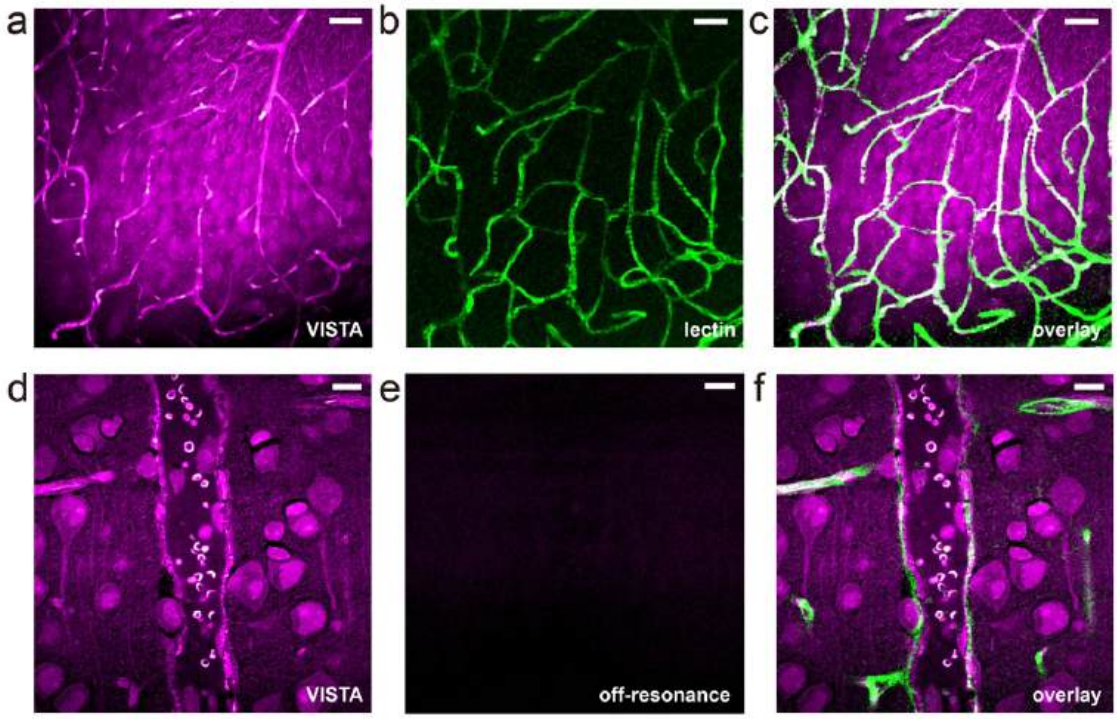

Supplementary Figure 13. Correlative VISTA images and the fluorescent images with lectin-stained vessels in mouse brain tissues. (a-c) The overlay image (c) for parallel images of VISTA (a, shown in Fig. 3a) and fluorescence from lectin-DyLight594 stained blood-vessels (b, shown in Fig. 3b). (d-e) VISTA image of a larger vessel (likely an artery) showing red blood cells (d, shown in Fig. 3c) and the corresponding off-resonance image at 2810 cm-1 confirms that signals in the VISTA image (including that of the red blood cells) are exclusively

SRS signals. (f) The overlay image for VISTA (Fig. 3c) and lectin-DyLight594 stained fluorescence (Fig. 3d). Scale bars: 40 μm. The length scale is in terms of distance after sample expansion.

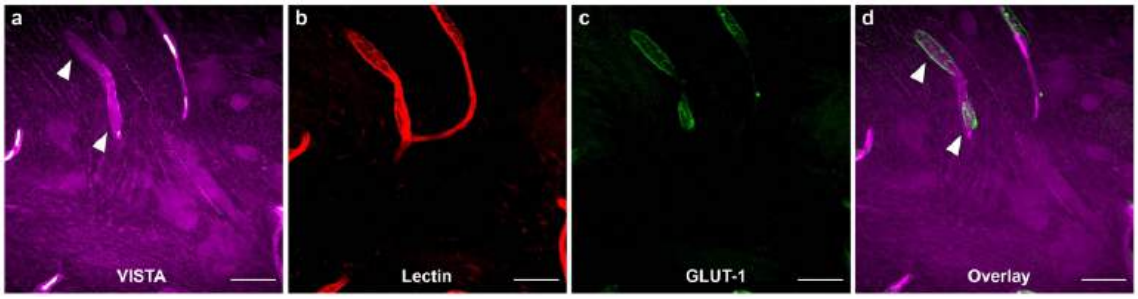

Supplementary Figure 14. Immuno-fluorescence reveals the cells in VISTA other than neuronal cells to be vascular endothelial cells. Elongated elliptical nuclei shown in VISTA (a, white arrow-headed, VISTA) co-localize (d, Overlay) with both fluorescent lectin-stained vessels (b, Lectin), and GLUT-1 (c, glucose transporter 1, brain endothelial cell marker) immunofluorescence-stained brain vascular endothelial cells. Images are shown as maximum Z projection. Scale bars: 50 μm. The length scale is in terms of distance after sample expansion.

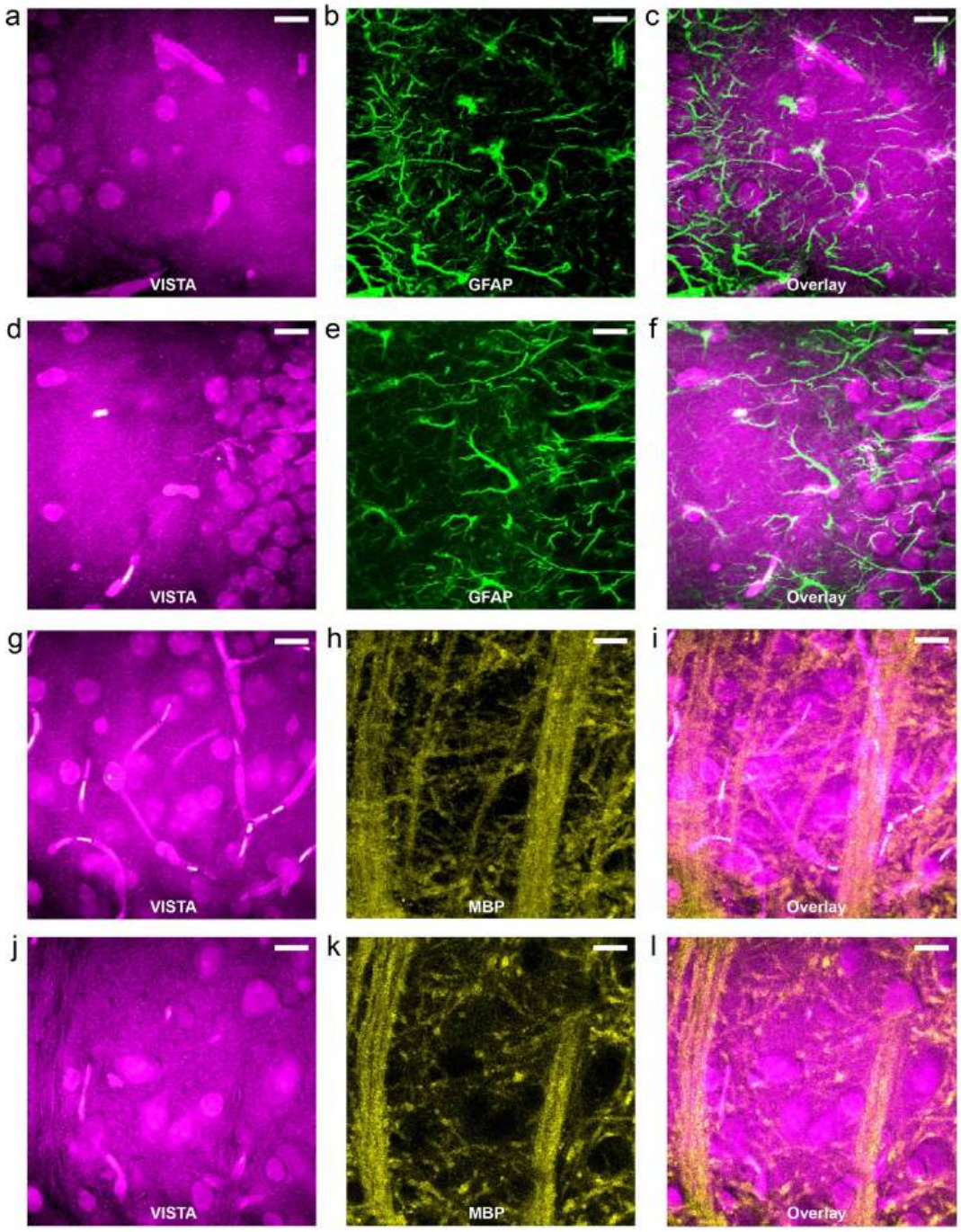

Supplementary Figure 15. Immunofluorescence confirms the absence of cytoplasmic structures from astrocytes and oligodendrocytes in VISTA. (a-f) Maximum z projection of VISTA image (a, d), immuno-stained fluorescence

image with GFAP (Glial Fibrillary Acidic Protein, the astrocyte cellular maker) antibodies (b, e) and the overlay (c, f). (g-i) maximum z projection of VISTA image (g), immuno-stained fluorescence image with MBP (Myelin Basic Protein, the myelin and oligodendrocyte cellular maker) antibodies (h) and the overlay (i). (j-l) single-slice VISTA image (j), immuno-stained fluorescence image with MBP antibodies (k) and the overlay (l). No correlation is identifiable between VISTA revealed cytoplasmic structures and GFAP or MBP stained cellular fluorescence images. Scale bars: 40 μm. The length scale is in terms of distance after sample expansion.

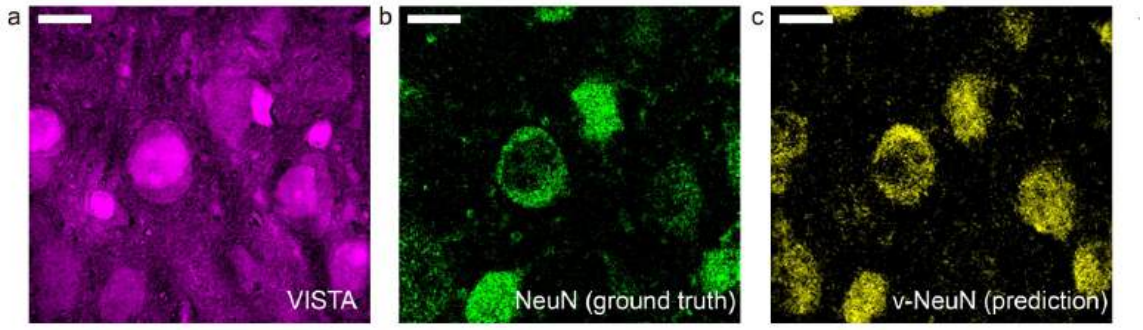

Supplementary Figure 16. Label-free VISTA prediction for neuronal cell bodies in brain tissues. (a-c) The input VISTA image (a), the ground truth fluorescence image of NeuN stained matured neurons (b) and the predicted VISTA-NeuN (v-NeuN) image of matured neurons from a (c). Scale bars: 40 μm. The length scale is in terms of distance after sample expansion.

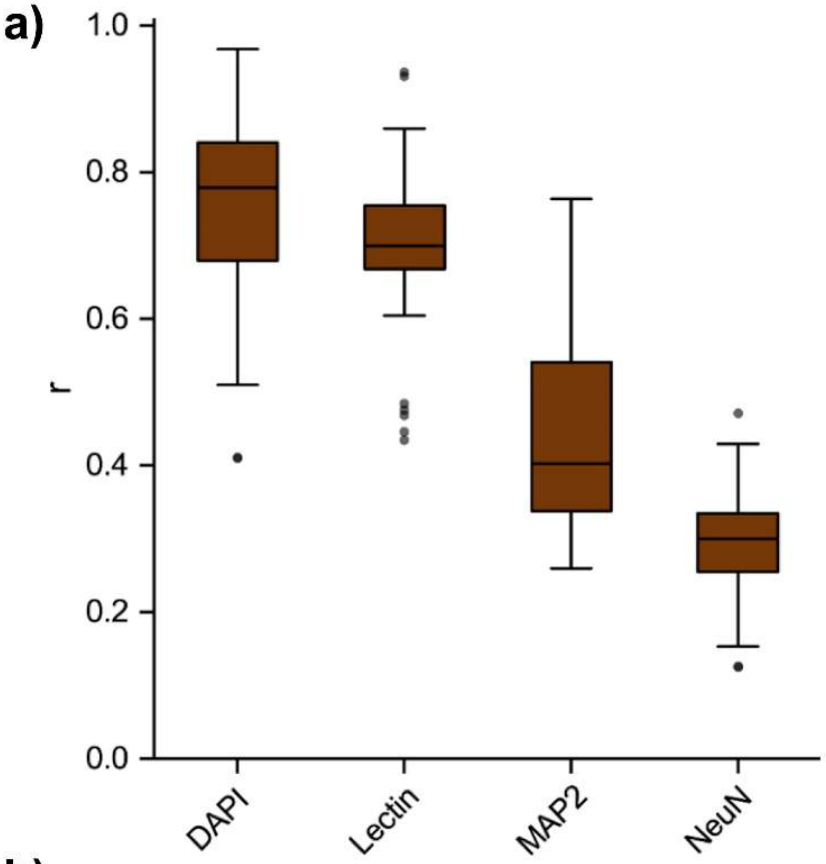
a)
1.0
0.8
0.6
0.4
0.2
0.0
r
DAPI
Lectin
MAP2
NeuN

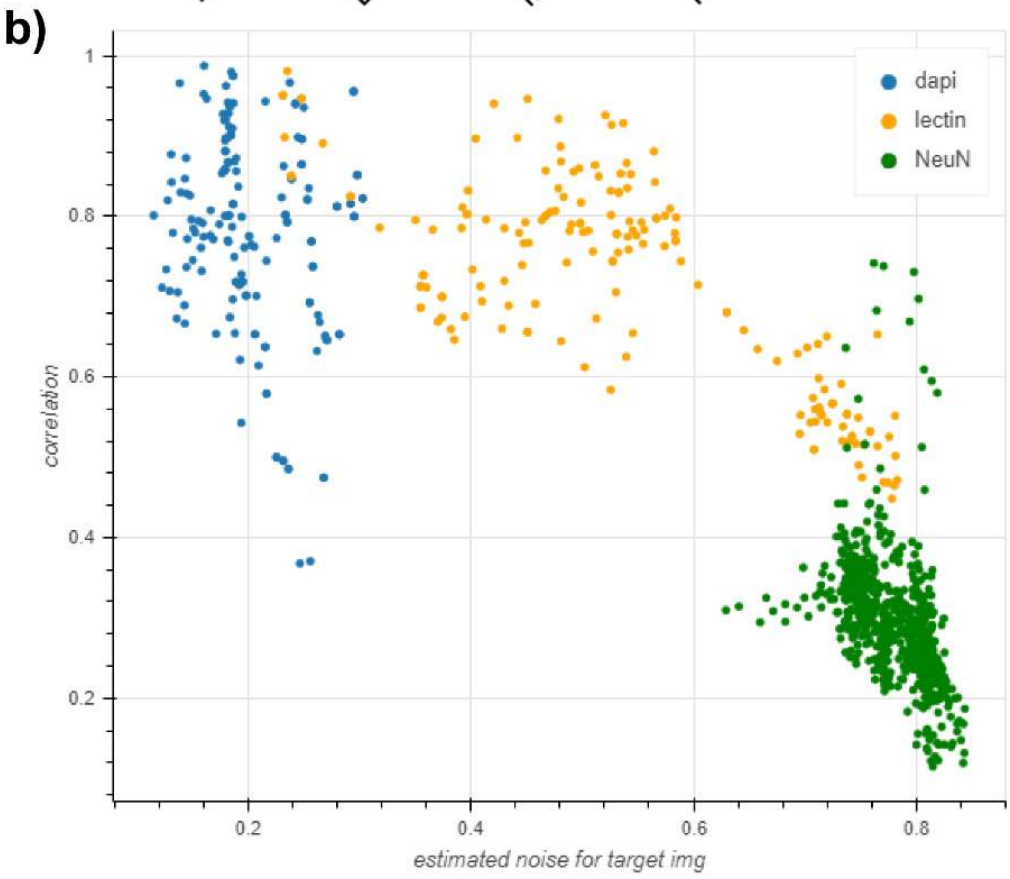
b)
dapi
lectin
NeuN
correlation
estimated noise for target img
0.2
0.4
0.6
0.8
1

Supplementary Figure 17. Model performance for the U-Net models, quantified by Pearson correlation coefficient (r). (a) Each point in the plot represents a target/predicted image pair. The boxes indicate the 25th, 50th, and 75th percentile of the Pearson's r for each model, with whiskers with maximum 1.5 interquartile range. Points within the box are not shown. DAPI, N=48; Lectin, N=37; MAP2, N=54; NeuN, N=130. (b) Correlation between the Pearson's r for the prediction results and the estimated standard deviation of the noise for ground-truth fluorescence images for DAPI, Lectin, and NeuN.

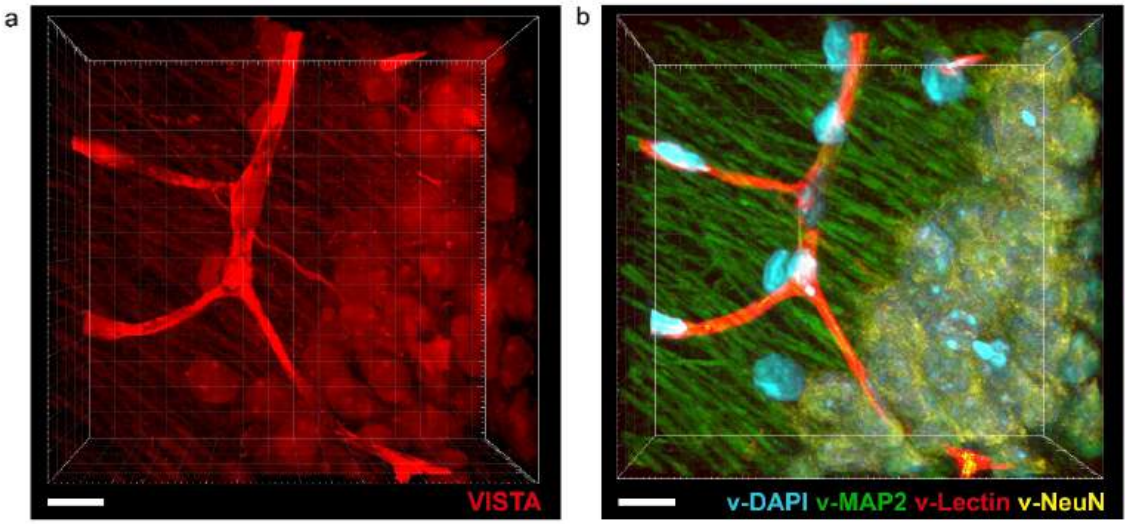

Supplementary Figure 18. Label-free VISTA prediction for multi-component imaging of mouse hippocampus. (a) The input VISTA image; (b) the predicted multicolor image with predicted v-DAPI (cyan), v-MAP2 (green), v-lectin (red), and v-NeuN (yellow) components, as shown in Fig. 4j. Scale bars: 40 μm. The length scale is in terms of distance after sample expansion.

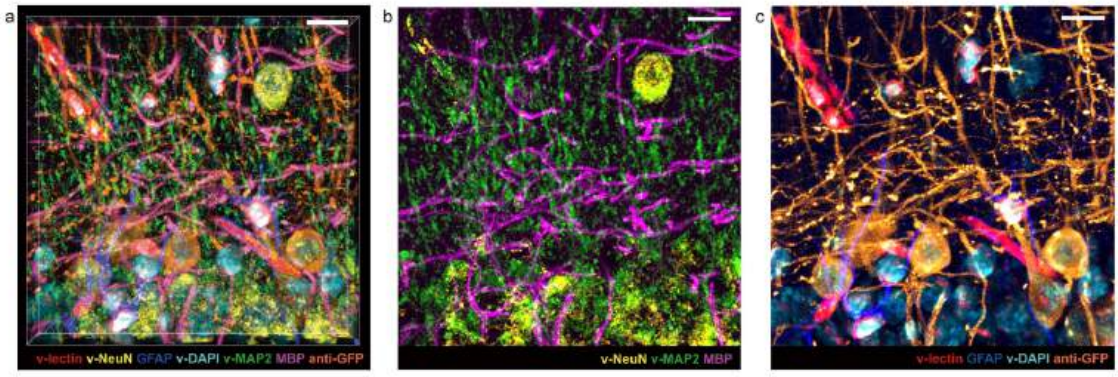

Supplementary Figure 19. 7-color multiplex imaging combining both label-free VISTA prediction and fluorescence imaging in hippocampus of Thy1-YFP mouse. (a) Volume 3D presentation of 7-color overlay image. (b-c) Maximum z projection view of 7 components in two sets of 3-color (b) and 4-color (c) overlay. VISTA components: v-NeuN (yellow), v-MAP2 (green), v-DAPI (cyan), v-lectin (red); immuno-fluorescence components: GFAP (blue), MBP (magenta), and anti-GFP (orange). Scale bars: 40 μm. The length scale is in terms of distance after sample expansion.

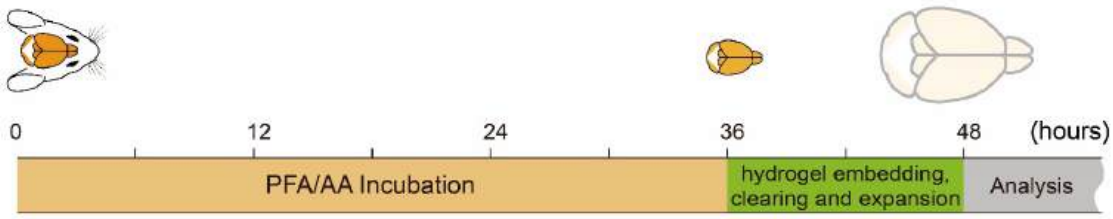

Supplementary Figure 20. Workflow of the sample processing steps for VISTA. Typical sample processing steps were completed with a 48-hour for mouse brain tissues before VISTA analysis. (PFA: paraformaldehyde; AA: acrylamide.)

1. 8 References

1. Huang, B., Bates, M. & Zhuang, X. Super-Resolution Fluorescence Microscopy. Annu. Rev. Biochem. 78, 993–1016 (2009).
2. Sahl, S. J., Hell, S. W. & Jakobs, S. Fluorescence nanoscopy in cell biology. Nature Reviews Molecular Cell Biology 18, 685–701 (2017).
3. Wassie, A. T., Zhao, Y. & Boyden, E. S. Expansion microscopy: principles and uses in biological research. Nature Methods 16, 33–41 (2019).
4. Chen, F., Tillberg, P. W. & Boyden, E. S. Expansion microscopy. Science 347, 543–548 (2015).
5. Tillberg, P. W. et al. Protein-retention expansion microscopy of cells and tissues labeled using standard fluorescent proteins and antibodies. Nature Biotechnology 34, 987–992 (2016).
6. Murray, E. et al. Simple, Scalable Proteomic Imaging for High-Dimensional Profiling of Intact Systems. Cell 163, 1500–1514 (2015).
7. Kim, S.-Y. et al. Stochastic electrotransport selectively enhances the transport of highly electromobile molecules. Proceedings of the National Academy of Sciences 112, E6274–E6283 (2015).
8. Shen, Y., Hu, F. & Min, W. Raman Imaging of Small Biomolecules. Annual Review of Biophysics 48, 347–369 (2019).
9. Cheng, J.-X. & Xie, X. S. Vibrational spectroscopic imaging of living systems: An emerging platform for biology and medicine. Science 350, (2015).

10. Saar, B. G. et al. Video-Rate Molecular Imaging in Vivo with Stimulated Raman Scattering. Science 330, 1368–1370 (2010).
11. Gasecka, A., Daradich, A., Dehez, H., Piché, M. & Côté, D. Resolution and contrast enhancement in coherent anti-Stokes Raman-scattering microscopy. Opt. Lett., OL 38, 4510–4513 (2013).
12. Silva, W. R., Graefe, C. T. & Frontiera, R. R. Toward Label-Free Super-Resolution Microscopy. ACS Photonics 3, 79–86 (2016).
13. Gong, L., Zheng, W., Ma, Y. & Huang, Z. Higher-order coherent anti-Stokes Raman scattering microscopy realizes label-free super-resolution vibrational imaging. Nature Photonics 14, 115–122 (2020).
14. Gong, L., Zheng, W., Ma, Y. & Huang, Z. Saturated Stimulated-Raman-Scattering Microscopy for Far-Field Superresolution Vibrational Imaging. Physical Review Applied 11, (2019).
15. Watanabe, K. et al. Structured line illumination Raman microscopy. Nature Communications 6, 10095 (2015).
16. Gradinaru, V., Treweek, J., Overton, K. & Deisseroth, K. Hydrogel-Tissue Chemistry: Principles and Applications. Annual Review of Biophysics 47, 355–376 (2018).
17. Ounkomol, C., Seshamani, S., Maleckar, M. M., Collman, F. & Johnson, G. R. Label-free prediction of three-dimensional fluorescence images from transmitted-light microscopy. Nature Methods 15, 917–920 (2018).
18. Shi, X. et al. Label-retention expansion microscopy. bioRxiv 687954 (2019) doi:10.1101/687954.

19. Puchtler, H. & Meloan, S. N. On the chemistry of formaldehyde fixation and its effects on immunohistochemical reactions. Histochemistry 82, 201–204 (1985).
20. Ku, T. et al. Multiplexed and scalable super-resolution imaging of three-dimensional protein localization in size-adjustable tissues. Nature Biotechnology 34, 973–981 (2016).
21. Gambarotto, D. et al. Imaging cellular ultrastructures using expansion microscopy (U-ExM). Nat Methods 16, 71–74 (2019).
22. Angueyra, J. M. & Kindt, K. S. Leveraging Zebrafish to Study Retinal Degenerations. Front. Cell Dev. Biol. 6, (2018).
23. Dvoriantchikova, G., Seemungal, R. J. & Ivanov, D. The epigenetic basis for the impaired ability of adult murine retinal pigment epithelium cells to regenerate retinal tissue. Scientific Reports 9, 3860 (2019).
24. Kandel, E. R. The Molecular Biology of Memory Storage: A Dialogue Between Genes and Synapses. Science 294, 1030–1038 (2001).
25. Liebmann, T. et al. Three-Dimensional Study of Alzheimer's Disease Hallmarks Using the iDISCO Clearing Method. Cell Reports 16, 1138–1152 (2016).
26. Wei, M. et al. Volumetric chemical imaging by clearing-enhanced stimulated Raman scattering microscopy. Proceedings of the National Academy of Sciences 116, 6608–6617 (2019).
27. Hama, H. et al. ScaleS: an optical clearing palette for biological imaging. Nature Neuroscience 18, 1518–1529 (2015).
28. Kirst, C. et al. Mapping the Fine-Scale Organization and Plasticity of the Brain Vasculature. Cell 180, 780-795.e25 (2020).

29. Helmstaedter, M. Cellular-resolution connectomics: challenges of dense neural circuit reconstruction. Nature Methods 10, 501–507 (2013).

30. Ueda, H. R. et al. Tissue clearing and its applications in neuroscience. Nature Reviews Neuroscience 21, 61–79 (2020).

31. Todorov, M. I. et al. Machine learning analysis of whole mouse brain vasculature. Nature Methods 17, 442–449 (2020).

32. Hollon, T. C. et al. Near real-time intraoperative brain tumor diagnosis using stimulated Raman histology and deep neural networks. Nature Medicine 26, 52–58 (2020).

33. Zhang, J., Zhao, J., Lin, H., Tan, Y. & Cheng, J.-X. High-Speed Chemical Imaging by Dense-Net Learning of Femtosecond Stimulated Raman Scattering. The Journal of Physical Chemistry Letters 11, 8573–8578 (2020).

34. Lin, H. et al. Fingerprint Spectroscopic SRS Imaging of Single Living Cells and Whole Brain by Ultrafast Tuning and Spatial-Spectral Learning. arXiv preprint arXiv:2003.02224. (2020).

35. Manifold, B., Thomas, E., Francis, A. T., Hill, A. H. & Fu, D. Denoising of stimulated Raman scattering microscopy images via deep learning. Biomed. Opt. Express, BOE 10, 3860–3874 (2019).

36. Falk, T. et al. U-Net: deep learning for cell counting, detection, and morphometry. Nature Methods 16, 67–70 (2019).

37. Bi, Y. et al. Near-resonance enhanced label-free stimulated Raman scattering microscopy with spatial resolution near 130 nm. Light: Science & Applications 7, (2018).

38. Sun, D. et al. Click-ExM enables expansion microscopy for all biomolecules. Nature Methods 1–7 (2020) doi:10.1038/s41592-020-01005-2.

Chapter 3

HIGH RESOLUTION IMAGING OF IN VIVO PROTEIN AGGREGATES

Lin, L. E., Miao, K., Qian, C., & Wei, L. (2021). High spatial-resolution imaging of label-free in vivo protein aggregates by VISTA. *Analyst*, *146*(13), 4135-4145. doi: 10.1039/D1AN00060H

3. 1 Summary

Amyloid aggregation, formed by aberrant proteins, is a pathological hallmark of neurodegenerative diseases, including Alzheimer's disease and Huntington's disease. High-resolution holistic mapping of the fine structures from these aggregates should facilitate our understanding of their pathological roles. Here, we achieved label-free high-resolution imaging of the polyQ and the amyloid-beta (Aβ) aggregates in cells and tissues utilizing a sample-expansion stimulated Raman strategy. We further focused on characterizing the Aβ plaques in 5XFAD mouse brain tissues. 3D volumetric imaging enabled visualization of the whole plaques, resolving both the fine protein filaments and the surrounding components. Coupling our expanded label-free Raman imaging with machine learning, we obtained specific segmentation of aggregate cores, peripheral filaments together with cell nuclei and blood vessels by pre-trained convolutional neural network models. Combined with 2-channel fluorescence imaging, we achieved a 6-color holistic view on the same sample. This ability for precise and multiplex high-

resolution imaging of the protein aggregates and their micro-environment without the requirement of labeling will open the way for new new biomedical applications.

3. 2 Introduction

Protein aggregation is one major pathological hallmark of neurodegenerative diseases.[1–3] For example, in Alzheimer's disease (AD), the amyloid plaques are made up of fibrillar aggregations containing misfolded Aβ peptides. There is, however, still much unknown about the mechanism of the structural formation and the neurotoxic effects of these aggregates in neurodegenerative diseases.[4–6] For example, it remains controversial whether the oligomers of the misfolded proteins are more toxic than the densely-packed aggregates.[7–9] On the other hand, aggregates have also been shown to induce cellular malfunctions by physically disrupting functional proteins and organelles.[10] It is hence essential to obtain high-resolution holistic views of the protein aggregates together with their micro-environment to offer new structural-functional insights and to shed light on pathologic understanding in neurodegeneration.

Extensive efforts have been devised to characterize the nanoscale structural details and to understand the functional implications of these protein aggregations.[11–17] For instance, with the combination of array tomography and stimulated emission depletion microscopy (AT-STED), ~0.1 μm resolution imaging on Aβ plaques has been shown.[12] In addition, single-molecule switching nanoscopy (SMSN) has demonstrated imaging of the fine features of the fibrillar arrangement in 30 μm thick brain sections.[11] However,

super-resolution fluorescence imaging techniques (i.e. STORM, PALM, and STED) are still limited to a rather shallow penetration depth of within 100 μm and offer low multiplexity.[14,18] This limits investigations of the native microenvironment around the plaques, which plays an irreplaceable role in AD progression.[19–23]

Recent reports have shown that AD pathology is also accompanied by neurofibrillary tangles and cerebral vasculature alterations in addition to the presence of Aβ plaques.[19–21] Moreover, reactive astrocytes and activated microglia are implicated in influencing the neuronal functions in AD.[22,23] Tissue clearing techniques, such as iDISCO, have been deployed for fluorescence imaging of the aggregates in deep tissues and to investigate the microenvironment of the plaques.[24–26] They indeed revealed remarkably complex morphology of the plaques and intricate interactions between the aggregates and their immediate environment, including blood vessels, microglia, and axons.[24–26] However, tissue labeling is generally prolonged and inhomogeneous, due to the slow penetration and inefficient targeting of the fluorescent probes.[27] In particular, the diffusion of large antibodies into the tissues often poses a rate-limiting step for the experiments.[27] Multiple rounds of screening are also often required to find an effective antibody with satisfying targeting efficiency and specificity.[24] Congo red, a smaller organic dye, presents better penetration, but has been shown to only stain positively for the cores of the plaques and could not reveal more detailed encompassing fibrillar structures.[28–30] It therefore remains highly demanded to have a novel imaging strategy that brings super-resolution imaging of the aggregates and

their surroundings into deep tissues while addressing the issues arising from required fluorophore labeling inside tissues. Such high-resolution and high-throughput volumetric imaging should help offer a holistic view of various plaque morphology in their native environment together with their spatial interactions with the surrounding components.

Toward this goal, Raman spectro-microscopy provides specific chemical information in a label-free manner by probing chemical vibrations directly from the biomolecules.[31–34] Prominently, hyperspectral stimulated Raman scattering (hSRS) imaging has been applied to mapping the Aβ plaques in fresh tissues with high sensitivity and speed.[35] Utilizing the Amide I vibrational band, native and misfolded proteins were imaged and delineated. The spatial resolution of conventional stimulated Raman scattering (SRS) imaging is, nonetheless, limited to ~0.4 μm, which is much coarser than the size of the *plaque* filaments and fibrils, which were suggested to be about 0.1 μm in diameter, in brain tissues.[11]

Recently, we developed a strategy for label-free super-resolved SRS imaging of endogenous protein-abundant structures in cells and tissues, by utilizing the Raman-compatible sample-polymer hybridization chemistry with subsequent isotropic sample expansion.[36] This new strategy, termed vibrational imaging of swelled tissues and analysis (VISTA), obtained an effective imaging resolution within 100 nm and offered a volumetric 3D view deep inside tissues.[36] Although sample expansion has gained rapid popularity for biological investigations,[37] so far no expansion imaging on protein aggregates has been reported. In this manuscript, we establish a VISTA-

based pipeline for high-resolution, label-free, and specific interrogations of Aβ plaques, filaments with the nearby cell nuclei, and blood vessels throughout mouse tissues (Fig. 1). First, we established that VISTA could preserve the general structure of the protein aggregates and allow isotropic expansion of these dense structures for nanoscale morphological investigations. Second, with the integration of a pre-trained U-Net convolutional neural network (CNN) from correlative VISTA and fluorescence imaging, high-resolution segmentation was also obtained for target-specific expanded imaging. Third, with tandem fluorescence microscopy, we achieved 6-color multiplex imaging for holistic visualization of the aggregate nano-morphology and their complex tissue surroundings of blood vessels, nuclei, myelin, astrocytes, and oligodendrocytes.

3. 3 Results

Characterizations of aggregate capture and expansion

We first characterized whether VISTA could be applied to imaging protein aggregates. Although we have recently successfully demonstrated the strategy of VISTA on visualizing protein-abundant structures in sample-hydrogel hybridized and expanded cells and tissues by SRS imaging at 2940 cm^{-1}, there are two major concerns toward imaging of the aggregates that await validations: first, whether acrylamide monomer could efficiently penetrate into the dense aggregate structure (Fig. 1, step 1, incubation) to effectively capture and hybridize the proteins inside aggregates to the

polymer gel network (Fig. 1, step 3, gelation); second, whether the captured protein aggregates after the denaturing step (Fig. 1, step 4) could be expanded isotropically to achieve the desired resolution with well-preserved local structures (Fig. 1, step 5, expansion).

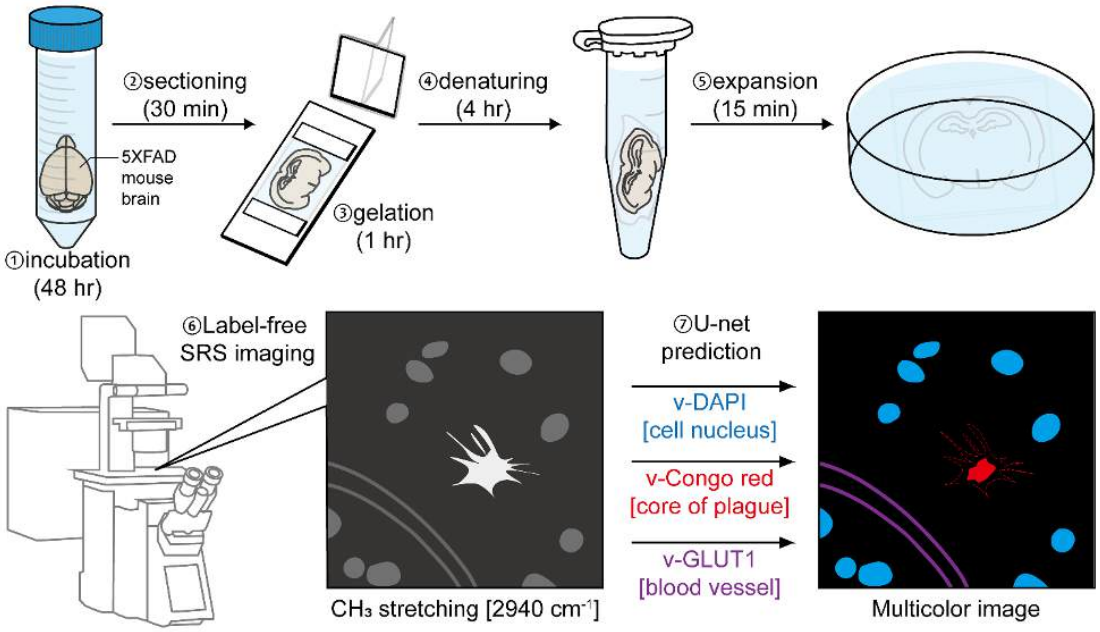

Fig. 1 Schematic illustration of proposed experimental workflow for high-resolution volumetric VISTA imaging of the amyloid-beta (Aβ) aggregates. The brain tissues from 5XFAD mice are hybridized with the polymer gel and expanded following the VISTA protocol of incubation, gelation, denaturing, and expansion. The samples are subsequently examined by SRS imaging at 2940 cm-1 (i.e. VISTA imaging). The VISTA images are then segmented by the pre-trained U-Net models with correlative VISTA images and fluorescence stains to predict different and

distinct features, including cores of plaques (v-Congo red), cell nuclei (v-DAPI), and blood vessels (v-GLUT1).

To establish VISTA on protein aggregates, we first tested whether the proteins inside the aggregates could be largely hybridized and retained onto the hydrogel network. We adopted two well-utilized model protein aggregate systems: the polyQ aggregates from the Huntington's disease in HeLa cells (Fig. 2A-D) and the Aβ plaques from the AD in brain tissues from 5XFAD transgenic mice (Fig. 2E-H), which develop severe amyloid pathology.[38] We started on the cellular level, for which we transfected Hela cells with an mHtt-97Q-GFP plasmid to examine the sample-processing and expansion of the polyQ aggregates. Before sample treatment, fluorescence imaging of GFP confirmed the aggregation formation (Fig. 2A). Parallel SRS imaging at the 2940 cm^{-1} showed a clear contrast from the corresponding protein-rich aggregates (Fig. 2B). After sample treatment and expansion, the alexa647-anti-GFP antibody was used to capture the expanded polyQ aggregates (Fig. 2C) since GFP fluorescence is quenched during the protein denaturing procedure (Fig. 1, step 4). In parallel, VISTA imaging on the same field of view showed a clear contrast of both large and small aggregates (Fig. 2D, the representative ones are indicated by an arrow and an arrowhead, respectively), indicating an effective hybridization between the aggregates and the hydrogel. We note that the lower fluorescence signal in the large and much more dense aggregates (Fig. 2C, arrowed) is likely due to the decreased labeling efficiency from limited penetration of the large antibodies into the aggregates.

We also note that the smaller bright spots in Fig. 2B (arrow indicated) are lipid droplets, which are not retained during the expansion process.

It is clear that the small fibril structures encompassing the aggregates could now be resolved after sample expansion, confirming the effectiveness of resolution increase in VISTA (Fig. 2D, zoomed-in insets of the green and cyan dash boxes). Interestingly, hollow-like structures were also observed in the large aggregate shown in Fig. 2D with adjusted image contrast (Fig. S2), indicating a lower protein concentration at the center of the large aggregates. We have also observed similar hollow structures in a number of unexpanded polyQ aggregates in live cells, but not with such clear contrast. Similarly, with the aid of correlative fluorescence imaging from Congo red staining (Fig. 2E, before treatment; Fig. 2G, after expansion), we established high specificity and sensitivity of VISTA imaging of the expanded Aβ plaques (Fig. 2F, SRS imaging at 2940 cm^{-1} before sample treatment; Fig. 2H, VISTA imaging after expansion). Both aggregation model systems confirmed that the aggregates could be clearly retained and expanded for sensitive visualization by VISTA.

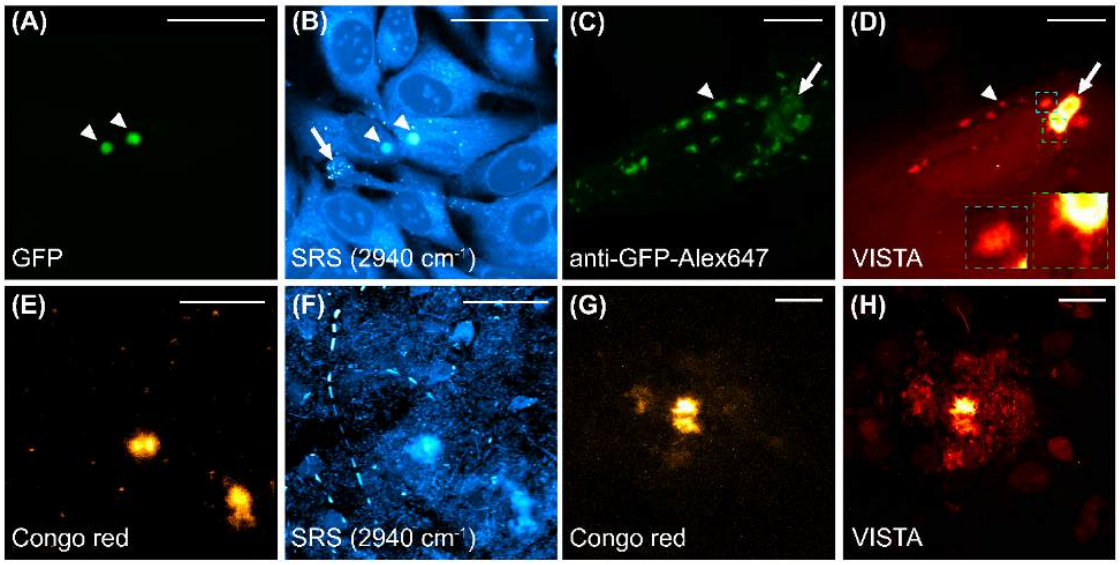

Fig. 2 SRS imaging at 2940 cm-1 for polyQ aggregates formed by the mHtt-97Q-GFP proteins (A-D) and Aβ plaques **(E-H) with correlative fluorescence imaging of targeted labels before and after expansion.** (A-B) Correlative fluorescence imaging of GFP (A) and the SRS imaging at 2940 cm-1 of unprocessed live HeLa cells formed with polyQ aggregates (arrowheaded) after transfected with the mHtt-97Q-GFP plasmid. PolyQ aggregates are indicated by arrowheads and representative small lipids droplets are indicated by an arrow. (B) at the same field of view. (C-D) Correlative fluorescence imaging of Alexa647-anti-GFP antibody labeled polyQ aggregates (C) and SRS imaging at 2940 cm-1 (D, VISTA) on expanded HeLa cells. The arrowhead and arrow indicate a representative small and a large polyQ aggregate, respectively. Two zoomed-in views in the colored dash boxes (D, insets, green, and cyan dash boxes designate the views from a large and a small aggregate respectively) show fine filaments at the outer shell of the aggregates. (E-F) Correlative fluorescence imaging

of Congo red labeled Aβ aggregates (E) and the SRS imaging at 2940 cm-1 (F) of fixed and unprocessed 5XFAD mouse tissues at the same field of view. (G-H) Correlative fluorescence imaging of Congo red labeled Aβ aggregates (G) and the SRS imaging at 2940 cm-1 (H, VISTA) of processed and expanded 5XFAD mouse tissues. Merged images of correlative fluorescence and SRS sets are shown in Fig. S1. scale bars: 40 μm.

Since we aim to characterize the fine morphology of the Aβ plaques, we next focused on Aβ aggregates in 5XFAD mouse tissues to analyze the expansion ratios and whether potential distortion might be introduced into the dense aggregates during the expansion. We tracked the protein aggregates in the tissue samples during the sample processing and expansion. We first performed SRS imaging comparison for the same tissue samples before and after gelation (Fig. 3A, before; Fig. 3B, after). It is obvious that gelation did not cause any morphological change of the aggregates. In addition, we observed an enhancement in contrast due to the loss of signals in the vicinity of the aggregates after gelation (Fig. 3B). This should be due to the deprivation of previously reported surrounding lipid contents,[35,39] since the hybridization chemistry here only retained proteins. The removal of the lipids was also confirmed by a loss of lipid features in the hSRS spectra from the aggregates and their surrounding areas (Fig. S3A).

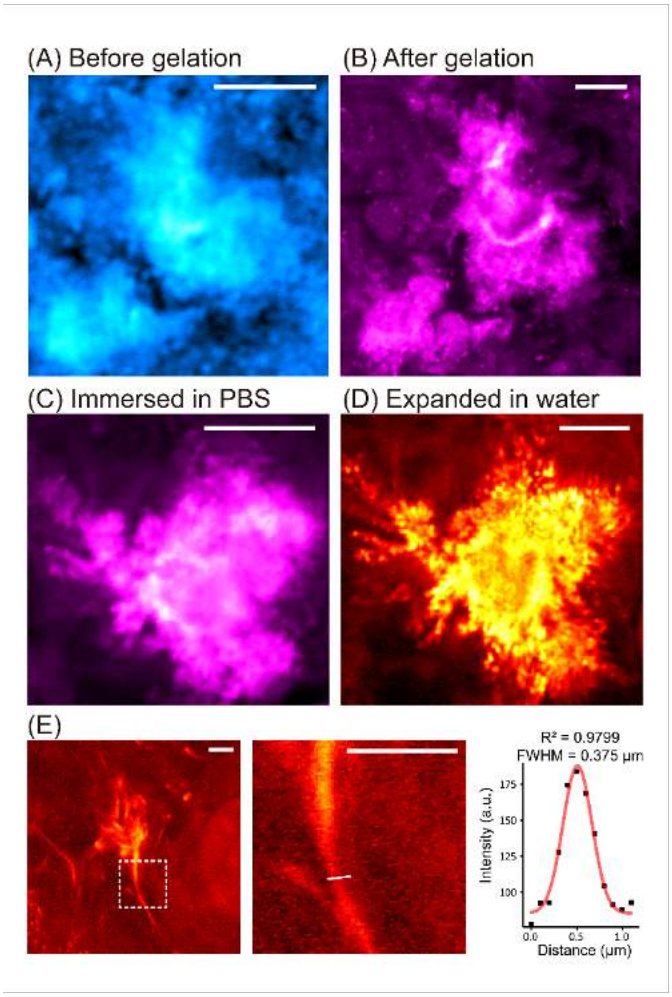

Fig. 3 Characterization of Aβ plaque expansion. (A-B) SRS images (at 2940 cm-1) for the same plaques before (A) and after (B) gelation. No obvious changes of location and morphology are observed. (C-D) SRS images (at 2940 cm-1) for the same plaques after gelation and immersed in PBS (C) versus in water (D). No distortion is shown during expansion in water with much-enhanced resolution. (E) The intensity profile of a fibril structure (boxed, the zoomed-in view shown on the right, the white line indicates the cross section for intensity fitting) in the expanded Aβ plaques imaged by VISTA is fitted by a gaussian distribution with a FWHM of 375 nm. Scale bars: 10 μm in (A)-(D), 5 μm in (E).

We next compared SRS images from the same aggregate immersed in PBS (with only a slight expansion, Fig. 3C) and in water (expected with full expansion, i.e. VISTA, Fig. 3D). Such detailed comparisons from the same plaques designate that the expansion is isotropic in water and is effective in resolution enhancement since all the fibrillar structures that were blurred in regular resolution SRS imaging (Fig. 3A-C) became clear and resolvable in VISTA imaging (Fig. 3D). Images from the same aggregate-containing tissue before gelation and after water-expansion were also captured to confirm the isotropic expansion and the loss of lipids (Fig. S3B-D). The similarity of the contour comparison for tissues before and after expansion (Fig. 2C-D and Fig. S3B-D) showed a more than 90% similarity, confirming the minimum expansion distortion. We calculated the average expansion ratio to be about 3.4 times from the plaques, which is consistent with previous reports of ours and others on brain tissues.[36,40] This indicates our effective resolution of label-free VISTA imaging could reach about 95 nm, highly suited to investigate these fibrils with reported width around 100 nm.[11] Indeed, our analysis confirmed that VISTA could capture Aβ fibrils with neck width around 110 nm (Fig. 3E, obtained by dividing the fitted full width at half maximum (FWHM), 375nm, by the average expansion ratio, 3.4).

High-resolution Volumetric VISTA imaging of the protein aggregates

Confirmed that VISTA is effective for high-resolution label-free imaging of the aggregate structures with retained fidelity, we then set out to visualize and identify various morphologies of the Aβ plaques in their native environment in 3D. We investigated the plaques formed in the hippocampus, which has been implicated to show early critical symptoms during the course

of AD.[21] For example, the hippocampal volumes were reported to reduce at an early stage of AD in human patients.[21] A large field-of-view mosaic VISTA imaging from the dentate gyrus easily captured the plaque distributions with their pronounced contrasts (Fig. 4A, plaques boxed with colored dash boxes). Zoomed-in views on the boxed regions are shown on the right with corresponding box colors (Fig. 4A). Despite the multi-component complexity in tissues, the protein aggregates showed a clear standout in the label-free image due to their higher local protein concentrations. In addition to aggregates, cell nuclei in the tissues were also distinctively captured by VISTA, which was confirmed by DAPI stain (Fig. S4A). It has been previously observed that the Aβ deposits are surrounded by a large number of microglia and astrocytes and could activate the prominent responses from these cells.[24,41,42] The ability to clearly visualize cell nuclei and aggregates at the same time without other signal interferences (i.e. lipids) could help us perform analysis of plaque-cell interactions.

Indeed, volumetric imaging of the hippocampal tissues could nicely provide 3D views of the plaques deep into the tissues without any sacrifice on the resolution (Fig. 4B, 700 μm depth after expansion). It is also clear that the large plaques are surrounded by a high number of cells (boxed), while the smaller ones do not present such obvious enrichment of cell nuclei in the vicinity (Fig. 4B). The image depth should be further increased to a few mm after the upgrade of the condenser to a long working distance objective.[25,36] Additionally, we found that blood vessels are also a clear standout in the VISTA images (Fig. 4B, arrow indicated), the identity of which was

confirmed by both lectin and anti-GLUT1 staining (Fig. S4B). Here, we showcased the capability of visualizing the intricate spatial relationship of the Aβ plaques and their surrounding components of cell nuclei and blood vessels. The change of blood flow, and hence the vascular alterations in morphology and diameters, are also an early sign of AD.[19,43] We envision that this ability to perform high-resolution high-throughput investigations between these three components inside tissues could largely facilitate our understandings of the influence on the structural integrity with the deposition of the Aβ plaques.

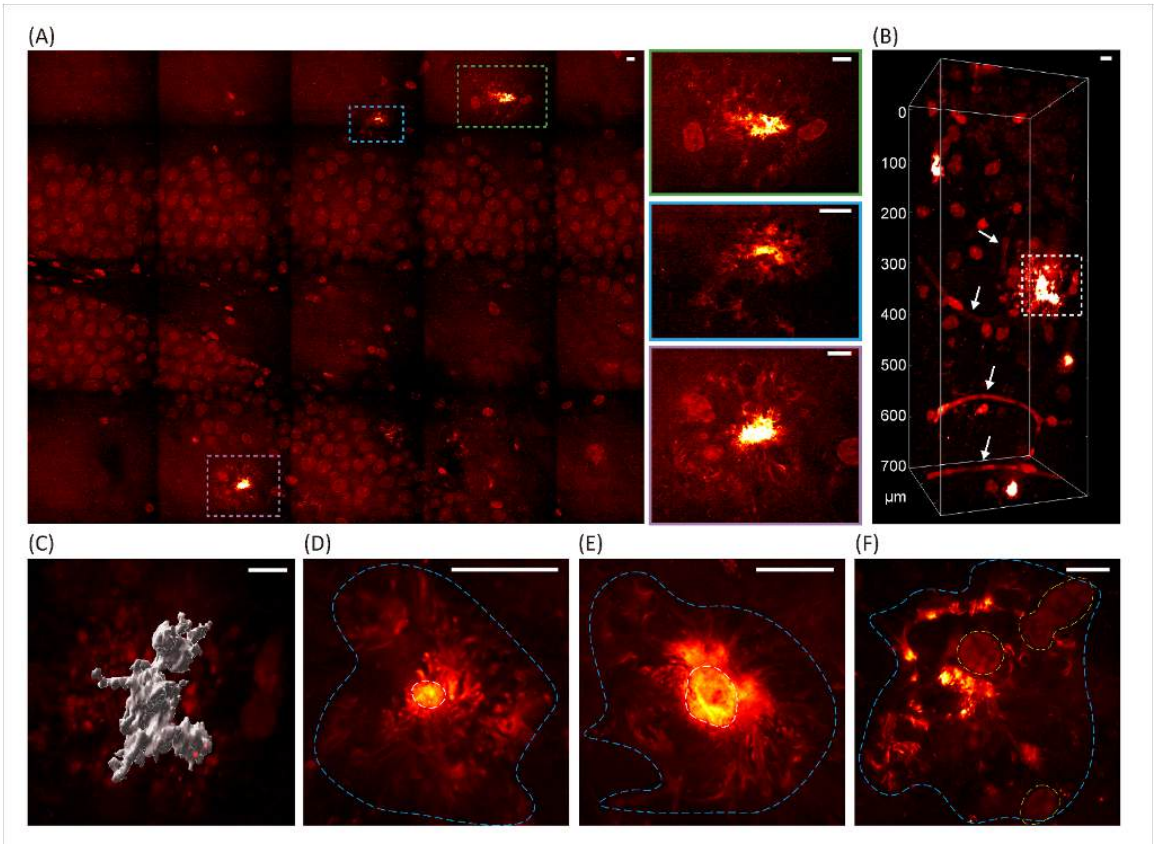

Fig. 4 VISTA mapping for the locations, morphologies, and the surroundings of the Aβ plaques **in the hippocampal tissues.** (A) A single-z mosaic VISTA mapping of an Aβ-plaque-containing hippocampal tissue section. Multiple observed plaques are highlighted in the colored dash

boxes and shown in the zoomed-in views on the right side. (B) Deep imaging (700 μm) of the hippocampal tissues captures volume views of the plaques and the surrounding matrix. The arrows indicate blood vessels. (C) Surface rendering of the plaque indicated by the dashed box in (B). (D-F) Representative Aβ plaques with different morphological details. The areas with protein aggregates are circled by cyan dashed lines, core areas are circled by white dashed lines, and cell nuclei are circled by yellow dashed lines. Scale bars: 20 μm.

To take a closer look at the plaque morphology, we generated the surface rendering of the aggregate boxed in Fig. 4B for more detailed visualization in 3D (Fig. 4C). Different layers of the same plaque could be also visualized by adjusting the rendering threshold (Fig. S5, the core of the plaque). Furthermore, we showed high-resolution label-free VISTA images for representative morphology of versatile plaques (Fig. 4D-F). While plaques with obvious core structures and diffusive fibrillar surroundings were most commonly observed (Fig. 4D), plaques with halo-like cores and ribbon-like surroundings were also captured by our VISTA imaging (Fig. 4E). Such observations agreed well with previous reports by super-resolution fluorescence imaging.[12] Moreover, we identified entirely diffusive plaques, which were Congo red-negative, with less well-defined cores together with their close proximity to cell nuclei (Fig. 4F). All these rich diffusive morphologies were absent in fluorescence images of Congo red stained plaques since it only stains the cores. We hence demonstrated that our label-

free VISTA method offers superior imaging performance for close to 100 nm resolution imaging of Aβ plaques together with their key interacting components (e.g. cells and vessels) in a complex biological matrix.

High-resolution U-Net segmentation of label-free VISTA images for multiplex imaging.

After identifying that our VISTA could allow clear imaging of aggregates, cell nuclei, and blood vessels with nice correlations to the corresponding post-expansion fluorescence stains and imaging (i.e. Congo red for the plaque cores (Fig. 2G-H), DAPI for cell nuclei (Fig. S4A), and lectin and GLUT1 antibody for the vessels (Fig. S4B)), we next investigated whether we could segment all these components into individual channels for specific and multiplex imaging. CNN has achieved tremendous success in computer vision problems.[44] The U-Net architecture has been shown to be highly successful in segmenting, denoising, and predicting biomedical images.[45–47]

We adopted the reported U-Net architecture[45] for modeling the features in our VISTA images by feeding in the corresponding fluorescence-VISTA image pairs (Fig. 5). The qualities and contrasts of the predicted images (Fig. 5C) from the input VISTA images (Fig. 5A) were comparable to that of the fluorescence ground-truth (Fig. 5B). The nice model performance was quantified by Pearson's correlation coefficient (Pearson's r) between the predicted images and the ground-truth images for the test sets (Fig. S6). We note that for calculating Pearson's r for v-GLUT1 and v-Congo red sets, we

set a threshold to ensure that the images we were comparing indeed contained signals because the random noise in the background could not be predicted by the U-Net. Since the v-Congo red image only predicted the plaque cores, we then performed subtraction of the predicted channels from the original VISTA images to visualize the peripheral plaque filaments.

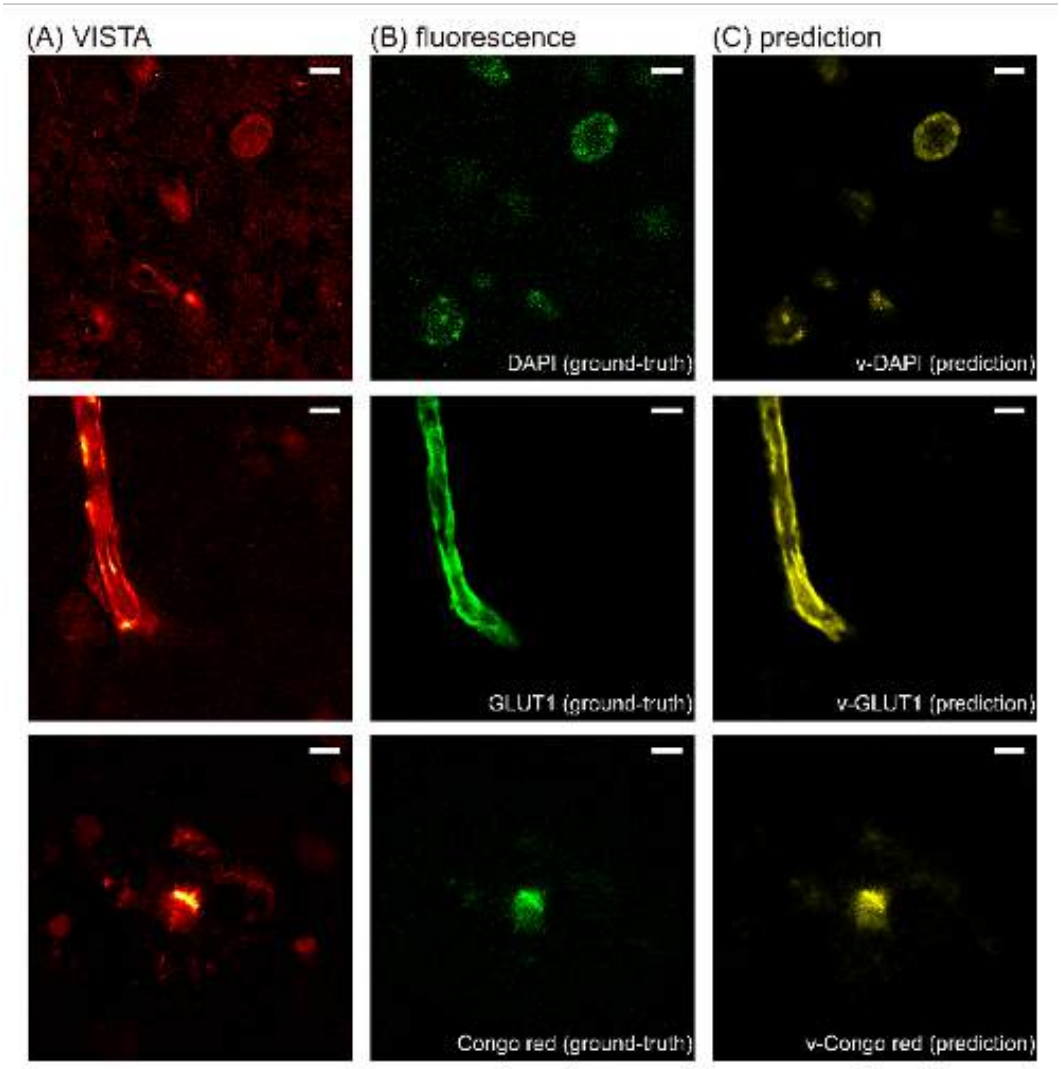

Fig. 5 VISTA images of the brain tissue with its corresponding ground-truth and prediction results. (A) Label-free VISTA images. (B) The

corresponding fluorescence ground-truth at the same field of view. (C) Prediction results by U-Net.

Through U-Net segmentation of VISTA images in 3D (Fig. 6A), a total of four-channel volumetric predicted imaging could be obtained (Fig. 6B) for plaque cores (green), plaque filaments (white), cell nuclei (cyan), and blood vessels (red). With additional channels of tandem fluorescence imaging of anti-MBP (myelin basic protein) antibody and anti-GFAP (glial fibrillary acidic protein) antibody staining, we obtained 6-color high-resolution imaging from the same Aβ-plaque-bearing hippocampal tissues (Fig. 6C) that could allow us to perform high-resolution interrogations for the distribution of Aβ plaque cores (green) and periphery filaments (white) together with their immediate environment of blood vessels (red), cell nuclei (cyan), astrocytes (yellow), and oligodendrocytes and myelin (magenta). For example, our further cross-channel analysis between the v-DAPI and GFAP channels revealed that a large portion (almost to a half) of the cells surrounding the Aβ plaques are astrocytes (Fig. S7&S8), which is consistent with the known effect of Aβ activated reactive astrocytes with astrocytic processes surrounding the plaque cores.[23,41] Such a multiplex imaging feat with minimum labeling requirements makes it extremely ideal for high-throughput and cost-effective large-scale biomedical investigations, for instance in human tissues, in the future.

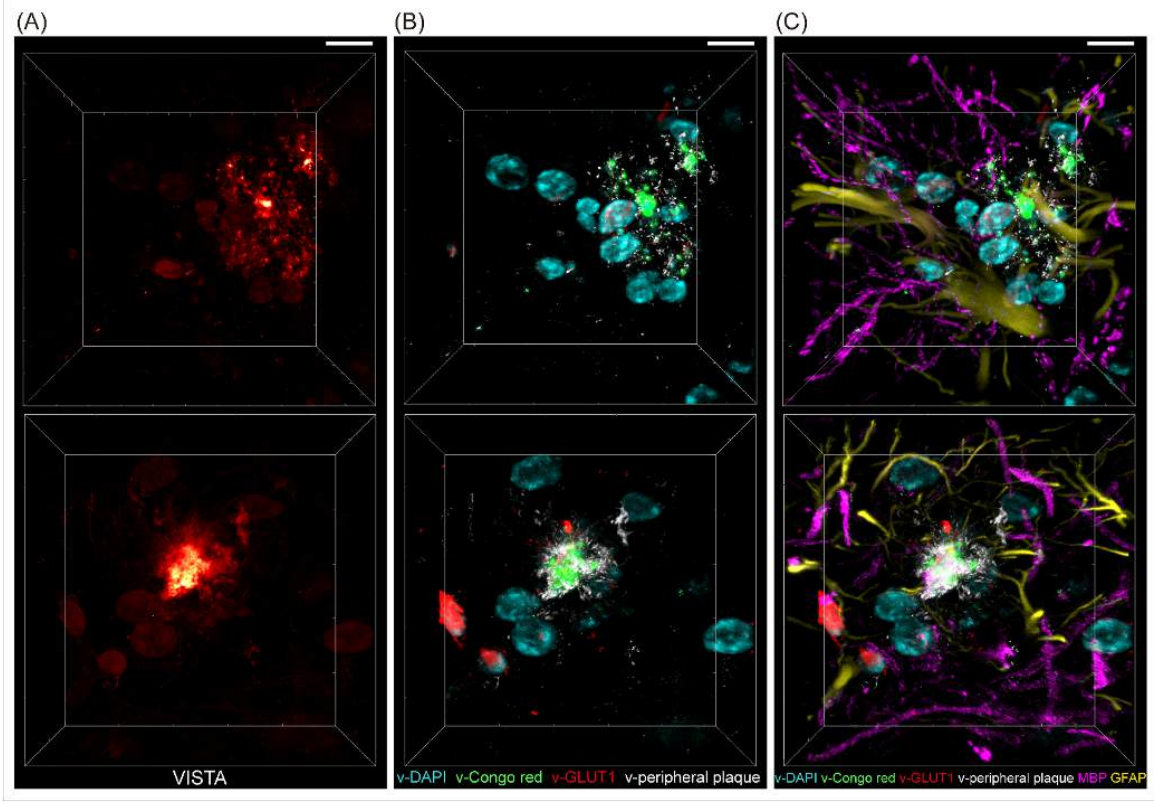

Fig. 6 3D multi-channel prediction of plaque-bearing hippocampus from two sets (top and bottom) of VISTA images. (A) VISTA images. (B) Four-channel overlay for v-DAPI (cyan, nuclei), v-Congo red (green, for plaque core), v-GLUT1 (red, blood vessels), and v-Peripheral plaque (white) by U-Net predicted high-resolution segmentation of the VISTA images in (A). (C) 6-color tandem fluorescence image of MBP (magenta, myelin basic protein) and GFAP (yellow, Glial fibrillary acidic protein) with 4-channel VISTA predictions. Scale bars: 30 μm.

In the context of the multiplex micro-environment imaging, we further observed plaques with different fine filament structures, which would not be detected by typical Congo red staining, nor readily resolved by regular-resolution SRS. We resolved aggregates with dotted filament structure and ribbon-like

structure, each surrounded by astrocytes of different morphologies (Fig. 6, top row (dotted-like, v-peripheral plaque) vs bottom row (ribbon-like). Zoomed-in views are shown in Fig. S9). Differences in astrocyte morphologies may indicate that they belong to varied subtypes, or designate that they have different levels of activation.[48–50] While further biological investigations are still required, our results here show that it is very likely that Aβ plaques with varied nano-scale morphological structures may play distinct pathological roles and our multiplex VISTA imaging could help to subtype these plaques based on their fine filament structures, which are absent from the typical Congo red labeling and imaging.

3. 4 Discussion

In this paper, we presented a label-free VISTA method for high-resolution vibrational imaging of protein aggregates, in particular for Aβ plaques in the AD. The Aβ plaques were easily identified and imaged. We further imaged plaque filaments with a resolution of approximately 100 nm and demonstrated large-scale mosaic and deep tissue volumetric imaging capabilities. Plaque cores, peripheral filaments, and the surrounding vasculature and cell nuclei were observed without the need of any labels and were further specifically segmented by a CNN-based U-Net method for 4-channel multiplex imaging. Finally, we demonstrated 6-channel imaging when tandem with fluorescence labels for further characterization of the proteins of interest, with observations for the correlation between varied fine plaque filament structures with distinct astrocyte morphologies. Our paper presents the first report for robust high-resolution imaging on the expanded aggregates with their interacting

native environment in tissues. We envision this expanded view of the protein aggregates could provide a new perspective for understanding the aggregate structures in the complex tissue environment and would further our insights on the roles of protein aggregates in neurodegenerative diseases.

3. 5 Methods and materials

Stimulated Raman scattering (SRS) microscopy.

The pump and Stokes beams were produced by a picoEmerald laser system (Applied Physics & Electronics.) The tunable pump beam (770 nm – 990 nm, spectral bandwidth ~ 7 cm^{-1}) and the Stokes beam (1031.2 nm, spectral bandwidth 10 cm^{-1}) are produced at an 80 MHz repetition rate. The Stokes beam was modulated at 20 MHz by a built-in electro-optic modulator (EOM). The pump and Stokes beams are spatially and temporally coupled inside the picoEmerald laser system and introduced into an FV3000 microscope (Olympus). The beams were then focused by a 25x water objective (XLPLN25XWMP, 1.05 numerical aperture (NA), Olympus) onto the sample for imaging. Transmitted light was collected by an oil immersion condenser lens (1.4 NA, Olympus) and the Stokes beam was blocked out by a bandpass filter (893/209 BrightLine, 25 mm, Semrock) while the pump beam was guided to a 10 mm×10 mm Si photodiode (S3590-09, Hamamatsu). To increase the saturation threshold and to reduce the response time, the photodiode was reverse biased by 64 V. The output current was pre-filtered by a 19.2-23.6-MHz bandpass filter (BBP-21.4+, Mini-Circuits) and

terminated with 50 Ω. The Raman loss signal of the pump beam was then demodulated by a lock-in amplifier (SR844, Stanford Research Systems or HF2LI, Zurich instrument) at the modulation frequency. The in-phase output is fed back into the Olympus IO interface box (FV30- ANALOG) of the microscope. Image acquisition speed is limited to 80 μs pixel dwell time with 30 μs time constant for the SR844 lock-in amplifier, and set to 20 μs pixel dwell time with 5 μs time constant for the HF2LI lock-in amplifier. The pump laser is tuned to 791.3 nm for imaging CH_3 vibrational mode at 2940 cm^{-1}. 16-bit grey scale images were acquired by Olympus Fluoview 3000 software. Volumetric images were acquired by a step size of 1 micron in the z-direction.

Reagents and materials.

Sodium acrylate (SA), acrylamide (AA), N,N′-methylenebisacrylamide (BIS, 2% in water), ammonium persulfate (APS), tetramethylethylenediamine (TEMED, Sigma-Aldrich), sodium dodecyl sulfate (SDS), Triton X-100, and deuterium oxide were obtained from Sigma-Aldrich. Tris(hydroxymethyl)aminomethane was obtained from Biosolve. Nuclease-free water and 4′,6-diamidino-2-phenylindole (DAPI) were purchased from Thermo Fisher. Paraformaldehyde (PFA, 16% in water) was purchased from Electron Microscopy Sciences.

Primary antibodies: anti-myelin basic protein in rat (ab7349) was purchased from Abcam; anti-glial fibrillary acidic protein in mouse (3670S) was purchased from Cell Signaling Technology, anti-glucose transporter 1 protein in rabbit (07-1401) was purchased from Sigma-Aldrich.

Secondary antibodies: goat anti-rat IgG, Alexa Fluor 568 (A-11077), goat anti-mouse IgG, Alexa Fluor 647 (A-21236); goat anti-rabbit IgG, Alexa Fluor 488 (A-11034) were purchased from Invitrogen.

Biological samples.

Cultured HeLa-CCL2 (ATCC) cells were cultured in DMEM (Gibco) with 10 percent fetal bovine serum (FBS, ThermoFisher) and 1 percent streptomycin penicillin (Sigma-Aldrich). Cells were seeded onto 14 mm glass-bottom microwell dishes (MatTek Corporation) or coverslips (12mm, #1.5, Fisher) for 24 h prior to transfection. Cells were first grown in regular DMEM complete medium until they reached 70-90% confluence. Transfection of 1-μg plasmids encoding mHtt-97Q-GFP was performed using Lipofectamine 3000 transfection reagent (ThermoFisher).

3. 6 Supplementary information

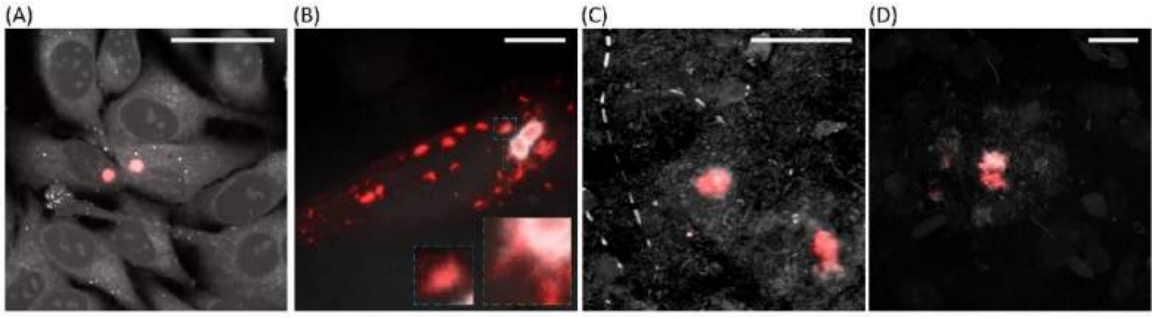

Fig. S1 Merged images of correlative fluorescence (red) and SRS (gray) from Fig. 2. (A) The merged image of Figure 2A (red) and 2B (gray). (B) The merged image of Figure 2C (red) and 2D (gray). (C) The merged image of Figure 2E (red)

and 2F (gray). (D) The merged image of Figure 2G (red) and 2H (gray). Scale bars: 40 μm.

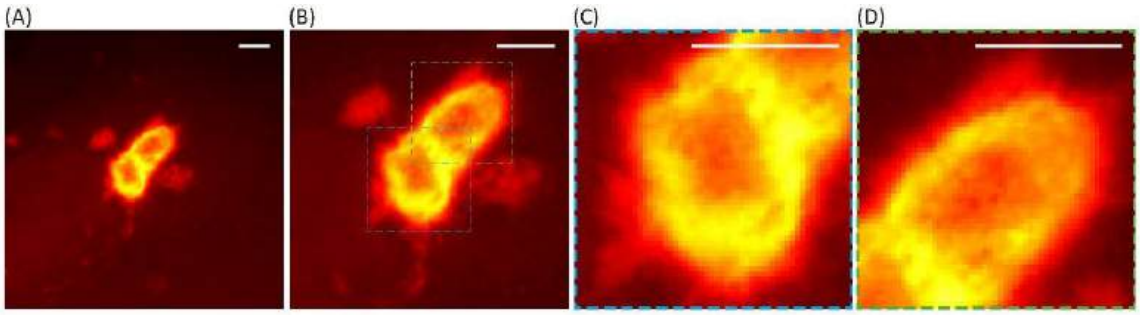

Fig. S2 Internal hollow structures for the PolyQ aggregates shown in Fig. 2B with adjusted image contrast. (A) VISTA image of the PolyQ aggregates in Fig. 2B with a larger intensity contrast range. (B) Zoomed in view from (A) for the same aggregate region. (C-D) Zoomed in views in (B) from the dashed boxes. Blue dashed box is shown in (C) and green dashed box is shown in (D). Scale bars: 10 μm.

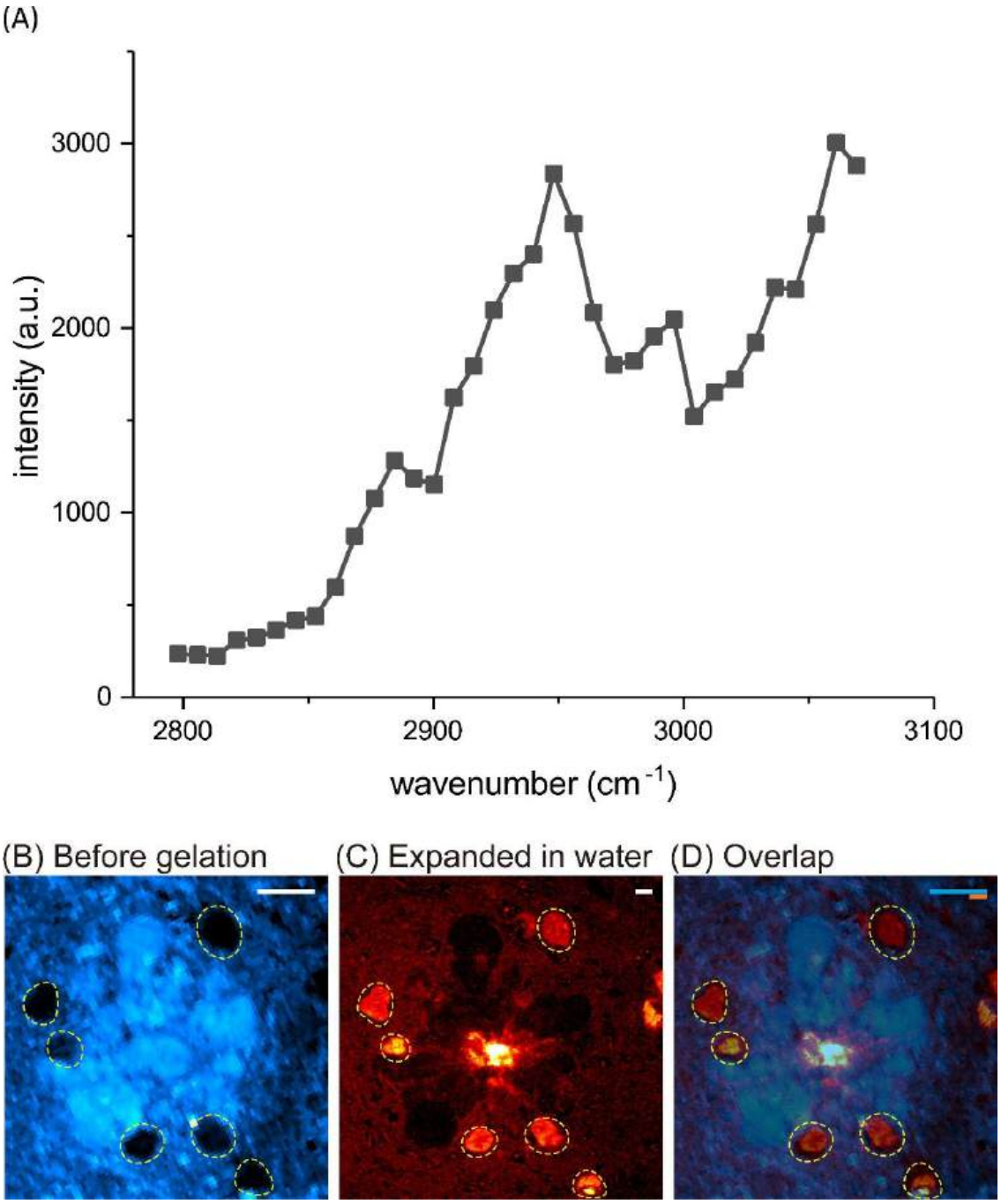

Fig S3. (A) The hSRS spectra of the expanded Aβ plaques in the CH region with a diminished spectral feature of lipid peaks around 2840 cm-1. (B-D) Registration of the same field of views before and after expansion from the same plaque-containing brain tissue samples. (B) Before gelation, (C) expanded in water,

showing the clear removal of lipids, and (D) overlap of B&C. The nuclei are circled by yellow dashed lines. Scale bars: 10μm.

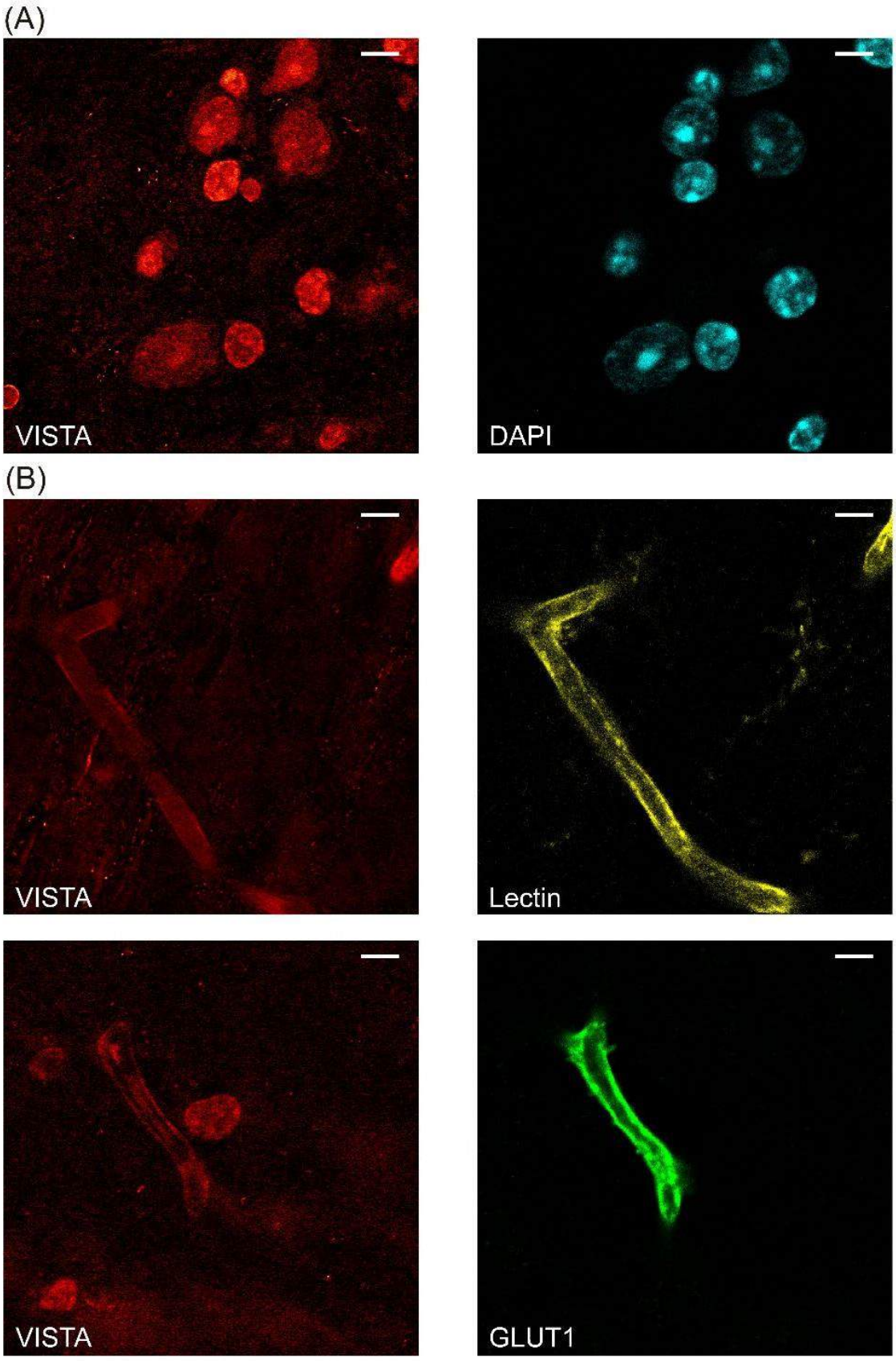
(A)
VISTA
DAPI
(B)
VISTA
Lectin
VISTA
GLUT1

Fig. S4 VISTA images (left column) with the corresponding fluorescence stains (right column) for (A) cell nuclei and (B) blood vessels (fluorescence confirmations for blood vessels include both the lectin stains and the anti-GLUT1 antibody labeling).

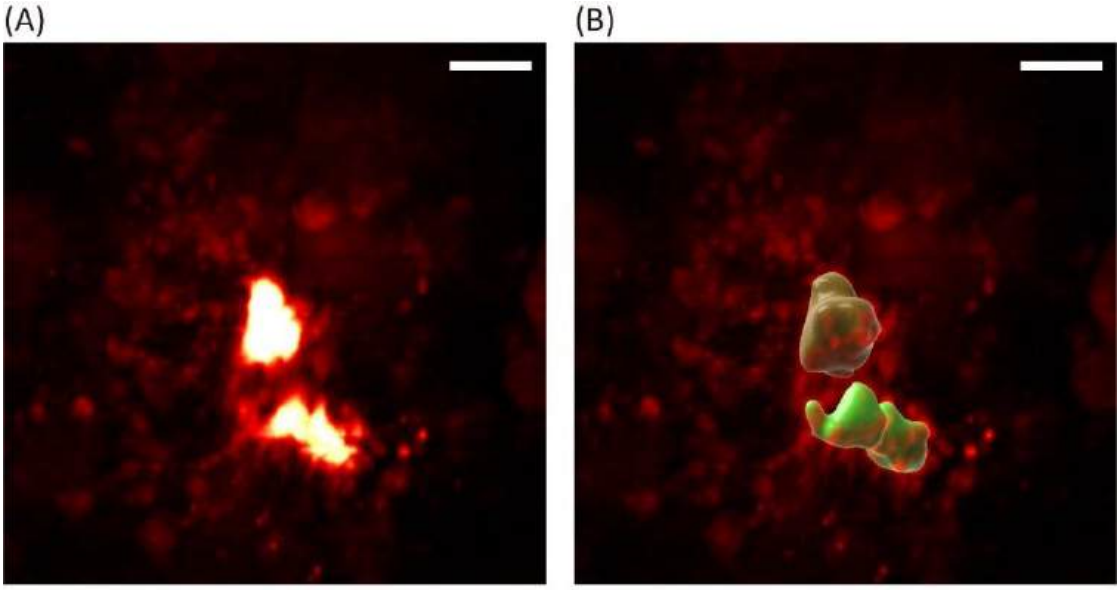

Fig. S5 (A) Intensity projection of the Aβ plaques in 3D. (B) Surface rendering for (A) showing the core of the aggregate. Scale bars: 20 μm.

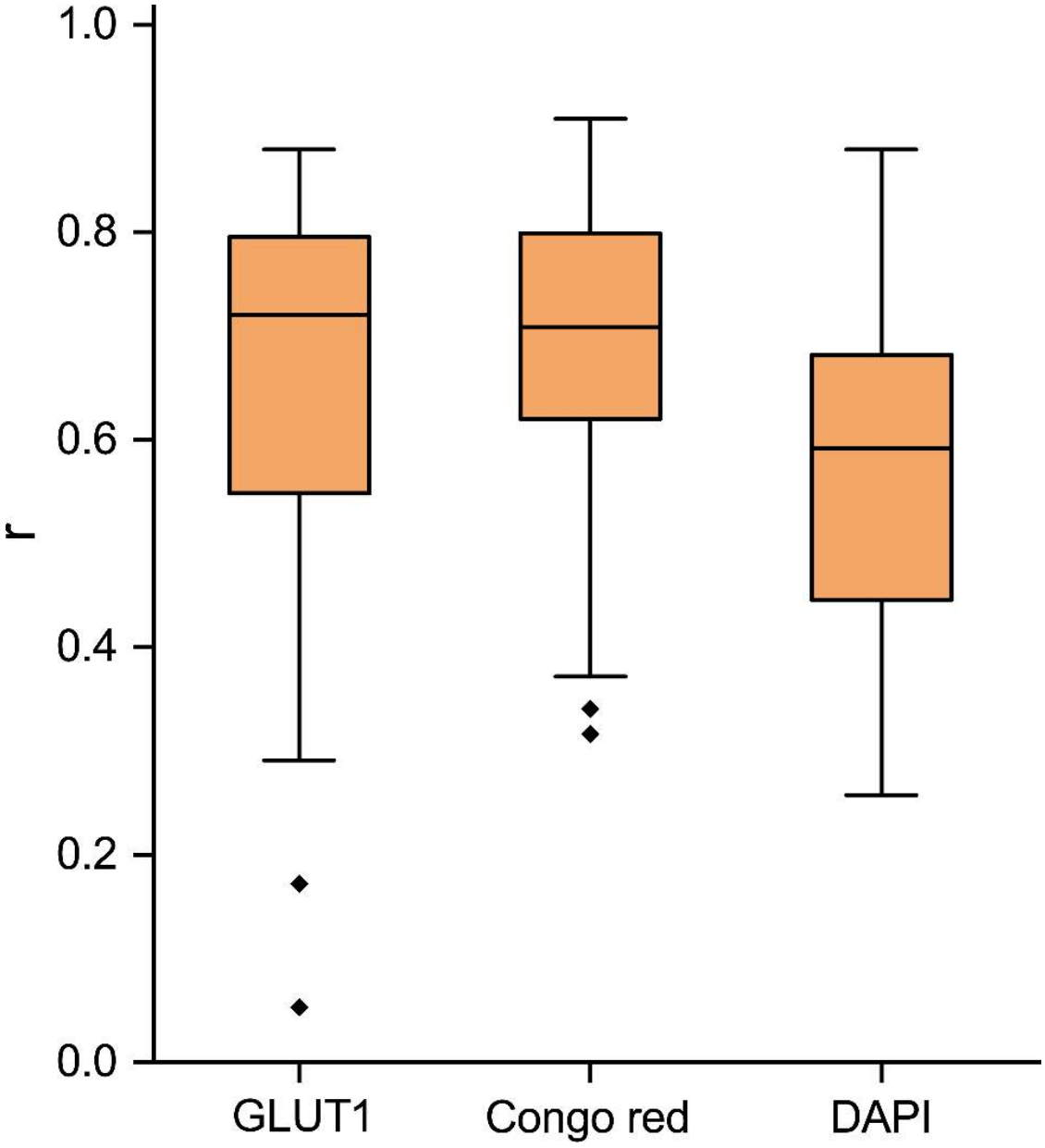

Fig. S6 Model performance of the U-Net models quantified by Pearson's correlation coefficient(r). The boxes indicate the 25th, 50th, and 75th percentile of the Pearson's r for each model, with whiskers indicating 1.5 interquartile range. Glut1, N=47; Congo red, N=25; DAPI, N=138.

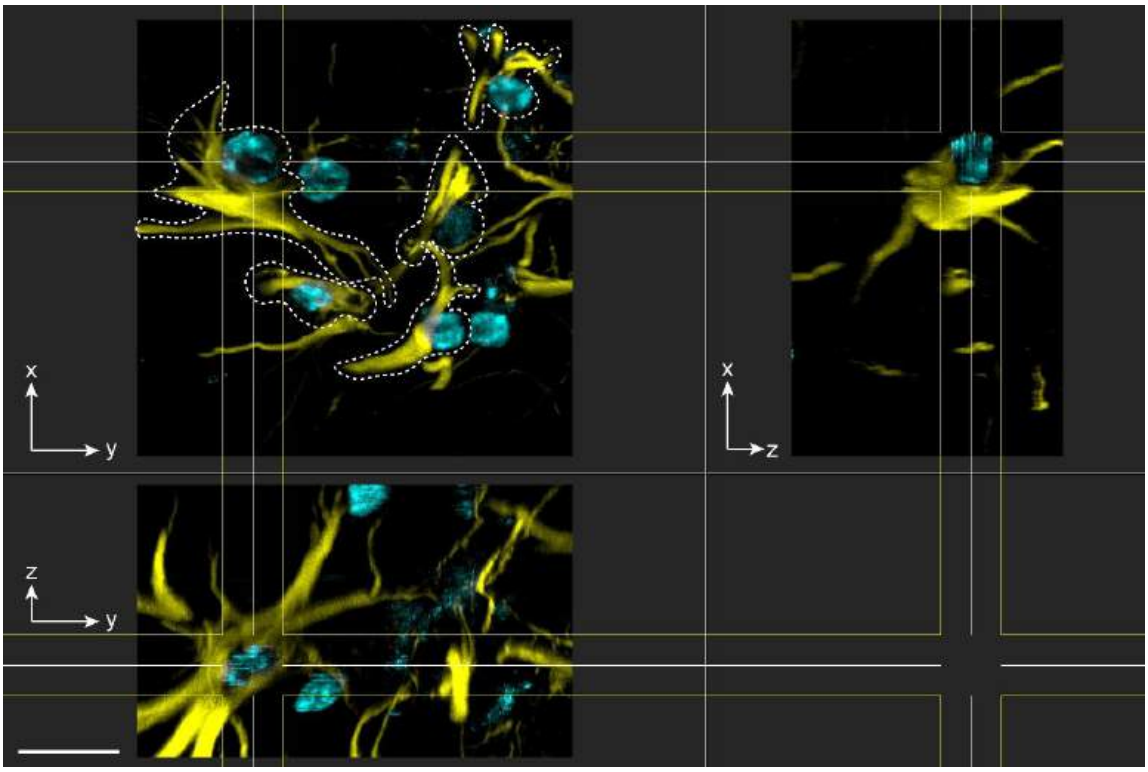

Fig. S7 Maximum intensity projection of predicted DAPI (v-DAPI, cyan) and fluorescence-labeled GFAP (yellow) for the cell set shown in the first row of Fig. 6. The cells circled by dashed lines were identified as astrocytes based on the GFAP staining and the v-DAPI pattern.

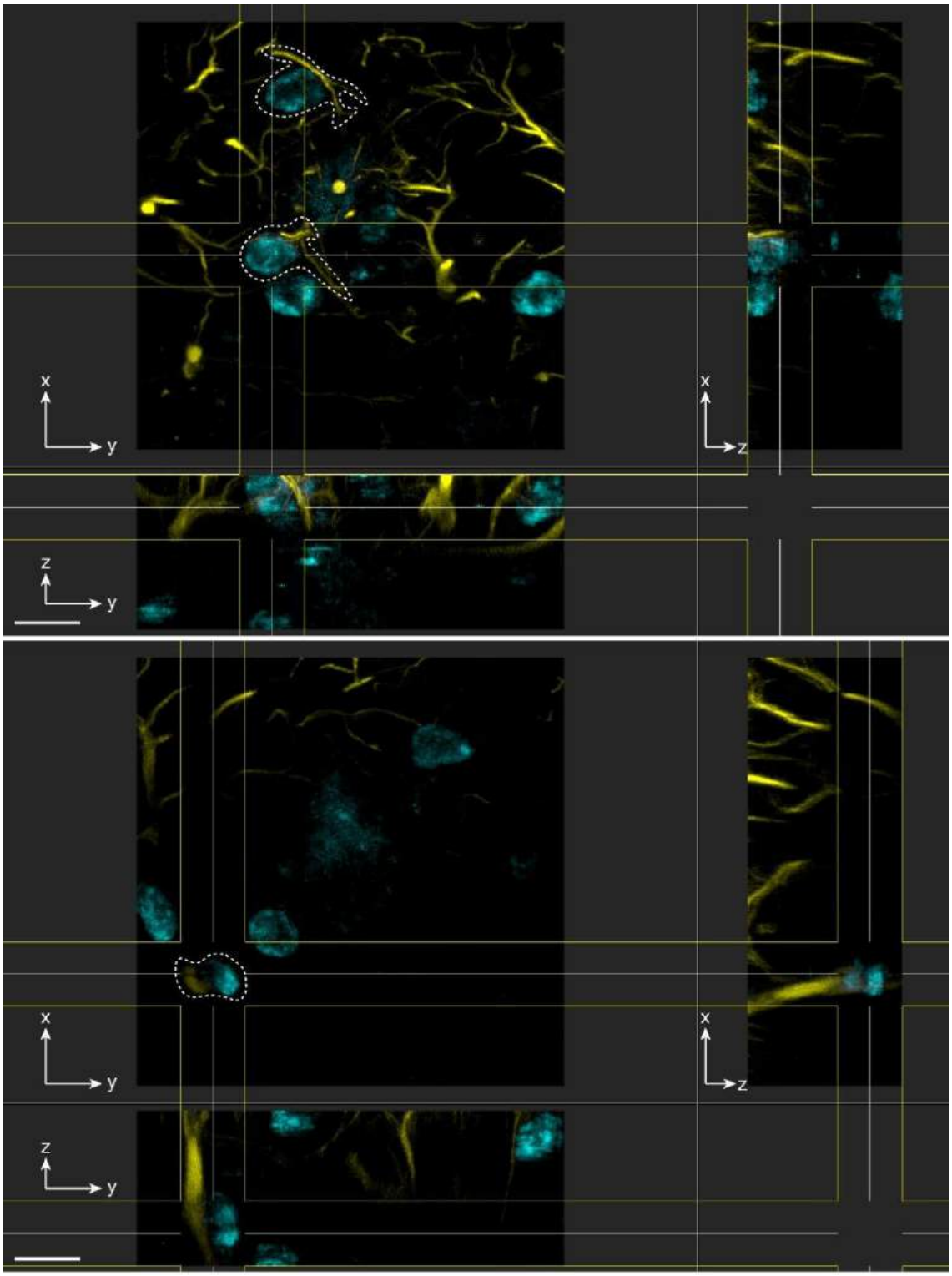
x
y
x
z
z
y
x
y
x
z
z
y

Fig. S8 Two maximum intensity projections of predicted DAPI (v-DAPI, cyan) and fluorescence-labeled GFAP (yellow) for the cell set shown in the second row of Fig. 6. The cells circled by dashed lines were identified as astrocytes based on the GFAP staining and the v-DAPI pattern.

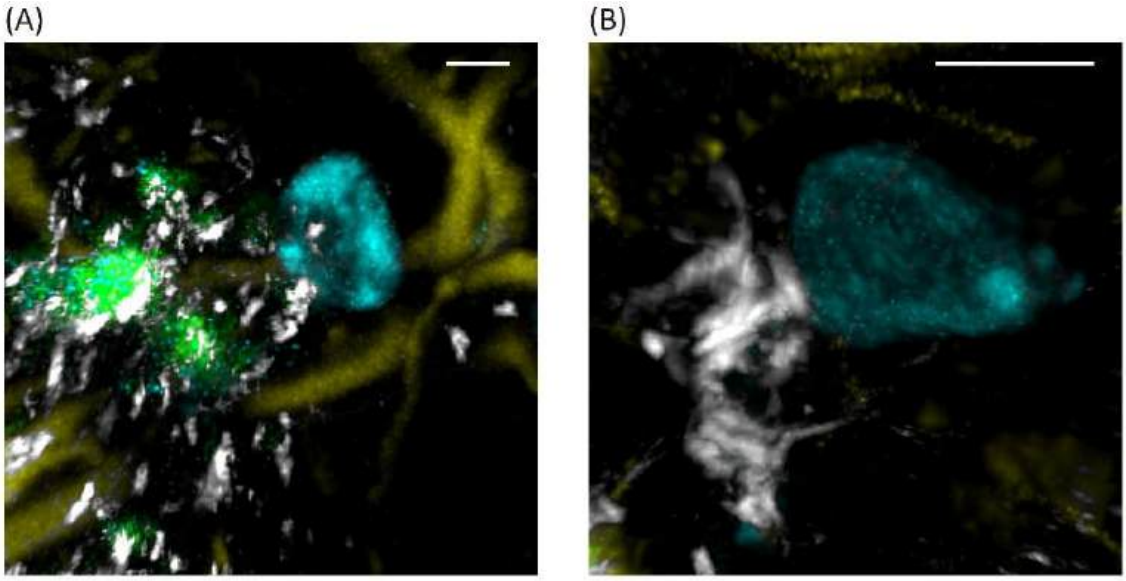

Fig. S9 Zoomed-in views of the dotted filament structure (A) and the ribbon-like structure (B) from the image set shown from the top row and the bottom row in Fig 6, respectively. Cyan: v- DAPI. White: v-peripheral plaque. Yellow: GFAP. Green: v-Congo red. Scale bars: 10 μm.

3. 7 References

1. Ross, C. A. & Poirier, M. A. Protein aggregation and neurodegenerative disease. *Nat. Med.* **10**, S10–S17 (2004).

2. Davies, S. W. *et al.* Formation of Neuronal Intranuclear Inclusions Underlies the Neurological Dysfunction in Mice Transgenic for the HD Mutation. *Cell* **90**, 537–548 (1997).
3. Hardy, J. & Selkoe, D. J. The Amyloid Hypothesis of Alzheimer's Disease: Progress and Problems on the Road to Therapeutics. *Science* **297**, 353–356 (2002).
4. Tanaka, M. & Komi, Y. Layers of structure and function in protein aggregation. *Nat. Chem. Biol.* **11**, 373–377 (2015).
5. Breydo, L. & Uversky, V. N. Structural, morphological, and functional diversity of amyloid oligomers. *FEBS Lett.* **589**, 2640–2648 (2015).
6. Li, L. *et al.* Real-time imaging of Huntingtin aggregates diverting target search and gene transcription. *eLife* **5**, e17056 (2016).
7. Lacor, P. N. *et al.* Aβ Oligomer-Induced Aberrations in Synapse Composition, Shape, and Density Provide a Molecular Basis for Loss of Connectivity in Alzheimer's Disease. *J. Neurosci.* **27**, 796–807 (2007).
8. Yang, T., Li, S., Xu, H., Walsh, D. M. & Selkoe, D. J. Large Soluble Oligomers of Amyloid β-Protein from Alzheimer Brain Are Far Less Neuroactive Than the Smaller Oligomers to Which They Dissociate. *J. Neurosci. Off. J. Soc. Neurosci.* **37**, 152–163 (2017).
9. Checler, F. & Turner, A. J. Journal of Neurochemistry special issue on Alzheimer's disease: 'amyloid cascade hypothesis--20 years on'. *J. Neurochem.* **120 Suppl 1**, iii (2012).

10. Bäuerlein, F. J. B., Fernández-Busnadiego, R. & Baumeister, W. Investigating the Structure of Neurotoxic Protein Aggregates Inside Cells. *Trends Cell Biol.* **30**, 951–966 (2020).
11. Mlodzianoski, M. J. *et al.* Active PSF shaping and adaptive optics enable volumetric localization microscopy through brain sections. *Nat. Methods* **15**, 583–586 (2018).
12. Querol-Vilaseca, M. *et al.* Nanoscale structure of amyloid-β plaques in Alzheimer's disease. *Sci. Rep.* **9**, 5181 (2019).
13. Bäuerlein, F. J. B. *et al. In situ* Architecture and Cellular Interactions of PolyQ Inclusions. *Cell* **171**, 179-187.e10 (2017).
14. Takasaki, K. T., Ding, J. B. & Sabatini, B. L. Live-Cell Superresolution Imaging by Pulsed STED Two-Photon Excitation Microscopy. *Biophys. J.* **104**, 770–777 (2013).
15. Duim, W. C., Jiang, Y., Shen, K., Frydman, J. & Moerner, W. E. Super-resolution fluorescence of huntingtin reveals growth of globular species into short fibers and coexistence of distinct aggregates. *ACS Chem. Biol.* **9**, 2767–2778 (2014).
16. Lu, M. *et al.* Structural progression of amyloid-β Arctic mutant aggregation in cells revealed by multiparametric imaging. *J. Biol. Chem.* **294**, 1478–1487 (2019).
17. Kaminski Schierle, G. S. *et al. In situ* Measurements of the Formation and Morphology of Intracellular β-Amyloid Fibrils by Super-Resolution Fluorescence Imaging. *J. Am. Chem. Soc.* **133**, 12902–12905 (2011).

18. Möckl, L. & Moerner, W. E. Super-resolution Microscopy with Single Molecules in Biology and Beyond–Essentials, Current Trends, and Future Challenges. *J. Am. Chem. Soc.* **142**, 17828–17844 (2020).

19. Bennett, R. E. *et al.* Tau induces blood vessel abnormalities and angiogenesis-related gene expression in P301L transgenic mice and human Alzheimer's disease. *Proc. Natl. Acad. Sci.* **115**, E1289–E1298 (2018).

20. Gamblin, T. C. *et al.* Caspase cleavage of tau: Linking amyloid and neurofibrillary tangles in Alzheimer's disease. *Proc. Natl. Acad. Sci.* **100**, 10032–10037 (2003).

21. Du, A. T. *et al.* Magnetic resonance imaging of the entorhinal cortex and hippocampus in mild cognitive impairment and Alzheimer's disease. *J. Neurol. Neurosurg. Psychiatry* **71**, 441–447 (2001).

22. Bartels, T., Schepper, S. D. & Hong, S. Microglia modulate neurodegeneration in Alzheimer's and Parkinson's diseases. *Science* **370**, 66–69 (2020).

23. Habib, N. *et al.* Disease-associated astrocytes in Alzheimer's disease and aging. *Nat. Neurosci.* **23**, 701–706 (2020).

24. Liebmann, T. *et al.* Three-Dimensional Study of Alzheimer's Disease Hallmarks Using the iDISCO Clearing Method. *Cell Rep.* **16**, 1138–1152 (2016).

25. Hama, H. *et al.* Sca l eS: an optical clearing palette for biological imaging. *Nat. Neurosci.* **18**, 1518–1529 (2015).

26. Ando, K. *et al.* Inside Alzheimer brain with CLARITY: senile plaques, neurofibrillary tangles and axons in 3-D. *Acta Neuropathol. (Berl.)* **128**, 457–459 (2014).

27. Murray, E. *et al.* Simple, Scalable Proteomic Imaging for High-Dimensional Profiling of Intact Systems. *Cell* **163**, 1500–1514 (2015).

28. Serrano-Pozo, A., Frosch, M. P., Masliah, E. & Hyman, B. T. Neuropathological Alterations in Alzheimer Disease. *Cold Spring Harb. Perspect. Med.* **1**, a006189 (2011).

29. Chen, G. *et al.* A learning deficit related to age and β-amyloid plaques in a mouse model of Alzheimer's disease. *Nature* **408**, 975–979 (2000).

30. Urbanc, B. *et al.* Neurotoxic effects of thioflavin S-positive amyloid deposits in transgenic mice and Alzheimer's disease. *Proc. Natl. Acad. Sci.* **99**, 13990–13995 (2002).

31. Kurouski, D., Duyne, R. P. V. & Lednev, I. K. Exploring the structure and formation mechanism of amyloid fibrils by Raman spectroscopy: a review. *Analyst* **140**, 4967–4980 (2015).

32. Shen, Y., Hu, F. & Min, W. Raman Imaging of Small Biomolecules. *Annu. Rev. Biophys.* **48**, 347–369 (2019).

33. Saar, B. G. *et al.* Video-Rate Molecular Imaging in Vivo with Stimulated Raman Scattering. *Science* **330**, 1368–1370 (2010).

34. Cheng, J.-X. & Xie, X. S. Vibrational spectroscopic imaging of living systems: An emerging platform for biology and medicine. *Science* **350**, aaa8870 (2015).

35. Ji, M. *et al.* Label-free imaging of amyloid plaques in Alzheimer's disease with stimulated Raman scattering microscopy. *Sci. Adv.* **4**, eaat7715 (2018).

36. Qian, C. *et al.* Super-Resolution Label-free Volumetric Vibrational Imaging. *bioRxiv* 2021.01.08.425961 (2021) doi:10.1101/2021.01.08.425961.

37. Wassie, A. T., Zhao, Y. & Boyden, E. S. Expansion microscopy: principles and uses in biological research. *Nat. Methods* **16**, 33–41 (2019).

38. Oakley, H. *et al.* Intraneuronal beta-amyloid aggregates, neurodegeneration, and neuron loss in transgenic mice with five familial Alzheimer's disease mutations: potential factors in amyloid plaque formation. *J. Neurosci. Off. J. Soc. Neurosci.* **26**, 10129–10140 (2006).

39. Kiskis, J. *et al.* Plaque-associated lipids in Alzheimer's diseased brain tissue visualized by nonlinear microscopy. *Sci. Rep.* **5**, 13489 (2015).

40. Ku, T. *et al.* Multiplexed and scalable super-resolution imaging of three-dimensional protein localization in size-adjustable tissues. *Nat. Biotechnol.* **34**, 973–981 (2016).

41. Perez-Nievas, B. G. & Serrano-Pozo, A. Deciphering the Astrocyte Reaction in Alzheimer's Disease. *Front. Aging Neurosci.* **10**, 114 (2018).

42. DeWitt, D. A., Perry, G., Cohen, M., Doller, C. & Silver, J. Astrocytes Regulate Microglial Phagocytosis of Senile Plaque Cores of Alzheimer's Disease. *Exp. Neurol.* **149**, 329–340 (1998).

43. Chui, H. C. & Ramirez-Gomez, L. Clinical and imaging features of mixed Alzheimer and vascular pathologies. *Alzheimers Res. Ther.* **7**, 21 (2015).

44. Khan, S., Rahmani, H., Shah, S. A. A. & Bennamoun, M. A Guide to Convolutional Neural Networks for Computer Vision. *Synth. Lect. Comput. Vis.* **8**, 1–207 (2018).

45. Ounkomol, C., Seshamani, S., Maleckar, M. M., Collman, F. & Johnson, G. R. Label-free prediction of three-dimensional fluorescence images from transmitted-light microscopy. *Nat. Methods* **15**, 917–920 (2018).

46. Ronneberger, O., Fischer, P. & Brox, T. U-Net: Convolutional Networks for Biomedical Image Segmentation. (2015).

47. Manifold, B., Thomas, E., Francis, A. T., Hill, A. H. & Fu, D. Denoising of stimulated Raman scattering microscopy images via deep learning. *Biomed. Opt. Express* **10**, 3860–3874 (2019).

48. Liddelow, S. A. *et al.* Neurotoxic reactive astrocytes are induced by activated microglia. *Nature* **541**, 481–487 (2017).

49. Heppner, F. L., Ransohoff, R. M. & Becher, B. Immune attack: the role of inflammation in Alzheimer disease. *Nat. Rev. Neurosci.* **16**, 358–372 (2015).

50. Koistinaho, M. *et al.* Apolipoprotein E promotes astrocyte colocalization and degradation of deposited amyloid-β peptides. *Nat. Med.* **10**, 719–726 (2004).

Chapter 4

HIGH-THROUGHPUT VOLUMETRIC MAPPING FACILITATED BY ACTIVE TISSUE SHRINK

Lin, L. E., Colazo, A., Bi, X., Du, J., & Wei, L. (2025). High-Throughput Volumetric Mapping Facilitated by Active Tissue SHRINK. *Small Methods*, 2500382. doi: 10.1002/smtd.202500382

4. 1 Summary

Comprehensive visualization of tissue architecture in large organs such as the brain is crucial for understanding functional relationships across key tissue regions. However, the large size of whole organs makes it challenging to image their entirety at the subcellular resolution, often requiring prolonged imaging sessions, volume reconstruction, and compromises in spatial coverage. Here, we report Scalable Hydrogel-embedded Rapid Imaging of tissue NetworK (SHRINK) to address this challenge through active tissue shrinkage and clearing. Utilizing the identified hydrogel network to preserve the spatial pattern of proteins *in situ* and remove the uncrosslinked biomolecules to create space, we showed that SHRINK isotropically drives the reduction of sample sizes down to 16% of its original volume while maintaining high cellular and tissue-level integrity in a reversible manner. The size reduction and the corresponding three-dimensional (3D) concentrating of the biomolecules renders a more than 6-fold enhancement for throughput and signal respectively, which addresses a key bottleneck for the

stimulated Raman scattering (SRS) microscopy, ideal for 3D label-free, metabolic, and super-multiplex tissue mapping. We further demonstrated that SHRINK-SRS achieves organ-scale mapping of brain, intestine, heart, and kidney tissues with refractive-index matched sample-clearing. SHRINK offers a powerful approach to overcome traditional imaging barriers, enabling rapid and detailed visualization of large organs.

4. 2 Introduction

Holistic tissue mapping with subcellular resolution has significantly facilitated our understanding of tissue architecture and cellular functions in their native three-dimensional (3D) context. Fluorescence-based tissue imaging techniques have revolutionized our understanding of complex tissues, such as the brain, as well as whole organs and animals, by uncovering unprecedented insights into their physiology and pathology[1–3]. Complementing these advances, chemical imaging methods like stimulated Raman scattering (SRS) microscopy offer minimally invasive, label-free, and highly multiplexed imaging capabilities, expanding imaging boundaries and delivering comprehensive perspectives on tissue structure-function relationships[4–7]. Importantly, SRS enables direct and quantitative visualization of biomass in biological samples, allowing for an accurate assessment of sample conditions. However, imaging scalability and throughput still pose a major challenge for optical volumetric tissue mapping. Optical scattering limits the depth of 3D imaging due to reduced light penetration into tissue[8–10]. Furthermore, scaling up from small tissue samples to large

volumes, such as moving from mouse to human tissues, requires significantly extended imaging acquisition. For example, the human brain is approximately 2,800 times the size of a mouse brain[11–13]. Even with state-of-the-art high-speed light-sheet microscopy, full imaging of a single human brain at micron resolution requires more than 10 weeks[14,15].

Over the last decade, extensive efforts have been made to address the limited light penetration for optical deep-tissue imaging. In particular, tissue clearing techniques have drastically enhanced the depth of 3D fluorescence imaging for histological profiling at the whole organ level without introducing sectioning artifacts and tedious image re-alignment for volumetric analysis. These strategies address the light scattering inside tissues by homogenizing the refraction index (RI) of the samples and then matching the RI with corresponding immersion solvents[16–34]. However, active-sample-engineering strategies remain underexplored for tackling the scalability challenges associated with imaging significantly larger and more physiologically relevant tissues, such as human samples, leaving the valuable information from these rare samples largely inaccessible.

Tissue clearing techniques are known to alter tissue sizes, which can be advantageous for imaging. For example, water-based strategies often lead to tissue swelling, which was leveraged as an active sample-swelling technique, widely known as expansion microscopy (ExM). ExM enables scalable super-resolution imaging on conventional microscopes across various tissue types. In

contrast, hydrophobic methods often induce minor tissue shrinkage due to the removal of water and lipids, which enhances transparency and reduces tissue size. This property was leveraged by methods such as ultimate 3D Imaging of Solvent-Cleared Organs (uDISCO) to improve imaging throughput. uDISCO was reported to reduce the volume of intact central nervous system in adult rats by up to 65%, with an average volume reduction of 50% in mouse brains[32]. This size reduction enhances overall imaging speed and helps mitigate physical limitations related to working distance and the focusing range of microscope objectives. However, even a volume reduction of 65%, equating to an isotropic shrink factor of 0.70, provides only modest improvements in signal strength and imaging throughput.

In this manuscript, we introduce SHRINK (Scalable Hydrogel-embedded Rapid Imaging of tissue NetworK), an active hydrogel-based tissue-shrinking technique (**Fig. 1a**) to significantly improve imaging throughput via sample volume reduction and the corresponding signal enhancement. A comparison of tissue clearing methods that induce shrinkage is provided in **Table S1**. SHRINK achieves this by efficiently retaining proteins *in situ* via hydrogel hybridization and removing lipids and water to create needed space for optimal tissue size reduction. Importantly, the hydrogel network maintains essential mechanical stability of the tissue during the shrinking process, preserving the structural integrity at the subcellular level. The resulting concentrated proteins in 3D within the diffraction-limited focus spot further enhances signals, enabling extra sensitive detection of low-abundance targets, which also addresses a key bottleneck, the detection sensitivity, of performing functional SRS

microscopy. Through rational analysis and screening, we identified a polymer network optimized for achieving isotropic shrinkage while preserving structural integrity. Using this approach, we demonstrated that SHRINK is compatible with both fluorescence and SRS microscopy, achieving an unprecedented 6.3-fold volume reduction and a 7-fold signal enhancement. Notably for SRS imaging, these combined effects of volume reduction and signal enhancement equals to an over 300-time faster imaging throughput under the same shot-noise-limited detectability. We demonstrate SHIRNK-SRS imaging through a 1.5 mm thick mouse brain tissue while maintaining subcellular resolution, and showed its general applicability with rat intestine, kidney, and heart with refractive-index matched sample-clearing. Importantly, SHRINK enables reversible sample shrinking and rehydration, supporting scalable and reversible investigations at even higher-resolution imaging on valuable samples as needed.

4. 3 Results

Identification of the optimal SHRINK polymer network

To maximize sample shrinkage, we hypothesized that the tissue-gel hybridization strategy could be leveraged to retain proteins efficiently while actively driving the tissue shrinkage through detergent washes, dehydration, or modulation of the osmotic pressure of the surrounding environment (**Fig. 1a**)[4,5,35–38]. We expected this strategy to achieve much-improved linear shrinking ratios compared to the shrinkage observed with uDISCO , while robustly preserving tissue architecture. To screen for the best polymer network, along with

the optimal detergent washing conditions and RI matching solvent, we designed the following five-step protocol: (i) fixation, (ii) gelation, (iii) detergent wash, (iv) dehydration for sample shrinkage, and (v) RI matching for deep tissue imaging (**Fig. 1b, tissue view and Fig. 1c, cellular view**).

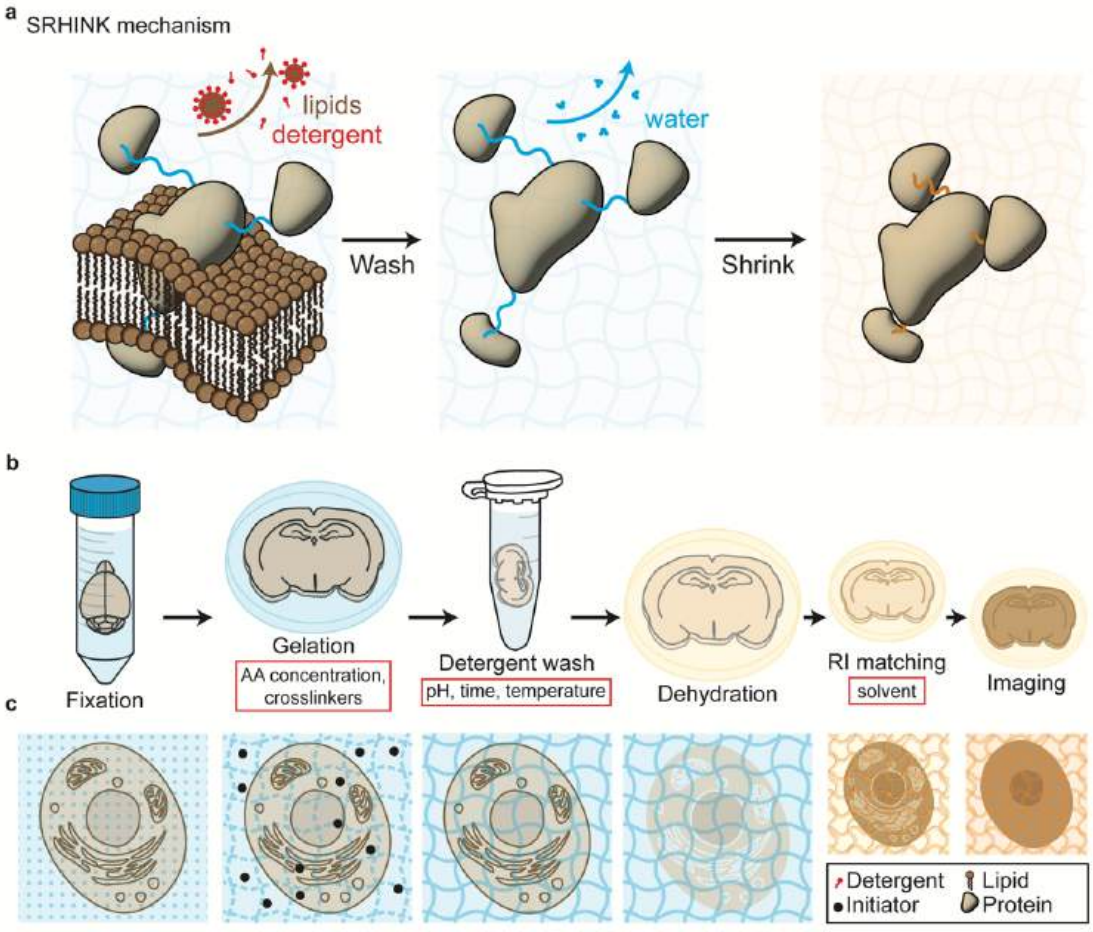

Fig. 1: Schematics and mechanism of SHRINK. (a) Molecular-level view of SHRINK: proteins are anchored by the polymer hydrogel, and unanchored biomolecules such as lipids are removed before the samples are subject to active shrinkage driven by the hydrogel. (b-c) Tissue-level (b) and the corresponding

cell-level (c) views of the SHRINK protocol pipeline. Key steps involved in SHRINK screening are highlighted in red boxes.

In the hydrogel-based ExM, tissues are typically incubated and fixed directly in 4% PFA in PBS. Then, a high concentration of the ionic monomer sodium acrylate is used in the gelation step to retain more water in the hydrogel mesh, enabling maximal sample expansion[39,40]. For SHRINK, a high concentration of acrylamide (AA) was introduced to maximize protein retention during incubation .[4,37] Additionally, we found that sodium acrylate's high water absorption capacity hindered sample shrinkage during dehydration. Therefore, in our design, we reformulated the SHRINK gelation solution to be charge-neutral by using only AA as the monomer. To ensure uniform polymerization at the tissue scale, we selected VA-044, a thermally activated initiator that diffuses into the tissue and enables homogeneous polymerization upon heating. After hybridization, the hydrogel mesh serves as the new structural backbone of the tissue, with proteins anchored to it, thereby preserving tissue integrity during shrinkage.

We expected that high osmotic pressure solutions should suffice for shrinkage. However, even with saturated saline, the shrunken tissue size remained above 90% of the original, which is not even as effective as the reduction achieved by uDISCO[32]. We next turned to the complete depletion of water by gradient dehydration and tested its effectiveness across different crosslinkers (**Fig. 2a and Table S2**)[41]. Successful shrinkage was achieved by immersing the gel samples in

a solution mixture with a gradient increase of tert-butanol, leading to a two-fold isotropic reduction in diameter (**Figure S1**). However, sample distortion was observed because the gel in contact with the tert-butanol solution shrank faster than that from the interior. This inhomogeneous shrinkage resulted in an unevenly hardened and curly shell wrapping around the tissue, as illustrated by the gel formed with N,N-Methylenebis(acrylamide) (BIS), the most widely used crosslinker for protein electrophoresis and ExM (**Fig. 2b**).

To address the severe sample distortion, we speculated that using N,N′-(1,2-dihydroxyethylene)bisacrylamide (DHEBA), a reversible crosslinker known to undergo mild decomposition under detergent wash, could solve this issue[42]. Indeed, the non-tissue-embedded portion of DHEBA undergoes partial decomposition while nicely maintaining the tissue integrity in the tissue-embedded portion, leading to the desired flat tissue-gel hybrid after the dehydration (**Fig. 2c**). We further screened other crosslinkers, including piperazine di-acrylamide (PDA), N,N′-bis(acryloyl)cystamine (BAC), and N,N'-diallyl-L-tartardiamide (DATD), but found that these samples all formed undesirable distortions caused by faster edge shrinkage and the formation of a non-transparent shell (**Fig. 2d**) [43–47].

After identifying DHEBA as the most suitable crosslinker, we further optimized the heating temperature, pH, and the duration of the detergent wash given DHEBA's sensitivity to heat and pH. Using label-free SRS imaging

targeting the CH_3 total-protein channel at 2940 cm^{-1}, we determined that a temperature of 75°C and a pH of 7 provided optimal conditions for selectively removing excess gel without invoking sample deterioration (**Figure S2**). The heating duration ranged from 6 to 16 hours depending on the sample sizes. Tissue damage started to occur when the denaturing buffer pH exceeded 7, temperatures rose above 75 °C, or the heating time exceeded 22 hours. To ensure optical transparency for deep-tissue profiling, we next optimized the final RI-matching solvents for imaging. Since the sample contains a mixture of highly concentrated protein (RI ~1.5–1.6) and acrylamide gel (RI ~1.45). To identify suitable solvents, we screened common organic solvents with refractive indices between 1.45 and 1.6 that are optically transparent in the visible range for fluorescence imaging and key vibrational imaging channels (e.g., 2100–2200, 2845, and 2940 cm^{-1}) used in SRS chemical imaging in the near-infrared region. With label-free SRS imaging at 2940 cm^{-1}, we quantitatively measured the signal attenuation coefficients and determined that the RI matching solution composed of benzyl alcohol, benzyl benzoate, and diphenyl ether (BABB-D15)[32] outperformed other tested solvents with more than a 2.5-fold smaller attenuation coefficient, at $1.22 \times 10^{-3} \pm 2.32 \times 10^{-4}$ μm^{-1} (**Fig. 2e** and **Table S3**).

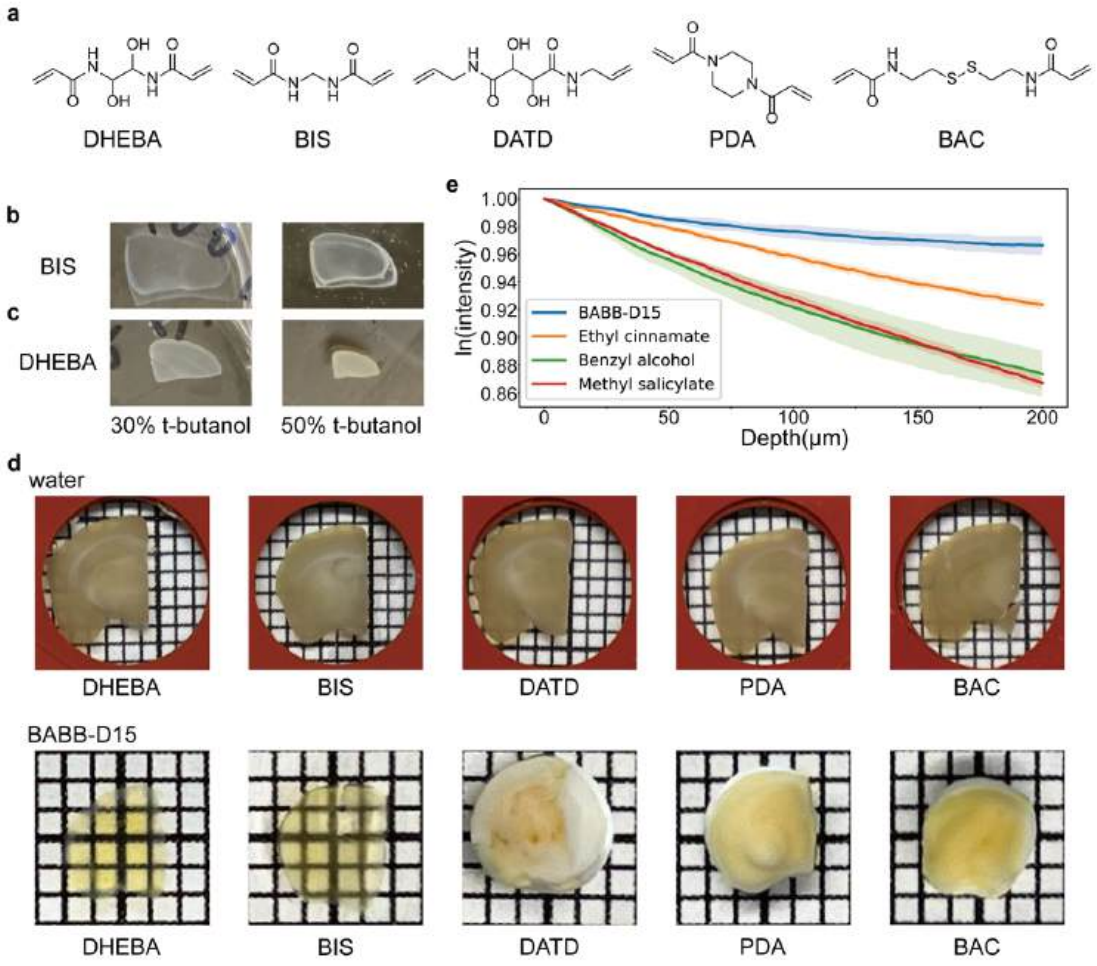

Fig. 2 Identification of the optimal crosslinker and RI matching solvent for SHRINK. (a) Structures of screened crosslinkers for tissue-gel hybridization. (b-c) Shrinkage during dehydration with 30% and 50% t-butanol of tissue-gel hybrid made with N,N-Methylenebis(acrylamide) (BIS) (b) and N,N′-(1,2-dihydroxyethylene)bisacrylamide (DHEBA) (c) as cross-linkers. BIS showed uneven shrinkage, with the outer portion shrinking faster. (d) Crosslinker screening with 600 μm brain tissue slices. The DHEBA sample was transparent and did not form an opaque polymer shell. Grid size: 1mm. (e) Signal attenuation with imaging depth measured by SRS imaging at 2940 cm^{-1} with DHEBA-

mediated shrunk brain tissue samples immersed in various RI matching solutions. Data represent mean values (n = 4), with shading indicating the standard deviation.

SHRINK offers signal enhancement for tissue imaging with reversible imaging capability

We next quantitatively compared the same tissue before and after shrinkage by SRS imaging and determined an average linear shrinkage ratio of 0.54 ± 0.03 fold (**Fig. 3a-c**, n = 6). Although this results in a 1.85-fold decrease in resolution, subcellular imaging with a resolution of approximately about 600 nm remains achievable[4]. We note that in this case, the gain largely outweighs the loss — the slight decrease of the resolution leads to a large reduction (i.e. 6.35-fold) of the volume, and hence significantly improved signal sizes (due to increased molecule concentration within the laser focal spot) and imaging throughput (from volume reduction). We note that unprocessed brain tissues contain high concentrations of lipids, causing the cell nuclei to appear darker than the lipid-rich surroundings in the label-free CH_3 channel (2940 cm^{-1}, **Fig. 1a**) due to the spectral bleed through from the CH_2 lipid channel at 2845 cm^{-1} (**Figure S3a-b**). Since only proteins are retained on the hydrogel mesh, nuclei become distinct after SHRINK (**Fig. 1b** and **Figure S3c-d**). As SRS signal intensity is linearly dependent on the density of the probed chemical bonds, we quantified the CH_3 signal enhancement from the nuclei to be 6.82 ± 0.11 fold (**Fig. 3d-f**), consistent with the previous estimation. The slight increase in signal enhancement beyond the pure contribution from

volume reduction may be due to improved sample transparency from RI matching.

To demonstrate the general potential of SHRINK, we further tested pre-resonance SRS imaging of nitrile bond (2200 cm^{-1}, with a bandwidth of about 15 cm^{-1}) from the reported MARS2200 dye, which produces one of the strongest Raman signals in the narrow-bond mode for optical super-multiplex imaging[48,49]. Using MARS2200 conjugated secondary antibody to label glial fibrillary acidic protein (GFAP), an astrocyte marker, in brain tissues, we obtained a signal enhancement of 16.13 ± 0.92 fold from the same samples before and after SHRINK (**Fig. 3g-i**). Notably, the signal enhancement factor is significantly larger than the shrinkage ratio, possibly due to the dye's higher quantum yield in the SHRINK environment. Such enhancement could significantly facilitate color expansion in super-multiplex pre-resonance SRS imaging, where sensitivity is a severe limiting factor for accessing versatile biomolecules to achieve one-shot multiplexing imaging and profiling[50]. We further benchmarked SHRINK with fluorescence microscopy, and similarly obtained the signal enhancement factor of 5.68 ± 0.75 from Alexa-647 immuno-labeled GFAP of the same brain tissues before and after SHRINK (**Fig. 3j-l**). These results also suggest a high potential for SHRINK in tissue-level fluorescence imaging, particularly for low-abundance targets where the signal-to-autofluorescence background ratio (SBR) poses a limiting challenge.

SHRINK is further envisioned for high-throughput screening, followed by detailed examination using reversible sample expansion. This approach is especially valuable for large and precious samples like human tissues. With most proteins preserved and the shrinkage process reversible, multiple rounds of imaging are possible for more comprehensive investigations. By washing off the RI matching solution with isopropanol and gradually rehydrating the tissue with a reversed tert-butanol gradient, we confirmed that the sample could be returned to its original size for ATTO680 immunolabeled brain tissue, and be re-shrunk again without significant loss in signal (**Figure S4**). Similar to MARS2200 imaging result in **Fig 3g-i**, the signal enhancement factor is also larger than the shrinkage ratio.

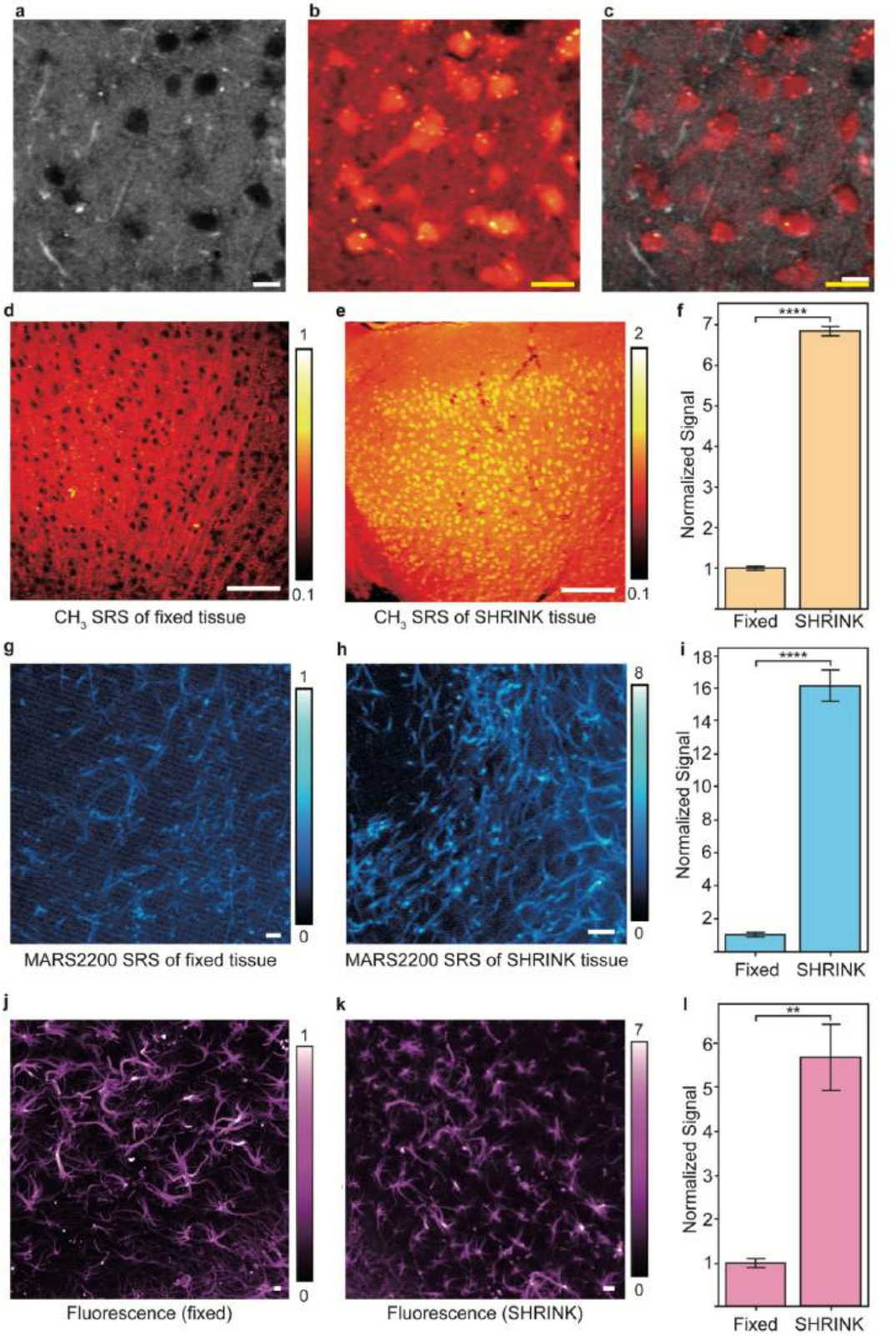
a
b
c
d
1
0.1
CH3 SRS of fixed tissue
e
2
0.1
CH3 SRS of SHRINK tissue
f
****
Normalized Signal
Fixed
SHRINK
g
1
0
MARS2200 SRS of fixed tissue
h
8
0
MARS2200 SRS of SHRINK tissue
i
****
Normalized Signal
Fixed
SHRINK
j
1
0
Fluorescence (fixed)
k
7
0
Fluorescence (SHRINK)
l
**
Normalized Signal
Fixed
SHRINK

Fig. 3. Quantitative characterization of the shrinkage ratio and signal enhancement of SHRINK with label-free SRS imaging, pre-resonance SRS dye, and fluorophore immuno-imaging. (a-c) Characterization of brain tissue shrinkage. (a) SRS image (at 2940 cm^{-1}) of mouse brain tissue fixed with 30% AA and 4% PFA in PBS. (b) SRS image (at 2940 cm^{-1}) of the same tissue after shrinkage. (c) Overlay of images before and after shrinkage. No obvious changes in cell location and morphology were observed. (d-f) Fixed (d) and SHRINK (e) tissue SRS imaging (2940 cm^{-1}) in a brain cortex region. (f) A 6.82 ± 0.11 fold enhancement for nucleus regions after SHRINK is obtained. Data represent mean values (n = 105 for Fixed, n = 215 for SHRINK), with error bars indicating the standard deviation. ****: $P < 0.00001$. (g-i) Fixed (g) and SHRINK (h) GFAP stained tissue with MARS2200 imaged at 2200 cm^{-1} by pre-resonance SRS from a brain cortex region. (i) a 16.13 ± 0.92 fold enhancement after SHRINK is achieved. Data represent mean values (n = 4 for Fixed, n = 4 for SHRINK.), with error bars indicating the standard deviation. ****: $P = 0.00007$. (j-l) Fluorescence images of Alexa-647 GFAP stained fixed (j) and SHRINK (k) tissue. (l) 5.68 ± 0.75 fold enhancement after SHRINK is shown. Data represent mean values (n = 4 for Fixed, n = 4 for SHRINK.), with error bars indicating the standard deviation. **, $P = 0.0015$. Scale bars: 10 μm.

SHRINK enables deep and large-scale mapping

Recognizing SHRINK's potential for high-throughput label-free SRS imaging, we demonstrated its applicability for deep tissue imaging across multiple organs. As mentioned above, under the same imaging parameter, SHRINK reduces the total imaging time to just 0.3% of the original, significantly boosting throughput. This improvement originates from the combined effects of a 6.3-fold reduction in volume and a 6.8-fold enhancement in signal, which equals a 6.8^2-fold reduction in acquisition time required to achieve the same shot-noise-limited signal-to-noise ratio (S/N) in SRS. Our mosaic SHRINK-SRS imaging (**Fig. 4a**) for a 1.5 mm mouse brain hemisphere revealed well-defined brain regions from the cortex to the corpus callosum and the nucleus accumbens (**Fig. 4b**), with distinct protein distributions aligning with known anatomical patterns. Depth profiling of the hippocampal region (**Fig. 4c**) outlined the dentate gyrus, and the striatum region (**Fig. 4d**) showed the characteristic striped pattern of white and gray matter. These results demonstrate that SHRINK is highly effective for volumetric imaging, enabling clear differentiation of distinct tissue structures within the brain.

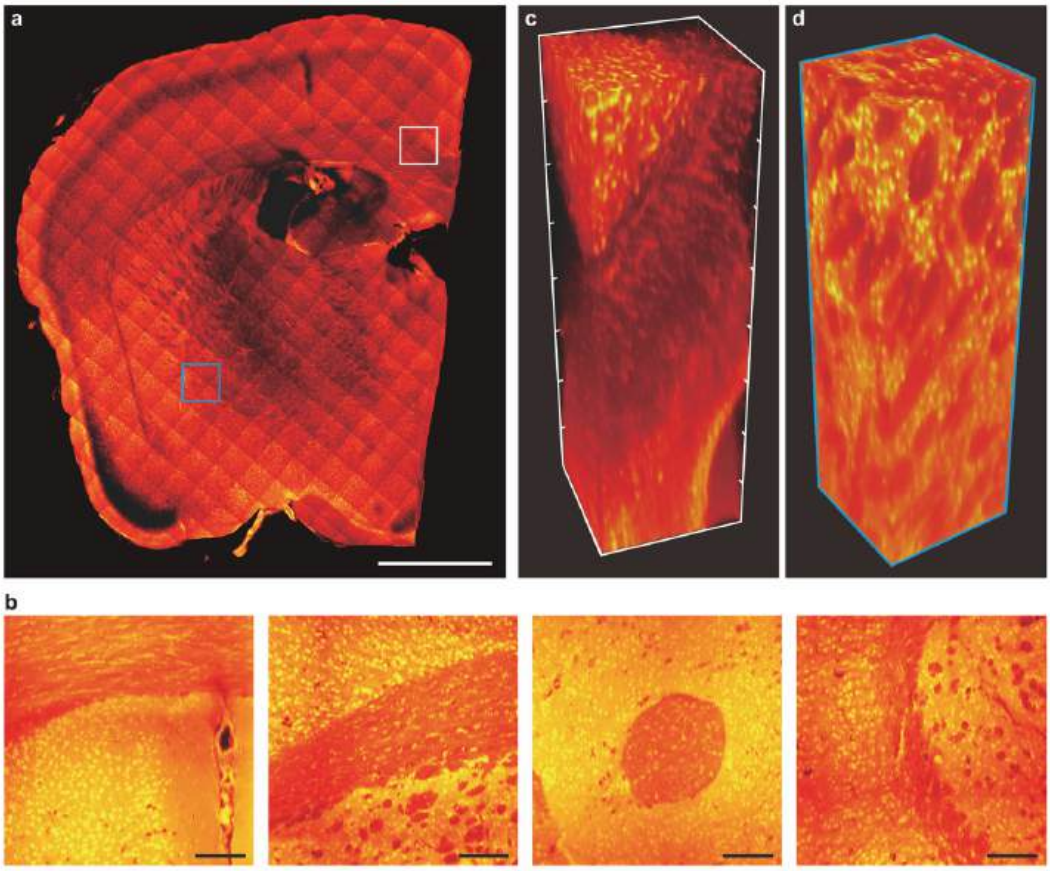

Fig. 4. High-throughput deep-tissue label-free mapping (at 2940 cm^{-1}) of the mouse brain. (a) Mosaic SHIRNK-SRS mapping for a 1.5 mm half mouse brain hemisphere. (b) Representative 2D imaging of the SHRINK tissue at the corpus callosum and nucleus accumbens. (c) Depth profiling of the hippocampal region. (d) depth profiling of the striatum. Scale bars: 1 mm (a), 100 μm (b-d)

We further explored the compatibility of SHRINK for high-throughput mapping of other rodent tissue organs. For instance, the mucosa, often prone to separation from the underlying submucosa during collection, remained intact through the SHRINK process, demonstrating SHRINK's capacity to preserve the native architecture of

delicate tissue layers (**Fig. 5a**, left). Through depth-resolved SHRINK-SRS imaging, we achieved high-resolution visualization of intestinal villi (Fig. 5a, right). In addition, in whole kidney samples from mice, large field-of-view SHRINK-SRS imaging revealed intricate renal tubular structures (**Fig. 5b**, left), while deep profiling uncovered the complex architecture of the collecting ducts of the renal papilla and the dilated renal pelvis (**Fig. 5b**, right). Notably, SHRINK-SRS enabled whole-heart imaging, clearly delineating cardiac fiber architecture and the septum separating the left and right ventricles (**Fig. 5c**, left). Depth imaging further showcased the complete heart wall, emphasizing SHRINK's power to penetrate and resolve details within thick muscle tissues with high throughput (**Fig. 5c**, right). Together, these findings underscore SHRINK's remarkable flexibility and capability for preserving and imaging diverse and complex organ systems in 3D, opening new possibilities for high-throughput structural analysis across multiple tissue types. With the significantly improved profiling power and the reversible scalability, we also envision SHRINK to find utility in enhancing our understanding of the intricate relationships of spatial cellular distribution and tissue architecture, especially in pathological contexts such as cancer or neurodegenerative disease tissues.

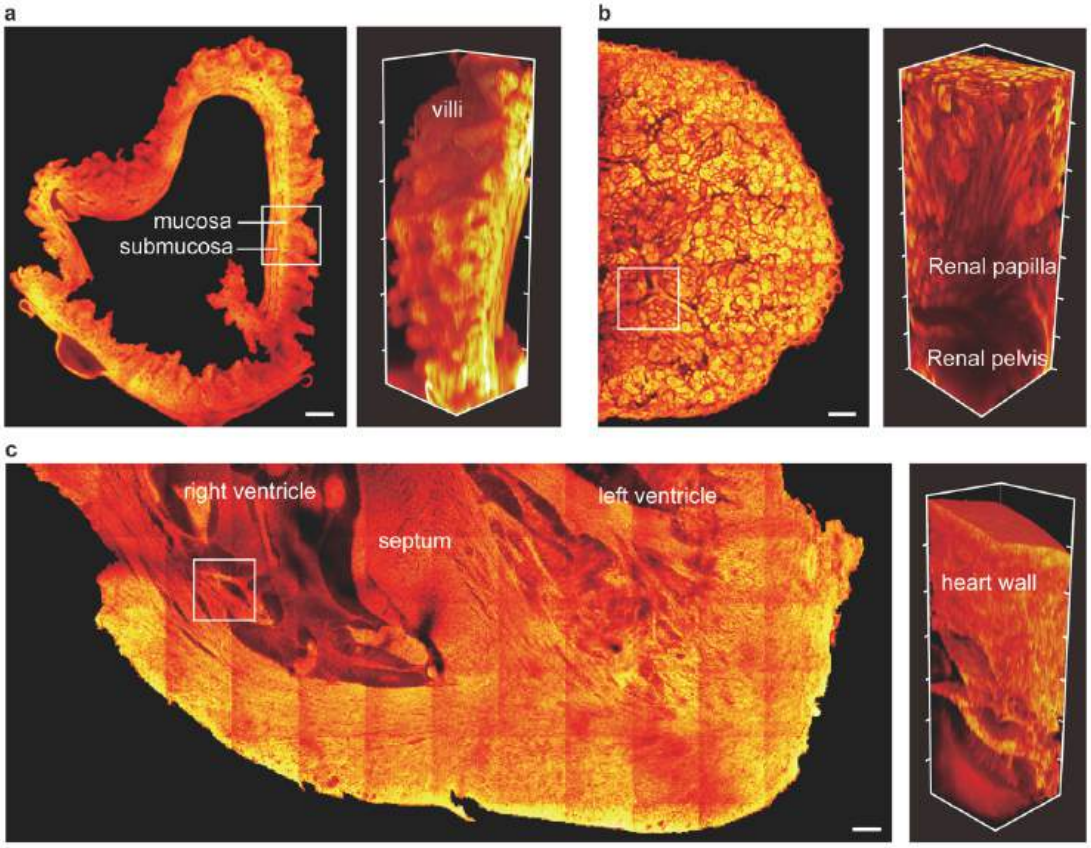

Fig. 5: 3D SHRINK-SRS label-free mapping (at 2940 cm^{-1}) of rat organ tissues. (a-c) Representative mosaic SHRINK mapping (left) and depth imaging (right) of a rat intestine (a), kidney (b), and heart (c). Scale bars: 100μm.

4. 4 Discussion

In summary, we established SHRINK as a robust and flexible tissue shrinkage and clearing method for high-throughput deep tissue imaging, achieving a volume shrinkage factor as low as 16%. We demonstrated the significant advances of

SHRINK combined with both label-free SRS and pre-resonance SRS imaging, addressing key sensitivity challenges and boosting the potential for high-throughput, high-sensitivity, and highly multiplexed biomedical SRS applications across large tissue volumes. We further showed that SHRINK is compatible with conventional immunostaining methods for fluorescence imaging, suitable for fast screening of tissue samples, and can be scalable with expansion for further investigation. SHRINK hence represents a valuable addition to the versatile tissue-clearing toolsets, offering enhanced shrinkage, protein preservation, signal enhancement, and compatibility with various imaging techniques. Its reversibility and suitability for multi-round imaging also make it an invaluable tool for comprehensive tissue analysis.

In SHRINK, tissues are incubated in a high concentration of acrylamide with 4% PFA to retain most proteins. This process allows immunostaining after denaturing the sample through washing, as well as re-staining after rehydration. However, the retention of protein, which constitutes 30-60% of brain tissue dry mass[51], may limit further shrinkage. Combining SHRINK with other hydrogel-based expansion methods that do not retain molecules at high density, such as pre-expansion labeling methods[36,38,52,53], could potentially allow for even greater reductions in sample volume through enhanced shrinkage. Since SHRINK utilizes the cleavable crosslinker DHEBA, it is potentially compatible with iterative expansion (iExM)[53], enabling linear sample scaling up to 100-fold (0.6x to 60x). SHRINK can also potentially be applied to other biomolecules beyond proteins

with suitable crosslinkers for lipids[54–56], nucleic acids[57–60], and universal cross-linking strategies[61,62]. Further exploration also includes imaging of amide I (~1650 cm^{-1}), amide III (~1240 cm^{-1}), or other side-chain-specific vibrational modes to investigate specific protein structures throughput the entire tissue via SHRINK[63,64].

4. 5 Methods and materials

Reagents and materials

Sodium acrylate, acrylamide (AA), N,N'-methylenebisacrylamide (BIS, 2% in water), N,N′-(1,2-dihydroxyethylene)bisacrylamide (DHEBA), N,N′-Bis(acryloyl)cystamine (BAC), N,N'-Diallyl-L-tartardiamide (DATD), and piperazine diacrylamide (PDA) were purchased from Sigma-Aldrich. Tris(hydroxymethyl)aminomethane was obtained from Biosolve. Nuclease-free water, tert-butanol (t-butanol), benzyl alcohol (BA), Diphenyl ether (DPE), N,N-dimethylacrylamide (BIS), methyl salicylate, ethyl cinnamate, dibenzyl ether, VA-044, and bovine serum albumin (BSA) were acquired from Thermo Fisher. Paraformaldehyde (PFA, 16% in water) was purchased from Electron Microscopy Sciences.

Anti-glial fibrillary acidic protein (anti-GFAP, 3670S) was purchased from Cell Signaling Technology, and goat anti-mouse antibodies (31160 and A-21235) were

purchased from Invitrogen. ATTO NHS-ester dyes were purchased from ATTO-TEC GmbH.

Secondary antibody-dye conjugation

All MARS NHS-esters were synthesized as previously reported and stored as 10 mM DMSO solutions[48,49]. Before conjugation, the secondary antibody was diluted to 2 mg/mL with 0.1 M $NaHCO_3$. To adjust the pH to approximately 8.3, one-tenth volume of 1 M $NaHCO_3$ was added to the antibody solution. For the conjugation reaction, MARS NHS-ester dye was introduced at a dye-to-protein ratio of 15:1. This mixture was incubated in the dark with gentle stirring for 1 hour at room temperature.

Excess dye was removed using gel permeation chromatography. Sephadex G-25 was first swelled at 90°C for 1 hour, then used to pack a column with a diameter of 0.5 cm and a length of 15 cm. Post-reaction, the solution was applied to the column, and the eluted dye bands were collected. The conjugated proteins were then concentrated to a concentration of 1–2 mg/mL in PBS using 10 kDa Amicon ultra-centrifugal filters (UFC501096, EMD, Millipore). The final concentration was determined using a Thermo Scientific NanoDrop. The resulting antibody solutions were kept at 4 °C. The ATTO dye conjugates were obtained following the same protocol.

Tissue samples

Brain tissues from C57BL/6J mice were obtained from The Jackson Laboratory. Rodents were euthanized using the standard CO_2 method without perfusion. Post-mortem brain tissues were frozen in liquid nitrogen or on dry ice and stored at -80°C, then shipped on dry ice. Upon arrival, the brain tissues were washed and fixed in 30% AA and 4% PFA at 4°C for three days and at 37°C for one day. The tissues were then sectioned into 500-1500 μm slices using a Leica VT 1200S vibratome and stored at 4°C. Rat organs were isolated from neonatal Sprague–Dawley rat (CD (Sprague–Dawley) IGS rat, Charles River) pups with a protocol (IA22-1835) approved by Caltech's Institutional Animal Care and Use Committee (IACUC), and fixed in 30% AA and 4% PFA at 4°C for three days and at 37°C for one day.

SHRINK procedure

The incubation solution (30% AA, 4% PFA in PBS) and gelation solutions (10% AA, 0.1% DHEBA, 0.1% VA-044 in PBS) were freshly prepared and stored at 4 °C before use. The tissue was incubated in the gelation solution for 1 hour at room temperature with gentle shaking, followed by heating to 45 °C for 2 hours to induce gelation.

After gelation, the sample-embedded gel was immersed in the denaturing buffer (200 mM SDS, 200 mM NaCl, and 50 mM Tris in nuclease-free water, titrated to pH 7) for 15 minutes at room temperature, and transferred into a 2 mL Eppendorf tube with 1.5 mL of denaturing buffer. The sample was denatured by heating at 75 °C for 6–18 hours in the tube. It was then transferred to nuclease-free water and

washed three times for 1–2 hours each. The sample was dehydrated sequentially in 30%, 50%, 70%, 90%, and 96% t-butanol with gentle shaking, followed by incubation in 100% t-butanol at 37 °C. Finally, the sample was transferred to BABB-D15 (BA:BB:DBE, 5:10:1 v/v/v) for at least 2 hours with shaking before imaging.

Immunostaining

The tissue-gel hybrid was transferred to 2 mL of PBST solution (1% Triton X-100 in PBS) and incubated with primary antibodies at a 1:100–1:200 dilution at 37 °C for 24 hours, followed by washing three times with PBST at 37 °C for 1–2 hours each. The samples were then incubated with secondary antibodies at a 1:200 dilution in PBST at 37 °C for 18–24 hours, followed by washing three times with PBST at 37 °C for 1–2 hours each before imaging.

Fluorescence imaging

The fluorescence images of the processed samples with fluorescent labels were obtained with a 4 μs pixel dwell time by a 25×, 1.05 NA water-immersion objective with the Olympus Fluoview system. Single-photon confocal laser scanning imaging was performed with a 640 nm laser (Coherent OBIS). The images were analyzed with Fiji or Imaris.

Stimulated Raman scattering (SRS) microscopy

The picoEmerald laser system (Applied Physics & Electronics) generated both the pump and Stokes beams used in this setup. The tunable pump beam had a wavelength range of 770 nm to 990 nm and a spectral bandwidth of approximately 7 cm^{-1}, while the Stokes beam had a fixed wavelength of 1031.2 nm and a spectral bandwidth of 10 cm^{-1}. These beams operated at an 80 MHz repetition rate, with the Stokes beam being modulated at 20 MHz via an integrated electro-optic modulator (EOM). Within the picoEmerald system, the pump and Stokes beams were synchronized both spatially and temporally before being directed into an Olympus FV3000 microscope. The Raman loss signal from the pump beam was demodulated using a lock-in amplifier (SR844 from Stanford Research Systems) at the modulation frequency. The in-phase output signal was fed back into the Olympus IO interface box (FV30-ANALOG) of the microscope. Image acquisition speed was set at 40 μs pixel dwell time and a 30 μs time constant. Images were captured in a 16-bit grey scale using Olympus Fluoview 3000 software.

For imaging, a 25× water immersion objective lens (XLPLN25XWMP, 1.05 NA, Olympus) focused the beams onto the sample. Transmitted light was collected using an oil immersion condenser lens (1.4 NA, Olympus). A bandpass filter (893/209 BrightLine, 25 mm, Semrock) was employed to block the Stokes beam, allowing only the pump beam to reach a 10 mm × 10 mm Si photodiode (S3590-09, Hamamatsu). To enhance the photodiode's saturation threshold and reduce its response time, it was reverse-biased at 64 V. The output current was filtered

through a 19.2–23.6 MHz bandpass filter (BBP-21.4+, Mini-Circuits) and terminated with a 50 Ω load.

Statistical analysis

For label-free SRS imaging, the quantification of signals was performed by subtracting the background intensity obtained from a solution-only area. Nucleus were segmented using the Otsu's method[65]. The signal was normalized to the laser power. Each segmented nucleus was treated as an independent data point, and differences in background-corrected intensities among Fixed and SHRINK images were evaluated using Student's t-tests. Volume fold change quantification was calculated from the volume change of the same set of nuclei before and after SHRINK.

For immunolabeled samples, each image was divided into four equal-sized regions for independent analysis. Within each region, signal and background areas were identified using the Otsu's method[65], where the highest-intensity class was designated as the signal and the lowest-intensity class as the background. To account for variations in background intensity, the mean background value was subtracted from the corresponding signal value in each region. Subsequently, the background-corrected intensities were normalized to the laser power. Differences in these intensities among Fixed and SHRINK images were assessed using Student's t-tests.

4. 6 Supplementary information

Method	Volume Reduction Fold (Rodent Brain)	Hydrogel-Based	Solvent
SHRINK	~6.4	O	tert-butanol, diphenyl ether, benzyl alcohol, benzyl benzoate
uDISCO	1.8–2.8	X	tert-butanol, diphenyl ether, benzyl alcohol, benzyl benzoate
3DISCO	1.3–2.0	X	Tetrahydrofuran, dibenzyl ether
FDISCO	1.3–1.4	X	Tetrahydrofuran, dibenzyl ether, benzyl alcohol, benzyl benzoate
FluoClearBABB	1.3–1.4	X	tert-butanol, hexane, benzyl alcohol, benzyl benzoate
PEGASOS	1.4–1.7	X	tert-butanol, benzyl benzoate, polyethylene glycol-associated solvent

Table S1. Comparisons of tissue clearing methods that induce shrinkage.

Acronym	Chemical name	Chemical structure
DHEBA	N,N′-(1,2-dihydroxyethylene)bisacrylamide	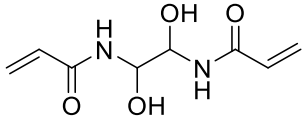

BIS	N,N -methylenebis(acrylamide)	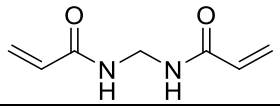
PDA	piperazine di-acrylamide	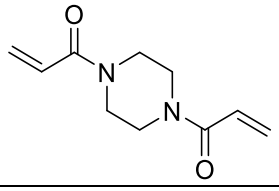
BAC	N,N′-bis(acryloyl)cystamine	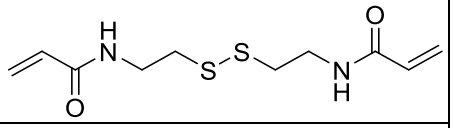
DATD	N,N'-diallyl-L-tartardiamide	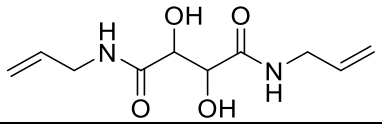

Table S2. Screened crosslinkers for tissue-gel hybridization.

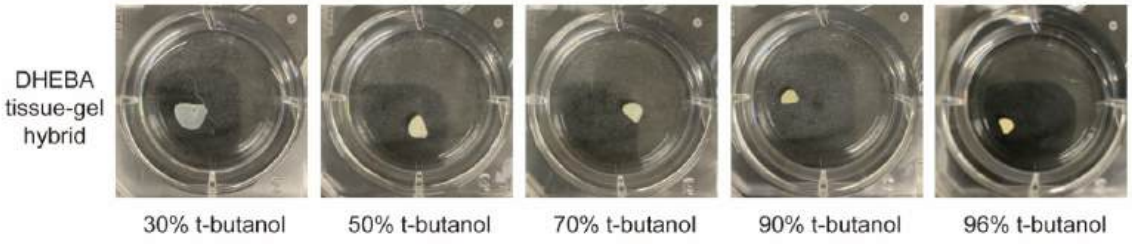

Figure S1 Homogenous and gradual tissue shrinkage was observed with gradient dehydration.

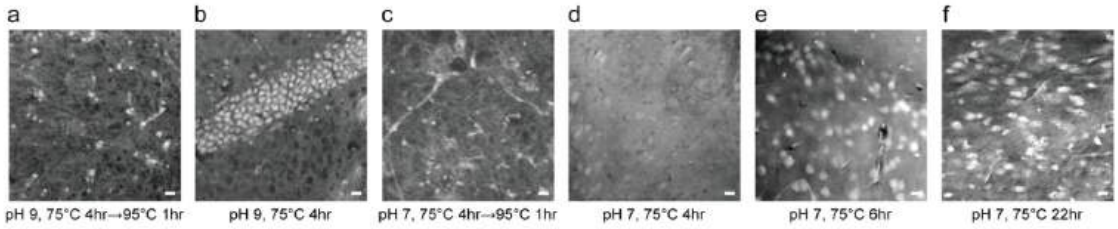

Figure S2 Evaluation of optimal denaturation conditions for DHEBA-crosslinked tissue-gel hybrids by label-free SRS imaging at CH_3 (2940 cm^{-1}) channel of the tissue-gel hybrid post-denaturation. (a-c) Post-denaturation imaging reveals tissue damage characterized by abnormal web-like structures and small holes. Significant damage is observed in samples denatured at pH 9 (a-b) or 95°C (a, c). (d-e) Normal morphology of tissues. (f) Mild damage, appearing as web-like structures and small holes within cell bodies, is evident after 22 hours of denaturation at pH 7. Scale bars: 10 μm.

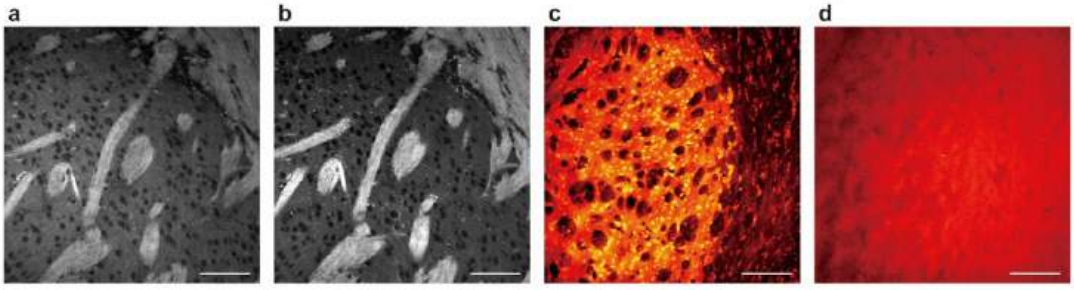

Figure S3 (a-b) Label-free SRS imaging at (a) CH_3 (2940 cm^{-1}) and (b) CH_2 (2845 cm^{-1}) channels of a fixed brain tissue sample at the striatum. (c-d) Label-free SRS-SHRINK imaging of a brain tissue sample at the striatum at (c) 2940 cm^{-1} and (d) 2845 cm^{-1}. Scale bars: 100 μm.

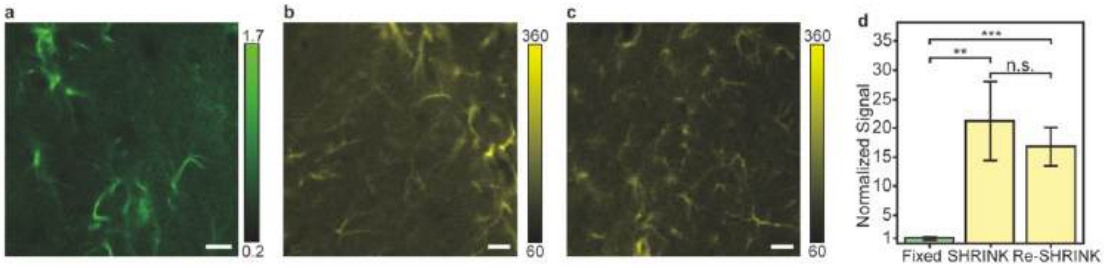

Figure S4 Fluorescence imaging of a ATTO680-GFAP-stained brain tissue sample. (a) Fixed tissue, (b) SHRINK tissue, and (c) SHRINK tissue stored at room temperature for two weeks, then rehydrated and shrunk again. (d) 21.20 ± 6.77 fold signal enhancement after SHRINK and 16.81 ± 3.28 fold after SHRINK, rehydration, and re-SHRINK after two-weeks storage are obtained. Scale bars: 10 μm. n = 4 for Fixed, n = 4 for SHRINK, n = 4 for Re-SHRINK. n.s: $P = 0.35$, not significant. **: $P = 0.0021$. ***: $P = 0.00017$.

	BABB-D15	ethyl cinnamate	benzyl alcohol	methyl slicylate	dimethyl sulfoxide
Attenuation coefficient (μm^{-1})	1.22E-03 ± 2.32E-04	3.06E-03 ± 7.23E-05	4.72E-03 ± 6.48E-04	4.55E-03 ± 1.27E-04	visually opaque

Table S3. Attenuation coefficients measured by label-free depth-resolved SRS imaging at CH_3 channel (2940 cm^{-1}) for tissue-DHEBA-gel hybrid in different RI matching solutions.

4. 7 References

1. Dent, J. A., Polson, A. G. & Klymkowsky, M. W. A whole-mount immunocytochemical analysis of the expression of the intermediate filament protein vimentin in Xenopus. *Development* **105**, 61–74 (1989).
2. Susaki, E. A. & Ueda, H. R. Whole-body and Whole-Organ Clearing and Imaging Techniques with Single-Cell Resolution: Toward Organism-Level Systems Biology in Mammals. *Cell Chem. Biol.* **23**, 137–157 (2016).
3. Ueda, H. R. *et al.* Whole-Brain Profiling of Cells and Circuits in Mammals by Tissue Clearing and Light-Sheet Microscopy. *Neuron* **106**, 369–387 (2020).
4. Qian, C. *et al.* Super-resolution label-free volumetric vibrational imaging. *Nat. Commun.* **12**, 3648 (2021).
5. Lin, L.-E., Miao, K., Qian, C. & Wei, L. High spatial-resolution imaging of label-free in vivo protein aggregates by VISTA. *Analyst* **146**, 4135–4145 (2021).
6. Wei, M. *et al.* Volumetric chemical imaging by clearing-enhanced stimulated Raman scattering microscopy. *Proc. Natl. Acad. Sci.* **116**, 6608–6617 (2019).
7. Shi, L. *et al.* Super-Resolution Vibrational Imaging Using Expansion Stimulated Raman Scattering Microscopy. *Adv. Sci.* **9**, 2200315 (2022).
8. Tuchin, V. Tissue Optics Light Scattering Methods and Instruments for Medial Diagnosis. *SPIE* **13**, (2000).
9. Yoon, S. *et al.* Deep optical imaging within complex scattering media. *Nat. Rev. Phys.* **2**, 141–158 (2020).
10. Hill, A. H., Manifold, B. & Fu, D. Tissue imaging depth limit of stimulated Raman scattering microscopy. *Biomed. Opt. Express* **11**, 762–774 (2020).

11. Wang, Q. *et al.* The Allen Mouse Brain Common Coordinate Framework: A 3D Reference Atlas. *Cell* **181**, 936-953.e20 (2020).
12. Lüders, E., Steinmetz, H. & Jäncke, L. Brain size and grey matter volume in the healthy human brain. *NeuroReport* **13**, 2371 (2002).
13. Hofman, M. A. Evolution of the human brain: when bigger is better. *Front. Neuroanat.* **8**, (2014).
14. Ahrens, M. B., Orger, M. B., Robson, D. N., Li, J. M. & Keller, P. J. Whole-brain functional imaging at cellular resolution using light-sheet microscopy. *Nat. Methods* **10**, 413–420 (2013).
15. Patel, K. B. *et al.* High-speed light-sheet microscopy for the in-situ acquisition of volumetric histological images of living tissue. *Nat. Biomed. Eng.* **6**, 569–583 (2022).
16. Chung, K. *et al.* Structural and molecular interrogation of intact biological systems. *Nature* **497**, 332–337 (2013).
17. Yang, B. *et al.* Single-Cell Phenotyping within Transparent Intact Tissue through Whole-Body Clearing. *Cell* **158**, 945–958 (2014).
18. Susaki, E. A. *et al.* Advanced CUBIC protocols for whole-brain and whole-body clearing and imaging. *Nat. Protoc.* **10**, 1709–1727 (2015).
19. Ke, M.-T., Fujimoto, S. & Imai, T. SeeDB: a simple and morphology-preserving optical clearing agent for neuronal circuit reconstruction. *Nat. Neurosci.* **16**, 1154–1161 (2013).
20. Kuwajima, T. *et al.* ClearT: a detergent- and solvent-free clearing method for neuronal and non-neuronal tissue. *Dev. Camb. Engl.* **140**, 1364–1368 (2013).

21. Hou, B. *et al.* Scalable and DiI-compatible optical clearance of the mammalian brain. *Front. Neuroanat.* **9**, 19 (2015).

22. Yu, T. *et al.* RTF: a rapid and versatile tissue optical clearing method. *Sci. Rep.* **8**, 1964 (2018).

23. Neckel, P. H., Mattheus, U., Hirt, B., Just, L. & Mack, A. F. Large-scale tissue clearing (PACT): Technical evaluation and new perspectives in immunofluorescence, histology and ultrastructure. *Sci. Rep.* **6**, 34331 (2016).

24. Sawada, K., Kawakami, R., Shigemoto, R. & Nemoto, T. Super-resolution structural analysis of dendritic spines using three-dimensional structured illumination microscopy in cleared mouse brain slices. *Eur. J. Neurosci.* **47**, (2018).

25. Ueda, H. R. *et al.* Tissue clearing and its applications in neuroscience. *Nat. Rev. Neurosci.* **21**, 61–79 (2020).

26. Richardson, D. S. & Lichtman, J. W. Clarifying Tissue Clearing. *Cell* **162**, 246–257 (2015).

27. Richardson, D. S. *et al.* Tissue clearing. *Nat. Rev. Methods Primer* **1**, 1–24 (2021).

28. Nudell, V. *et al.* HYBRiD: hydrogel-reinforced DISCO for clearing mammalian bodies. *Nat. Methods* **19**, 479–485 (2022).

29. Qi, Y. *et al.* FDISCO: Advanced solvent-based clearing method for imaging whole organs. *Sci. Adv.* **5**, eaau8355 (2019).

30. Renier, N. *et al.* iDISCO: A Simple, Rapid Method to Immunolabel Large Tissue Samples for Volume Imaging. *Cell* **159**, 896–910 (2014).

31. Ertürk, A. *et al.* Three-dimensional imaging of solvent-cleared organs using 3DISCO. *Nat. Protoc.* **7**, 1983–1995 (2012).

32. Pan, C. *et al.* Shrinkage-mediated imaging of entire organs and organisms using uDISCO. *Nat. Methods* **13**, 859–867 (2016).

33. Jing, D. *et al.* Tissue clearing of both hard and soft tissue organs with the PEGASOS method. *Cell Res.* **28**, 803–818 (2018).

34. Klingberg, A. *et al.* Fully Automated Evaluation of Total Glomerular Number and Capillary Tuft Size in Nephritic Kidneys Using Lightsheet Microscopy. *J. Am. Soc. Nephrol.* **28**, 452 (2017).

35. Park, Y.-G. *et al.* Protection of tissue physicochemical properties using polyfunctional crosslinkers. *Nat. Biotechnol.* **37**, 73–83 (2019).

36. Chen, F., Tillberg, P. W. & Boyden, E. S. Expansion microscopy. *Science* **347**, 543–548 (2015).

37. Ku, T. *et al.* Multiplexed and scalable super-resolution imaging of three-dimensional protein localization in size-adjustable tissues. *Nat. Biotechnol.* **34**, 973–981 (2016).

38. Chozinski, T. J. *et al.* Expansion microscopy with conventional antibodies and fluorescent proteins. *Nat. Methods* **13**, 485–488 (2016).

39. Murali Mohan, Y., Keshava Murthy, P. S. & Mohana Raju, K. Synthesis, characterization and effect of reaction parameters on swelling properties of acrylamide–sodium methacrylate superabsorbent copolymers. *React. Funct. Polym.* **63**, 11–26 (2005).

40. Üzüm, Ö. B., Kundakci, S., Durukan, H. B. & Karadağ, E. Swelling and dye sorption studies of AAm/SA hydrogels crosslinked by glutaraldehyde and divinylbenzene. *J. Appl. Polym. Sci.* **105**, 2646–2654 (2007).

41. Hennink, W. E. & van Nostrum, C. F. Novel crosslinking methods to design hydrogels. *Adv. Drug Deliv. Rev.* **64**, 223–236 (2012).

42. Gelfi, C. & Righetti, P. G. Polymerization kinetics of polyacrylamide gels I. Effect of different cross-linkers. *ELECTROPHORESIS* **2**, 213–219 (1981).

43. Zhao, H., Brown, P. H. & Schuck, P. On the Distribution of Protein Refractive Index Increments. *Biophys. J.* **100**, 2309–2317 (2011).

44. Krivosudský, O., Dráber, P. & Cifra, M. Resolving controversy of unusually high refractive index of a tubulin. *Europhys. Lett.* **117**, 38003 (2017).

45. Klein, J. & Heitzmann, R. Preparation and characterization of poly(acrylamide-co-acrylic acid). *Makromol. Chem.* **179**, 1895–1904 (1978).

46. Stejskal, J. & Horská, J. Refractive index increments of polyacrylamide and comments on the light scattering from its solutions. *Makromol. Chem.* **183**, (1982).

47. Plieva, F., Huiting, X., Galaev, I. Y., Bergenståhl, B. & Mattiasson, B. Macroporous elastic polyacrylamide gels prepared at subzero temperatures: control of porous structure. *J. Mater. Chem.* **16**, 4065–4073 (2006).

48. Miao, Y., Qian, N., Shi, L., Hu, F. & Min, W. 9-Cyanopyronin probe palette for super-multiplexed vibrational imaging. *Nat. Commun.* **12**, 4518 (2021).

49. Wei, L. *et al.* Super-multiplex vibrational imaging. *Nature* **544**, 465–470 (2017).

50. Shi, L. *et al.* Highly-multiplexed volumetric mapping with Raman dye imaging and tissue clearing. *Nat. Biotechnol.* **40**, 364–373 (2022).

51. Morell, P. & Quarles, R. H. Characteristic Composition of Myelin. in *Basic Neurochemistry: Molecular, Cellular and Medical Aspects. 6th edition* (Lippincott-Raven, 1999).

52. Tillberg, P. W. *et al.* Protein-retention expansion microscopy of cells and tissues labeled using standard fluorescent proteins and antibodies. *Nat. Biotechnol.* **34**, 987–992 (2016).

53. Chang, J.-B. *et al.* Iterative expansion microscopy. *Nat. Methods* **14**, 593–599 (2017).

54. Götz, R. *et al.* Nanoscale imaging of bacterial infections by sphingolipid expansion microscopy. *Nat. Commun.* **11**, 6173 (2020).

55. White, B. M., Kumar, P., Conwell, A. N., Wu, K. & Baskin, J. M. Lipid Expansion Microscopy. *J. Am. Chem. Soc.* **144**, 18212–18217 (2022).

56. Wen, G. *et al.* Evaluation of Direct Grafting Strategies via Trivalent Anchoring for Enabling Lipid Membrane and Cytoskeleton Staining in Expansion Microscopy. *ACS Nano* **14**, 7860–7867 (2020).

57. Chen, F. *et al.* Nanoscale imaging of RNA with expansion microscopy. *Nat. Methods* **13**, 679–684 (2016).

58. Wang, Y. *et al.* EASI-FISH for thick tissue defines lateral hypothalamus spatio-molecular organization. *Cell* **184**, 6361-6377.e24 (2021).

59. Wen, G. *et al.* A Universal Labeling Strategy for Nucleic Acids in Expansion Microscopy. *J. Am. Chem. Soc.* **143**, 13782–13789 (2021).

60. Alon, S. *et al.* Expansion sequencing: Spatially precise *in situ* transcriptomics in intact biological systems. *Science* (2021) doi:10.1126/science.aax2656.

61. Klimas, A. *et al.* Magnify is a universal molecular anchoring strategy for expansion microscopy. *Nat. Biotechnol.* **41**, 858–869 (2023).

62. Sun, D. *et al.* Click-ExM enables expansion microscopy for all biomolecules. *Nat. Methods* **18**, 107–113 (2021).

63. Ji, M. *et al.* Label-free imaging of amyloid plaques in Alzheimer's disease with stimulated Raman scattering microscopy. *Sci. Adv.* **4**, eaat7715 (2018).

64. Lin, H. *et al.* Microsecond fingerprint stimulated Raman spectroscopic imaging by ultrafast tuning and spatial-spectral learning. *Nat. Commun.* **12**, 3052 (2021).

65. Otsu, N. A Threshold Selection Method from Gray-Level Histograms. *IEEE Trans. Syst. Man Cybern.* **9**, 62–66 (1979).

[This chapter is temporarily embargoed.]